Wet and dry model granulates under mechanical load
-
A confocal microscopy study

Dissertation

zur Erlangung des Grades
„Doktor der Naturwissenschaften“
am Fachbereich Physik, Mathematik und Informatik
der Johannes-Gutenberg-Universität in Mainz

vorgelegt von

Jennifer Wenzl
geboren in Wiesbaden

Mainz, den 31.12. 2013

Die vorliegende Arbeit wurde in der Zeit von Juni 2010 bis Dezember 2013 unter der Betreuung von und am Max-Planck-Institut für Polymerforschung in Mainz durchgeführt.

Tag der mündlichen Prüfung:
Dekan:

1. Berichterstatter:
2. Berichterstatter:
3. Berichterstatter:
4. Berichterstatter:

D77

“How many bodies are required before we have a problem?”

R.D. Mattuck

Zusammenfassung

Granulare Materie, auch Schüttgut genannt, besteht aus diskreten Teilchen mit Größen zwischen Mikrometern bis hin zu Metern. Sie ist in vielen Industriezweigen und im täglichen Leben zu finden, wie z.B. in der Lebensmittelverarbeitung, Pharmazie und Kosmetik oder in der Öl- und Bergbauindustrie. Bei der Verarbeitung granularer Materie in Industrie oder mechanischer Verfahrenstechnik werden die Schüttgüter gespeichert, gemischt, gefördert oder filtriert. Diese Techniken beruhen auf der Grundlage makroskopischer Experimente, d.h. rheologischen Untersuchungen des Schüttguts als Ganzem mit seinen Volumeneigenschaften. Trotz der zahlreichen Untersuchungen dieser Volumeneigenschaften, ist die Beziehung zwischen den Einzelpartikelbewegungen und dem makroskopischen Verhalten des Schüttguts immer noch nicht ausreichend verstanden und experimentell herausfordernd. Für die Erforschung der mikroskopischen Eigenschaften auf Partikelniveau werden 3D-Bildgebungsverfahren benötigt.

Das Ziel der vorliegenden Arbeit war die Untersuchung von Einzelpartikelbewegungen in einem granularen System in 3D unter äußerer mechanischer Belastung, im Speziellen Kompression und Scherung. Während der mechanischen Belastung mittels Nanoindentation wurden die strukturellen und dynamischen Eigenschaften der granularen Systeme mit konfokaler Mikroskopie untersucht. Um den Anforderungen der konfokalen Mikroskopie zu entsprechen, wurden neue Modellsysteme für granulare Materie entwickelt und präpariert. Diese erforderten die Entwicklung neuer Analysealgorithmen sowie die Anpassung der bereits vorhandenen Analyseprogramme. Da die untersuchten Partikel Festkörper sind, wird ihre Bewegung durch sechs Freiheitsgrade beschrieben. Um die Bewegung vollständig mit allen sechs Freiheitsgraden zu erforschen, wurde im Rahmen dieser Arbeit eine Technik entwickelt, die die Visualisierung der Rotation sphärischer mikrometergroßer Partikel in 3D ermöglicht.

Einer der Schwerpunkte dieser Dissertation war ein Modellsystem für trockene kohäsive granulare Materie. In solchen Systemen wurde die Translation und Rotation der Einzelpartikel bei einer Kompression des granularen Systems untersucht. Im Allgemeinen war die Rotation der einzelnen Teilchen die empfindlichere Messgröße gegenüber der Translation. In Regionen mit großen strukturellen Veränderungen setzte die Rotation deutlich früher ein als die translatorische Bewegung.

In granularen Schichtsystemen unter Scherung wurden Scherdilatation und Scherzonenbildung beobachtet. Auf globaler Ebene zeigten die granularen Schichten ein Scherverhalten, welches bereits aus klassischen Scherexperimenten wie z.B. mit der Jenike-Zelle bekannt ist. Lokal wurde hingegen ein deutlich abweichendes Scherverhalten beobachtet. Die Scherzonenbildung wurde gefördert, wenn in der Nähe der aufgebrachten mechanischen Belastung bereits lokal eine Region mit niedrigerer Partikeldichte existierte. Allerdings trat auch in Regionen mit konstantem Volumenbruch eine Reorganisation

der Partikel auf. Es fand hier ein Mischen zwischen den verschiedenen Partikelschichten statt, insbesondere wurde ein Austausch von Partikeln zwischen dem fließenden Bereich und dem nicht fließenden beobachtet. Für das Verständnis der Fließeigenschaften von kohäsiven granularen Systemen, ist es somit nicht ausreichend sie lediglich mit Volumeneigenschaften, wie z.B. dem Volumenbruch zu beschreiben. Es müssen zusätzlich Einzelpartikeldynamiken, wie Translation und Rotation berücksichtigt werden.

Der zweite Schwerpunkt lag auf der Entwicklung und Untersuchung von einem Modellsystem für nasse granulare Materie, in denen eine zusätzliche bindende Flüssigkeit der Partikelsuspension hinzugegeben wird. Um auf Mikrometerskala die 3D-Struktur der bindenden Flüssigkeit unabhängig von den Partikeln zu untersuchen, wurde der bestehende konfokale Mikroskopaufbau weiter entwickelt. Dazu wurde ein zweiter Beleuchtungs- und Detektionsstrahlengang für die gleichzeitige Beobachtung beider Phasen im Mikroskop implementiert. In den durchgeführten Scher- und Kompressionsexperimenten von nassen Clustern und Volumensystemen traten völlig andere Dynamiken im Vergleich zu trockenen kohäsiven Modellsystemen auf. Die zusätzliche bindende Flüssigkeit veränderte das Fließverhalten der Partikelsuspension drastisch. In einem System ähnlich einer Pickering-Emulsion traten große strukturelle Veränderungen in der lokalen Umgebung um Flüssigkeitstropfen auf. Die Ursache dieser Veränderungen war ein Wechselspiel zwischen der gespeicherten Energie in den Flüssigkeitstropfen nach dessen Deformation und der Bindungsenergie der Partikel in der Tropfenoberfläche.

Konfokale Mikroskopie in Kombination mit Nanoindentation gaben neue Einblicke in die Einzelpartikelbewegungen und -dynamiken von granularen Systemen unter mechanischer Belastung. Diese neuen experimentellen Ergebnisse können dazu beitragen, das Verständnis der Beziehung zwischen den Volumeneigenschaften von granularer Materie, wie Volumenbruch oder Fließspannung, und der Dynamik auf Einzelteilchenniveau zu verbessern.

Abstract

Granular matter, also known as bulk solids, consist of discrete particles with sizes between micrometers and meters. They are present in many industrial applications as well as daily life, like in food processing, pharmaceutics and cosmetics or in the oil and mining industry. When handling granular matter in industries or process engineering, the bulk solids are stored, mixed, conveyed or filtered. These techniques are based on observations in macroscopic experiments, i.e. rheological examinations of the bulk properties. Despite the amply investigations of bulk mechanics, the relation between single particle motion and macroscopic behavior is still not well understood and experimentally challenging. For exploring the microscopic properties on a single particle level, 3D imaging techniques are required.

The objective of this work was the investigation of single particle motions in a bulk system in 3D under an external mechanical load, i.e. compression and shear. During the mechanical load applied with nanoindentation the structural and dynamical properties of these systems were examined with confocal microscopy. To satisfy the requirements for confocal microscopy, new granular model systems in the wet and dry state were designed and prepared. These new model systems required the development of new analysis algorithms and the customization of the existing analysis programs. As the particles are solid bodies, their motion is described by six degrees of freedom. To explore their entire motion with all degrees of freedom, a technique to visualize the rotation of spherical micrometer sized particles in 3D was developed.

One of the foci during this dissertation was a model system for dry cohesive granular matter. In such systems the translation and rotation during a compression of the granular matter was investigated. In general the rotation of single particles was the more sensitive parameter compared to the translation. In regions with large structural changes the rotation had an earlier onset than the translation.

In granular systems under shear, shear dilatation and shear zone formation were observed. Globally the granular sediments showed a shear behavior, which was known already from classical shear experiments, for example with Jenike cells. Locally a different shear behavior was observed. The shear zone formation was enhanced, when near the applied load a locally pre-diluted region existed. But even in regions with constant volume fraction a reorganization of particles occurred. A mixing between the different particle layers occurred, in particular an exchange of particles between the current flowing region and the non-flowing region was observed. Hence for understanding the flow properties of granular cohesive systems, they have to be described not only by bulk parameters, e.g. the volume fraction but also with single particle dynamics, such as translation and rotation.

The second focus was on model systems for wet granular matter, where an additional binding liquid is added to the particle suspension. To examine the 3D structure of the binding liquid on the micrometer scale independently from the particles, the existing confocal microscope setup was further developed. A second illumination and detection beam path for the simultaneous observation of both phases was implemented. In shear and compression experiments of wet clusters and bulk systems completely different dynamics compared to dry cohesive models systems occured. The additional binder liquid drastically changed the flow behavior of the particle suspension. In a Pickering emulsion-like system large structural changes predominantly occurred in the local environment of binding liquid droplets. These large local structural changes were due to an energy interplay between the energy stored in the binding droplet during its deformation and the binding energy of particles at the droplet interface.

Confocal microscopy in combination with nanoindentation gave new insights into the single particle motions and dynamics of granular systems under a mechanical load. These novel experimental results can help to improve the understanding of the relationship between bulk properties of granular matter, such as volume fraction or yield stress and the dynamics on a single particle level.

Contents

1 Introduction and Motivation

The science dealing with granular granular matter has grown in the recent years, as it is present in many industrial applications and daily life, e.g. in food processing, pharmaceutics and cosmetics or in the oil and mining industry [1]. Granular matter consists of discrete particles, spanning a large range of sizes from micrometers up to several meters. Granular matter is divided in dry and wet granular system. In dry granulate systems, the particles are suspended in air. They are usually present as flour and sugar in food industries or in pharmaceutics, when thinking of fine powders as carrier material for drug delivery in powder inhalers. In wet granular systems an additional binder liquid builds an connecting network between the particles. These systems occur for example in the mining industry, when dealing with oil sand, or in cosmetics, where fine powder particles are embedded in an oil-water emulsion.

When handling granular matter in industries or process engineering, the bulk solids have to be stored, mixed, conveyed or filtered. All these different manufacturing processes depend on the bulk flow properties, i.e. the rheology of these systems. Classical rheometry [2] provides various possibilities probing the rheology of granulate systems. Rheological testings under shear are achieved by a wide range of shear devices [3]. The techniques and mechanics, which are then applied in industries are based on these macroscopic experiments.

Although the bulk mechanics are amply characterized by rheological methods, undesired effects appear during the manufacturing processes, which could be no longer explained only by bulk properties. For example when storing dry granulates in silos, a breaking of the confining walls was observed. The reason is an inhomogeneous stress distribution inside the bulk due to particle networks and force chains. Such particle networks can build bridges, which then hinder also the flow out of silos or during pumping. These effects show that a macroscopic description of granular matter is not sufficient for a full understanding of the granulates behavior.

Thus, a microscopic investigation on a single particle level is needed. A focus should lie on the influence of the macroscopically applied load on the single particle motions and the dependence on the particle interactions at the contacts. The problem here is that due to the large size of the particles ($> 1\mu\mathrm{m}$) the granular systems are athermal and depend on the history of treatment. Furthermore, the particle shape anisotropy and the number of degrees of freedom (translation and rotation) complicate a theoretical description. These as well as the high number of particles (typically $> 10^4$) increase the computational costs of simulations and make them time-consuming. The goal is to find simplified model systems, which show the effects of interest of real granulate systems.

Knowing the particle interactions at the contacts is a first step for the understanding of granular matter mechanics. On the modeling side, various contact models describe the

interaction between two contacting particles [4–6]. Experimentally numerous techniques are available to measure the particle-particle interactions. Methods as atomic force microscopy [7] or the surface force apparatus [8] are widely used. The first choice for a bulk system is a simplification of the problem on 2D. With contact dynamic simulations Kadau et al. explored the compaction of cohesive granular particles in 2D [9]. Experimentally the problem is typically broken down to two-dimensional disks. Aguirre et al. investigated the flow of disks through an aperture, which could be used as a model system for the discharging of silos [10]. With video imaging they captured the flow for different aperture diameters and flow velocities. A technique for visualizing stress distributions and force chains in granulates under load is using photoelastic disks [11]. Zhang et al. examined granulates near jamming and compared their experimental results with theoretical models. Further investigations of granular matter in the solid-, liquid- or gas-like state can be found in the overview of Jaeger et al. [12]. Results on granular flows for different geometries both in experiments and numerical work is reviewed in [13].
Experimentally it is challenging to investigate bulk solids in 3D. Using X-ray tomography, a 3D exploration of dense granular systems is possible [14,15]. Obtaining such 3D images usually takes up to hours per scan with voxel sizes up to tens of micrometers. Laser scanning techniques are complementary methods allowing destruction free 3D imaging of granular systems at a shorter time scale and better spatial resolutions than X-ray tomography. New X-ray micro-tomography methods using synchrotron radiation can achieve resolutions typically down to a few µm per voxel [16]. In contrast laser scanning confocal microscopes work with an optical resolution of roughly 0.5 µm per voxel. A combination of confocal microscopy with microsphere indentation was used to study the mechanical behavior of densely packed spheres [17]. The particle sediments behaved like yield-stress materials, which were solid-like below a critical stress and liquid-like above it.
An additional binding liquid in wet granular system complicates the investigation, as here particles and the liquid distribution have to be described and visualized. Granular systems get stiffer due to the additional binding liquid. Whether the network of capillary bridges or the increase of the friction force between the particles causes the stiffness is still under investigation. Overviews over the current theoretical and experimental state of the art can be found in [18, 19]. Sediments of emulsion droplets under microsphere indentation were investigated in 3D with confocal microscopy [20]. Force-depth curves revealed that the mechanical resistance of the networks originated from interdroplet friction forces.

The aim of this work was to investigate model granulate bulk systems in the wet and dry state under a mechanical load. A combination of confocal microscopy for 3D imaging with nanoindentation was used. The load, i.e. compression and shear was applied globally on scales larger than the particle diameter. The focus was on the relationship between the global macroscopic behavior and the single particle dynamics. Questions as how structural changes in dry cohesive granulates influence the single particle motion, i.e. the translation and especially the rotation were investigated. In shear experiments a focus was on the shear zone formation and dilatation. Single particle motions in the flowing and non-flowing region were compared with expectations from classical shear experiments, such as from Jenike cells. With 2-color confocal microscopy a model system for wet granulates with an inhomogeneously distributed binding liquid was explored. 3D investigations revealed that the binding liquid dominated the granulate dynamics on a local scale.

2 Theory

2.1 Introduction into Granular Matter

Granular matter are bulk solids consisting of discrete solid particles, the so-called “grains” or “granulates”. The particle size ranges from 1 µm and can go up to several meters. In general granular matter consists of non-spherical and polydisperse particles. Due to the large grain size, granular systems are athermal and dominated by gravitation, while Brownian motion can usually be neglected. A special category of granulates are the so-called “fine powders” with grain sizes between 1 µm and 10 µm [21]. For fine powders common interactions such as Van der Waals or electrostatic interactions can be in the same order of magnitude or can even exceed the gravitation.

In general one has to distinguish between dry and wet granulate systems. In dry granulate systems the particles are suspended in a continuous medium, which is usually air. The single particle interactions are mainly acting over the surface of the particle contact. In wet granulate systems an additional liquid, the so-called “binding liquid”, is added to the dry granulate suspension. This binding liquid adds an additional capillary interaction to the system.

When dealing with granular matter in industries or process engineering a macroscopic description of bulk solids as a continuum is used [22]. The considered volume elements in a continuum description are chosen large enough compared to the grain size, so that single particle interactions could be neglected. The properties of the bulk are then described with macroscopic parameters, such as the hardness (see Sec.2.3.1) or the volume fraction, i.e. the solid fraction in the bulk volume (see Sec.5.2.2). When bulk solid are exposed to a mechanical load, the single particle contacts have an influence on the deformation and flow of the bulk, e.g. when building up force chains (see Sec.2.4.2 and Sec.2.4.3). In this case the bulk solids have to described microscopically, i.e. on a single particle level.

2.2 Particle Interactions and Forces

For understanding the dynamics in bulk granulates, the interactions between the single particles inside the bulk have to be known. The interactions, i.e. the forces are dominant at the particle surfaces or the interface between them. The most fundamental force is the Van der Waals force, which acts between uncharged molecules of the surface over short distances of a few nanometers. When the surfaces are charged, electrostatic interactions have to be considered, which are more long ranged. In real systems due to the humidity of the surrounding air, liquid films occur on the particle surfaces. When two particles are in close contact, a liquid meniscus is created, which adds an additional force onto the particles. When dealing with suspensions and slurries, usually only the particle motions are considered. For particles moving in these liquids, the flow and motion of the liquid gets significant. The liquid then applies so-called hydrodynamic forces onto the particles, which can drastically change the dynamics of the system.

2.2.1 Van der Waals Forces

Van der Waals forces are very important, as they act between every molecules or surfaces. These forces arise between neutral molecules and are due to interactions between their dipole moments. This dipolar interaction is usually attractive and acts over short distances of a few tens of nanometers.
The Van der Waals potential between two molecules is very steep with a x^{-6}-decrease and is composed of three components: the Keesom, the Debye and the London interaction.

$$V_{VdW}(x) = -\left(C_{Keesom} + C_{Debye} + C_{London}\right) \cdot \frac{1}{x^6} = -C_{total} \cdot \frac{1}{x^6} \tag{2.1}$$

with C_j the interaction constant for the corresponding interaction term and C_{total} their sum.

Keesom interaction The Keesom or orientation term describes the interaction between two fixed but freely rotating permanent dipoles [23]. The dipoles have a preferential orientation of maximum interaction, when their opposite charges are facing each other. Thermal fluctuations drive the dipoles away from their preferential orientation. The net orientation is a balance between these effects and results in an attractive potential (Fig.2.1).

$$V_{Keesom}(x) = -\frac{p_1^2 p_2^2}{3(4\pi\varepsilon_0)^2 k_B T} \cdot \frac{1}{x^6} \tag{2.2}$$

with p_i the dipole moment of molecule i, ε_0 the electric constant, k_B the Boltzmann constant and T the temperature.

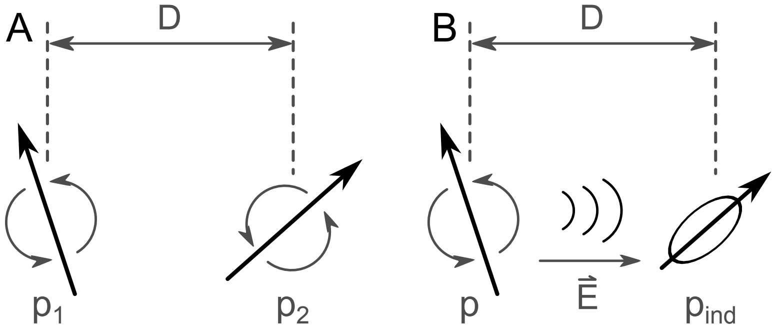

Figure 2.1: Geometry for the Keesom interaction between two freely rotating permanent dipoles (A) and geometry for the Debye interaction between a permanent and an induced dipole (B) with separation distance D

Debye interaction The Debye or induced dipole term describes the interaction between a fixed permanent and an induced dipole moment, which are both able to rotate freely [24]. A permanent static dipole moment generates an electric field $\vec{E}$ in its surrounding. When this static dipole approaches a nonpolar molecule, a charge shift and hence a dipole moment is induced (Fig.2.1). The new induced dipole moment p_{ind} interacts with the permanent dipole moment.

$$V_{Debye}(x) = -\frac{p^2\alpha}{(4\pi\varepsilon_0)^2} \cdot \frac{1}{x^6} \tag{2.3}$$

with p the permanent dipole moment and α the polarizability of the nonpolar molecule.

London interaction The London or dispersion term describes the interaction between two nonpolar molecules and is due to quantum mechanical effects [25]. In the molecules quantum mechanically the electron density distribution oscillates and rearranges with frequencies ν_i, this leads to a polarization of the molecule. The polarized molecule induces then a dipole moment in adjacent molecules. During the approach of two oscillators, they interact with each other, leading to a net attractive potential.

$$V_{London}(x) = -\frac{3}{2}\frac{\alpha_1\alpha_2}{(4\pi\varepsilon_0)^2}\frac{2\pi\hbar\nu_1\nu_2}{(\nu_1+\nu_2)} \cdot \frac{1}{x^6} \tag{2.4}$$

with α_i and ν_i the polarizability and ionization frequency of molecule i.
Usually the London dispersion interaction is dominant even for polar molecules. It has only a x^{-6}-decrease, when the electrical field of the oscillator has enough time to propagate over the separation distance D before the polarization orientation changes. This is only the case, if $D < c/\nu_i$ is valid, with c the speed of light. For larger separation distances $D > 10$nm the London potential decreases more steeply and has a x^{-7}-decrease for molecules. This effect is called retardation.

So far Van der Waals interactions between single molecules were discussed. There are two possibilities to obtain the Van der Waals interactions for macroscopic extended objects.

Hamaker approach One possibility is the Hamaker concept [26], which is a microscopic approach. The potentials are then determined by a pairwise summation of the potentials between all molecules in the solid. High order interactions i.e. the influence of third molecules are neglected. This gives no precise quantitative prediction of the Van der Waals potential, but a good qualitative understanding. Nevertheless for many geometries this assumption gives values in good agreement with experiments for the Van der Waals potential. Summing up all potentials between the molecules one obtains for the Van der Waals potential between two infinitely extended planes of material A and B at a separation distance D:

$$V_{plane} = -\frac{\pi C_{AB}\varrho_A\varrho_B}{12D^2} \tag{2.5}$$

Here C_{AB} is the total interaction constant for materials A and B (see Eq.2.1) and ϱ_i the molecular density of object i. Compared to the case of two single molecules, the Van der Waals potential here is less steeply, which is characteristic for all geometries with extended objects. In the Hamaker concept the Van der Waals potentials between two objects can be divided in a geometrical part and the so-called Hamaker constant A_H, which contains only the molecule and material parameters.

$$A_H = \pi^2 C_{AB} \varrho_A \varrho_B \tag{2.6}$$

The Van der Waals energy between two spheres with radii R_1 and R_2 with a separation distance D can then be calculated with

$$E_{VdW} = -\frac{A_H}{6D} \frac{R_1 R_2}{R_1 + R_2} \tag{2.7}$$

Lifshitz theory A macroscopic calculation to obtain Van der Waals potentials is the Lifshitz theory [27]. Here two objects of material A and B are interacting over a medium I via the correlation of electromagnetic fluctuations and the exchange of virtual photons. The distance dependence obtained from the Hamaker approach is also valid for the Lifshitz theory. Only the Hamaker constant is calculated in a different way, using the bulk dielectric and magnetic properties of the involved materials. For non-magnetic materials the magnetic contribution is negligible compared to the dielectric contribution.

A main issue for calculating A_H is the knowledge of the dielectric properties for all materials over the entire wavelength or frequency range respectively. These properties are characterized by the dielectric response function $\varepsilon(\omega)$ with angular frequencies ω. New experimental methods to obtain $\varepsilon(\omega)$ is for example "vacuum ultraviolet spectroscopy" [28] or "valence electron energy loss spectroscopy" (VEELS) [29]. To calculate afterwards the Hamaker constant from the spectroscopic data one can use the "simple spectral method" [30], the "Tabor-Winterton approximation" [8, 31] or the "full spectral method" [32]. If there is sufficient spectral data available the "full spectral method" is used. Otherwise or for a quick estimation one uses the "Tabor-Winterton approximation", as it is a function of the materials refractive indices n_i, dielectric constants ε_i and ionization frequencies ν_i of the three materials. Usually these material parameters are available for a wide range of materials. For two materials A and B interacting over an intermediary material I, the Hamaker constant can be calculated with the Tabor-Winterton approximation:

$$\begin{aligned} A_{AIB} \approx\ & \frac{3}{4} k_B T \left(\frac{\varepsilon_A - \varepsilon_I}{\varepsilon_A + \varepsilon_I} \right) \left(\frac{\varepsilon_B - \varepsilon_I}{\varepsilon_B + \varepsilon_I} \right) \\ & + \frac{3\pi\hbar\nu_e}{4\sqrt{2}} \frac{\left(n_A^2 - n_I^2\right)\left(n_B^2 - n_I^2\right)}{\sqrt{n_A^2 + n_I^2} \cdot \sqrt{n_B^2 + n_I^2} \cdot \left(\sqrt{n_A^2 + n_I^2} + \sqrt{n_B^2 + n_I^2} \right)} \end{aligned} \tag{2.8}$$

Under the assumption that the ionization frequencies of the three involved materials are nearly the same, one can take a mean ionization energy ν_e instead.

There are several methods to obtain Van der Waals forces and Hamaker constants experimentally for macroscopic objects. Widely used are the "surface force apparatus" (SFA) [8] or the "atomic force microscope" (AFM) [7]. The SFA consists of two atomically smooth crossed mica cylinders, where one is mounted onto a translator and one onto a spring. The separation distance is measured with optical interference techniques, the forces are determined from the spring deflection. With a AFM the force is measured between the surface and a sharp tip, mounted on a cantilever. The force is then detected over the deflection of the cantilever. This is often used in combination with the colloidal probe technique [33], where a small colloid instead of a sharp tip is mounted onto the cantilever.

2.2.2 Electrostatic Forces

In industries granulates are often handled in form of slurries and suspensions. Depending on the used surrounding solvent, particles and surfaces are more or less charged. This causes a manifold interaction behavior between the surfaces.
In polar solvents with high dielectric constant ε (e.g. water) the surfaces get easily charged, due to the dissociation of surface molecules. A surface potential ψ_0 is then built up by the surface charges with charge density σ_e. In the solvent volume the electric potential $\psi(x, y, z)$ is described by the Poisson equation.

$$\vec{\nabla}^2 \psi = -\frac{\varrho_e}{\varepsilon\varepsilon_0} \tag{2.9}$$

with ϱ_e the local charge distribution. There are two contributions to the local charge distribution in the solvent. One is a background ion concentration c_b of dissociated external salts. The second contribution is a counterion concentration c_0 from the dissociation of the surface molecules. After dissociation thermal fluctuations drive the counterions away from the charged surface. Their spatial distribution can be described with Boltzmann statistics.

$$\varrho_{e,c_0} = c_0 e \cdot \left(\exp\left(-\frac{e\psi}{k_B T}\right) - \exp\left(\frac{e\psi}{k_B T}\right) \right) \tag{2.10}$$

It is assumed that the background ion concentration is significantly higher than the counterion concentration to avoid charge imbalance. Further only monovalent ions are considered here. Combining Eq.2.9 and Eq.2.10 one obtains the so-called Poisson-Boltzmann equation, which describes the electrical potential near a charged surface.

$$\vec{\nabla}^2 \psi = \frac{c_0 e}{\varepsilon\varepsilon_0} \left(\exp\left(\frac{e\psi}{k_B T}\right) - \exp\left(-\frac{e\psi}{k_B T}\right) \right) \tag{2.11}$$

It is a partially differential equation of degree two and can be solved analytically only for simple geometries.

Linear one-dimensional case For the geometry of two planar surfaces the Poisson-Boltzmann equation can be reduced to an one-dimensional case. The electric potential is then only changing along the axis normal to the planes:

$$\frac{\partial^2\psi}{\partial x^2} = \frac{c_0 e}{\varepsilon\varepsilon_0}\left(\exp\left(\frac{e\psi(x)}{k_B T}\right) - \exp\left(-\frac{e\psi(x)}{k_B T}\right)\right) \tag{2.12}$$

For small potentials $e\,|\psi| \ll k_B T$ the Poisson-Boltzmann equation can be linearized. This means that the exponential terms are expanded in series and terms of higher order than the linear one are neglected. This leads to an electrical potential of

$$\psi(x) = \psi_0 \exp\left(-\kappa x\right) \tag{2.13}$$

with κ the inverse Debye length

$$\kappa = \sqrt{\frac{2c_0 e^2}{\varepsilon\varepsilon_0 \mathrm{k_B T}}} \tag{2.14}$$

So far only monovalent ions have been considered. In many systems also ions with higher valency Z are present. Taking also the background ion solution into account, the inverse Debye length is

$$\kappa = \sqrt{\frac{e^2}{\varepsilon\varepsilon_0 \mathrm{k_B T}}\sum_i \left(c_{0,i}Z_i^2 + c_{b,i}Z_i^2\right)} \tag{2.15}$$

The linearization of the Poisson-Boltzmann equation is also called Debye-Hückel approximation [34], as Debye and Hückel firstly used the linearization to describe the electric potential around a sphere (Fig.2.2). Due to the spherical geometry the potential has a radial dependence, which is of a Yukawa-like shape. Additionally the finite size of the sphere with radius R_p has to be taken into account, this leads to an additional volume exclusion term in the potential:

Figure 2.2: Effective charge distribution of counterions around a sphere with surface charge Z_p. The counterions are mainly located in a shell with thickness κ^{-1} around the sphere

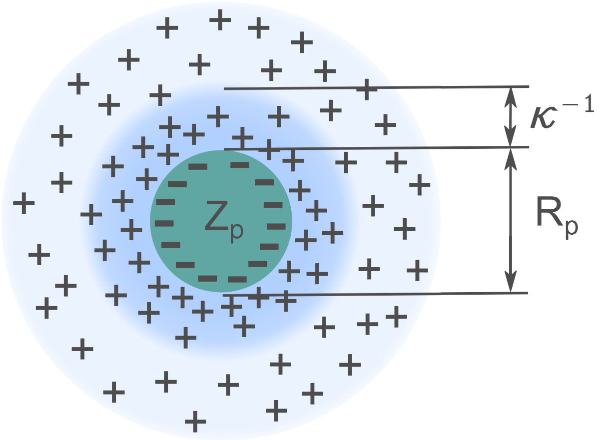

$$\psi(r) = \frac{Z_p e}{4\pi\varepsilon\varepsilon_0}\cdot\frac{\exp\left(\kappa R_p\right)}{1+\kappa R_p}\cdot\frac{\exp\left(\kappa r\right)}{r} \tag{2.16}$$

with $Z_p$the particle surface charge.

Non-linear case In many cases the linearization gives realistic results, but for higher potentials $|\psi|$ the Poisson-Boltzmann equation can no longer be linearized. The full solution leads then to lower potentials and steeper decays at low distances compared to the linearized solution. For calculating the potential over the entire distance range, the surface potential ψ_0 has to be known. As it is built up by the surface charges, ψ_0 is directly related to the surface charge density σ_e.

$$\sigma_e = \sqrt{8c_0\varepsilon\varepsilon_0 k_B T} \cdot \sinh\left(\frac{e\psi_0}{2k_BT}\right) \tag{2.17}$$

and for small potentials

$$\sigma_e = \kappa\varepsilon\varepsilon_0\psi_0 \tag{2.18}$$

The charge density σ_e and so the surface potential ψ_0 are strongly dependent on the background salt concentration, as it effects the dissociation of the surface molecules. Hence for high background salt concentration more dissociated surface charges are needed to build up the same surface potential than for a lower background salt concentration.

DLVO theory

The electrostatic repulsion and the screening of surface charges could not explain for a long time the coagulation of charged particles. The combination of attractive Van der Waals and repulsive electrostatic forces could overcome this problem and is described by the DLVO theory. This theory was developed around 1940 by Derjaguin and Landau [35] and independently by Verwey and Overbeek in 1948 [36]. At large distances there exists a secondary minimum, where the particles feel a slight attraction (Fig.2.3). The coagulation of particles is reversible in this region. The electrostatic repulsion gets significant at intermediate distances and prevent the particles from coagulation. At small distances the suspension gets unstable. In the primary energy minimum the attractive Van der Waals forces are dominant and the particles coagulate irreversibly. Depending on the background salt concentration these three regions are more or less pronounced.

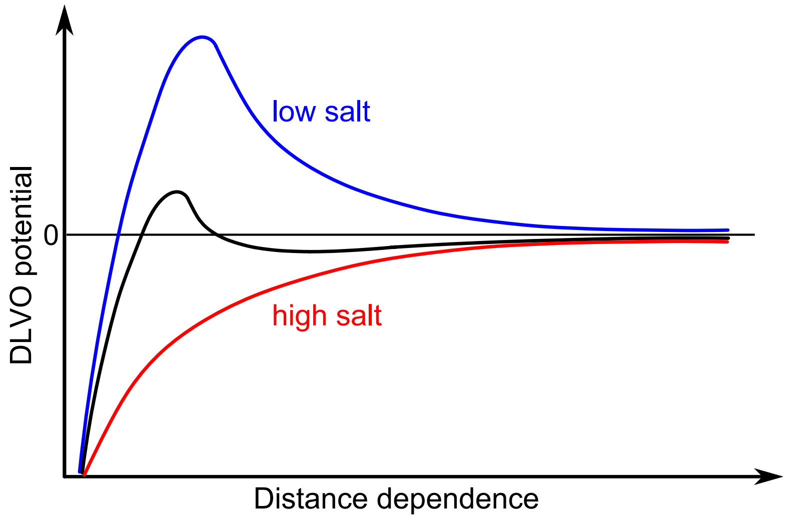

Figure 2.3: Interaction potential between two surfaces based on the DLVO theory. With decreasing background salt concentration the primary minimum gets more pronounced and deeper. For high salt concentrations the secondary energy minimum disappears

Electrostatics in nonpolar solvents

In nonpolar solvents, i.e. in solvents with low dielectric constants, surfaces are usually less charged than in polar solvents. The electrical work to separate two charges from a separation distance D to infinity is

$$E_{el} = \frac{e^2}{4\pi\varepsilon\varepsilon_0 D} \tag{2.19}$$

The required work for charge separation is reciprocally dependent on the dielectric constant ε. Hence it is significant higher in nonpolar media and molecules are less able to dissociate. As the surface charge density is dependent on the dielectric properties of the solvent, less surface charges are required to built up the same surface potential ψ_0 than for polar media. For low potentials the surface potential can be derived with

$$\psi_0 = \frac{\sigma_e}{\varepsilon\varepsilon_0\kappa} = \frac{\sigma_e}{e}\sqrt{\frac{k_B T}{2c_0\varepsilon\varepsilon_0}} \tag{2.20}$$

These effects have an influence on the electrostatic stabilization of dispersions. Usually for liquids with dielectric constants ε larger than 11, dispersions can be stabilized as sufficient as in aqueous media. In contrast, for $\varepsilon < 5$ the electrostatic stabilization of dispersions is hardly possible.

2.2.3 Capillary Forces

Wetting phenomena

Young equation Considering a liquid drop, sitting on a solid surface with a contact angle Θ (Fig.2.4). A three-phase contact line is then formed between the solid, the liquid and the gaseous environment. The wetting behavior of a liquid on solid surfaces is described by the Young equation [37], which relates the contact angle with the surface tensions of the involved materials:

Figure 2.4: Part of a liquid drop with a contact angle Θ sitting on a solid surface. A three-phase contact line is formed between the solid, the liquid and the gaseous environment

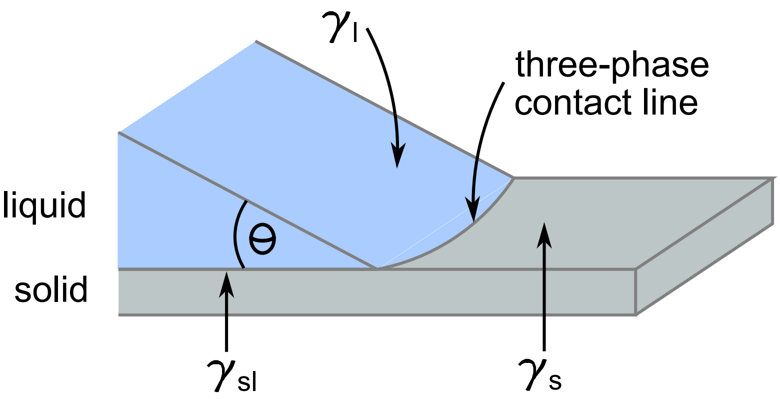

$$\gamma_l \cdot \cos\Theta = \gamma_s - \gamma_{sl} \tag{2.21}$$

γ_s and γ_l are the surface tensions of the solid and liquid surface, γ_{sl} of the solid-liquid interface. Liquids with contact angles below 90° are called wetting liquids, for higher contact angles they are called non-wetting liquids. For total wetting a thin liquid film is spreading over the surface with a zero contact angle. The Young equation is also valid, when the gaseous environment is exchanged by a second liquid. The interfacial tensions of the involved materials then have to be considered, i.e. the liquid-liquid interface tension γ_{ll} and the solid-liquid interface tensions γ_{sl_i} of the two liquids i.

Young-Laplace equation When two particles are in contact in a humid environment, condensed liquid creates a meniscus around the contact area. This liquid meniscus generates an attractive force called capillary or meniscus force. This force has two contributions. Due to the surface tension, liquid surfaces try to reduce the surface area. For a meniscus around two spheres this is the case, when the particles are as close as possible. Hence the surface tension of the bridging liquid drags the particles together. Additionally due to the curved surface there is a pressure difference, also called Laplace pressure, between the liquid and the surrounding fluid. This negative pressure act over the cross-sectional area of the meniscus, which also pulls the particles towards each other.

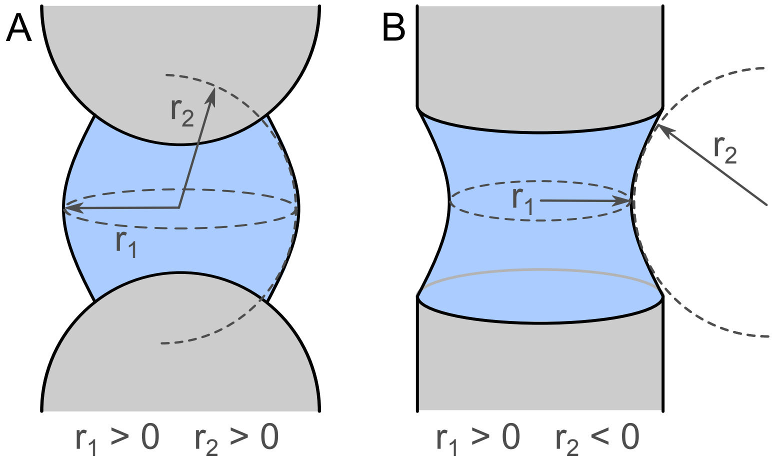

Figure 2.5: Capillary bridge between two spheres with positive radii of curvature (A). The radii r_1 and r_2 are the radii of curvature of the liquid bridge and are oriented in perpendicular planes. Pendular bridge between two cylinders (B)

The Young-Laplace equation describes this pressure difference between a fluid and a bridging liquid with a curved interface, when gravitation is negligible.

$$\Delta P = \gamma_l \cdot \left(\frac{1}{r_1} + \frac{1}{r_2} \right) \tag{2.22}$$

With γ_l the surface tension of the bridging liquid and r_1 and r_2 the radii of curvature. When the surrounding medium is a gas, the Laplace pressure is $\Delta P = P_{liquid} - P_{gas}$. The sum of the curvatures $1/r_1 + 1/r_2$ describes the local curvature of a surface at an arbitrary point on this surface. The radii of curvature are determined along perpendicular oriented planes (Fig.2.5). Radii of curvature lying on planes inside the liquid are defined positive. When the plane is oriented outside the liquid, the radius of curvature is negative. If the liquid structure exceeds a certain size or volume, gravitation, i.e. the hydrostatic pressure, has to be considered.

$$\Delta P = \gamma_l \cdot \left(\frac{1}{r_1} + \frac{1}{r_2}\right) + \varrho_l g h \tag{2.23}$$

with ϱ_l the liquid's mass density, g the acceleration of gravity and h the height coordinate. A rule of thumb is, when the curvature of the bridging liquid is much smaller as the capillary constant $\kappa_c = (\gamma_l/\varrho_l g)^{1/2}$, then the hydrostatic pressure can be neglected. For water in air the capillary constant is 2.7mm.

Kelvin equation For positively curved surfaces the Laplace pressure is increased. Liquid molecules then tend to evaporate faster, which leads to a higher vapor pressure P_v above the curved liquid. The vapor pressure is increased compared to the vapor pressure of a planar surface. This change in the vapor pressure for curved liquid surfaces is described by the Kelvin equation [38].

$$N_A k_B T \cdot \ln\left(\frac{P_v}{P_{v,0}}\right) = \gamma_l V_m \cdot \left(\frac{1}{r_1} + \frac{1}{r_2}\right) \tag{2.24}$$

with N_A the Avogadro constant, V_m the liquids molar volume and $P_{v,0}$ the vapor pressure of a planar surface. Many phenomena can be explained with the Kelvin equation, e.g. the condensation of liquid into pores, which occurs at pressures below $P_{v,0}$. The liquid keeps condensating into the pore until the meniscus has reached the curvature value determined with Eq.2.24. This is only the case if the liquid totally wets the surface, i.e. has a contact angle of zero (Fig.2.6A). If the liquid does not totally wet the pore surface, less liquid is condensating compared to the totally wetting case.

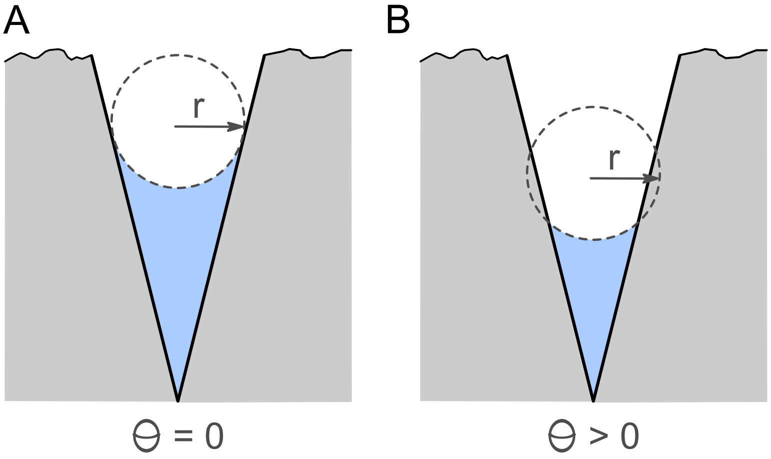

Figure 2.6: Capillary condensation of a liquid into a pore, for a totally wetting liquid with contact angle zero (A) and for a liquid with finite contact angle at the pore surface (B)

A main influence on the wetting behavior of liquids has the surface roughness of the particles. At low vapor pressures the capillary bridge is first formed at the outer most asperity. With increasing vapor pressure more and more bridges at asperities are formed. The capillary force is then proportional to the number of asperities. At high vapor pressures the capillary bridge acts over the total contact area and the influence of the surface roughness is negligible. This dependence of the wetting behavior on the surface roughness can drastically change the flow behavior of wet granulates or the adsorption of liquids on surfaces.

Pickering emulsion A special case of capillary bridging is a Pickering emulsion [39]. Here solid particles are bound at the interface of liquid droplets. The typical radius R_p of the particles is smaller or in the same size range as the droplet radius R_d (Fig.2.7). The binding energy of the particles at the surface is:

$$E_{bind} = \pi R_p^2 \gamma_{ll} \cdot (1 - |\cos(\Theta_{ll})|)^2 \tag{2.25}$$

with Θ_{ll} the contact angle of the interface on the particle surface.

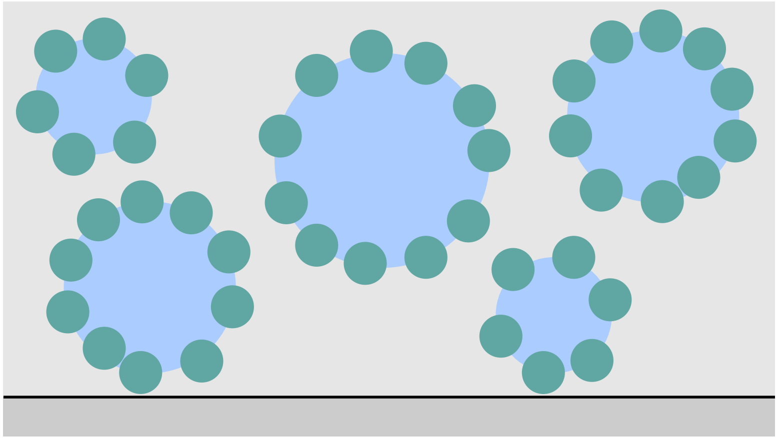

Figure 2.7: Pickering emulsion droplets (blue) stabilized by solid particles (green). The stabilizing particles are in the same size range as the emulsion droplets

Determination of capillary forces

The capillary force strongly depends on the geometry of the capillary bridge and the shape of the involved solid surfaces. For the calculation of these forces the geometry and boundary conditions, e.g. constant bridge volume or vapor pressure have to be known. In general a full analytical solution for the capillary force is hard to obtain. Hence depending on the boundary conditions different approximations are used. For small menisci and negligible gravitation the radii of curvature can be approximated by circles. This is called the "circular approximation" [40, 41]. For the capillary force between a sphere of radius R_p and a planar surface, when the vapor phase and the liquid are in equilibrium (Fig.2.8), one obtains [42]:

$$F \approx 2\pi\gamma_l R_p \left(\cos\Theta_1 + \cos\Theta_2 - \frac{D}{r_1}\right) \tag{2.26}$$

For a constant volume V of the liquid bridge the capillary force is [43]

$$F \approx 2\pi\gamma_l R_p (\cos\Theta_1 + \cos\Theta_2) \left(1 - \frac{D}{\sqrt{D^2 + \frac{V}{\pi R_p}}}\right) \tag{2.27}$$

Figure 2.8: Spherical particle with radius R_P at distance D from a planar wall. A liquid forms a meniscus between the sphere and the wall with a curvature radius r_1. Θ_1 and Θ_2 are the contact angles of the liquid on the particles and wall surface

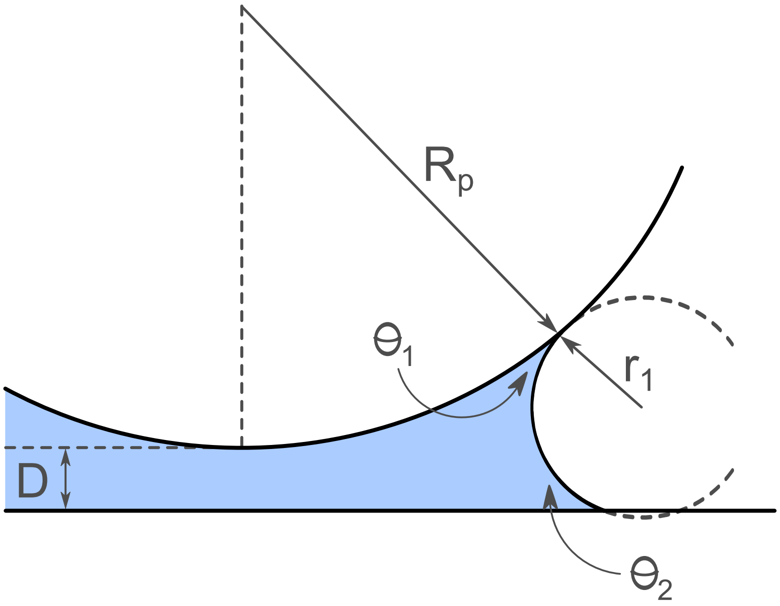

In both cases the capillary force gets weaker with increasing separation distance D. If the volume in Eq.2.27 is increased (at constant separation distance), the capillary force is also increasing. This is due to the increased cross-sectional area of the meniscus over which the Laplace pressure is acting.
Capillary forces between two spheres can be calculated in the same way by exchanging in Eq.2.26 and Eq.2.27 R_P with an effective radius

$$R^* = R_1 R_2/(R_1 + R_2) \tag{2.28}$$

with R_i the radius of sphere i. For many other geometries the capillary force has been derived, an overview can be found in [44].

2.2.4 Hydrodynamic Forces

Considering a liquid volume $dV = dxdydz$ between two parallel plates of area A. When moving one plate with a shear force $\vec{F}$ parallel to the second one, the flow of the interstitial liquid is not uniform, but a gradient in the shear rate $\dot{\gamma}$ is built up (Fig.2.9). The

Figure 2.9: Moving a plate parallel to a second plate with a shear force $\vec{F}$. A gradient in the shear rate $\dot{\gamma}$ is build up in the interstitial liquid

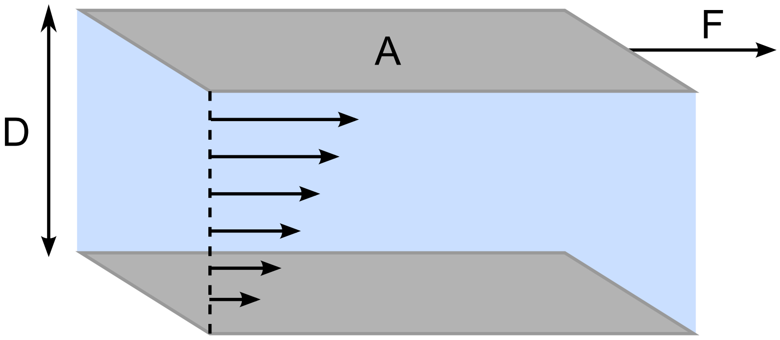

relation between the required shear force and the shear rate can be described by

$$\frac{F}{A} = \eta \underbrace{\frac{\Delta v}{D}}_{\dot{\gamma}} \tag{2.29}$$

with η the liquids viscosity and Δv the velocity difference tangential to the plate orientation. This relation is only valid for laminar flows, i.e. for small gap distances Δz and small velocities Δv. Laminar flow is dominant, when the inertia force is small compared to the friction force, caused by the liquids viscosity. The ratio between the inertia force and the friction force is called Reynolds number.

$$Re = \frac{\varrho_l \overline{v} L}{\eta} \tag{2.30}$$

with $\overline{v}$ the typical velocity of the liquid and L the length scale on which the liquid velocity is changing. The Reynolds number is a criterion, whether the flow is laminar or turbulent. If $Re \ll 1$ then the flow is laminar, while for larger Reynolds number the flow is more turbulent. The timescale τ_{lam}, on which a laminar flow is decaying is dependent on the liquid viscosity and density:

$$\tau_{lam} = \frac{\varrho_l L^2}{\eta} \tag{2.31}$$

Navier-Stokes equation

Quantitatively the flow of an incompressible Newtonian liquid is described by the Navier-Stokes equation. It has two main contributions. The first contribution is the viscous force $\eta \vec{\nabla}^2 \vec{v} \cdot dV$ (Fig.2.10), with an infinitesimal volume element dV. The viscous force is caused by a gradient in the shear rate $\dot{\gamma}$ of the liquid. The second contribution is a force due to a pressure gradient $-\left(\vec{\nabla} P\right) dV$, acting on the opposing sides of dV. The net force dF_x acting on the surfaces of the volume element is:

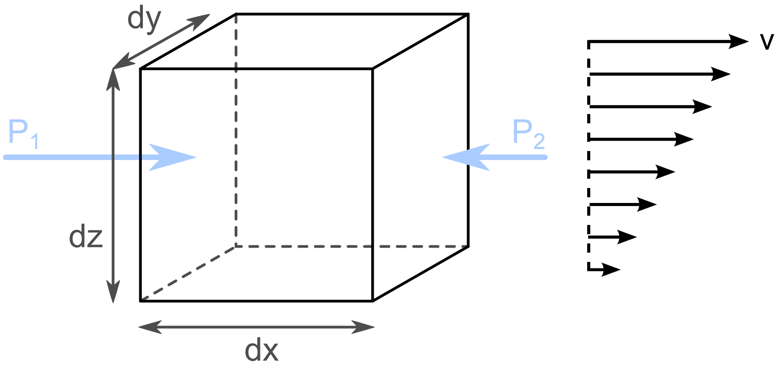

Figure 2.10: Liquid volume element dV in a flow field with liquid velocities $\vec{v}$. The flow is along the x-direction with the velocity gradient in z-direction. The pressure gradient is acting on the opposing sides of the volume element in the flow direction

$$dF_x = \eta \vec{\nabla}^2 \vec{v} \cdot dV - \left(\vec{\nabla} P\right) dV \tag{2.32}$$

Additionally one has to consider external forces $\vec{F}_{ext}$, like gravitational forces. According to Newton's law the Navier-Stokes equation in the lab fixed coordinate system is

$$\varrho_l \left[\frac{\partial \vec{v}}{\partial t} + \left(\vec{v} \cdot \vec{\nabla} \right) \vec{v} \right] = \eta \vec{\nabla}^2 \vec{v} - \vec{\nabla} P + \vec{F}_{ext} \tag{2.33}$$

As mass is conserved, the continuity equation is valid:

$$\vec{\nabla} \cdot \vec{v} = 0 \tag{2.34}$$

Hydrodynamic forces on rigid objects

The force acting on objects due to a liquid flow depends on the geometry. A sphere of radius R_p moving with a constant velocity $\vec{v}_p$ relative to the surrounding liquid feels a hydrodynamic drag force. This force is described by the Stokes law.

$$\vec{F} = -6\pi\eta R_p \vec{v}_p \tag{2.35}$$

As a consequence for an object moving towards a wall in normal direction, the hydrodynamic drag force is increasing, as liquid has to be pushed out of the gap between object and wall. Particles in a laminar flow are dragged with it, when the particle inertia is small enough. The timescale τ_{drag} of a particle being dragged with the laminar flow is

$$\tau_{drag} = \frac{4\varrho_s R_p^2}{6\eta} \tag{2.36}$$

with ϱ_s the mass density of the sphere.

Hydrodynamic interaction at the liquid-liquid interface

Hydrodynamic forces occur not only near solid surfaces, but also between fluid interfaces. When moving the liquid-liquid interfac, due to the strong hydrodynamic forces a deformation of the interface is observed. For droplets in a surrounding liquid this deformation leads to an increase of the interface, as the droplet volume is conserved. The energy for increasing the surface and deforming the droplet shape is stored inside the droplet. When exposed to a further deformation or when relaxing to the equilibrium shape, the stored deformation energy could be released and can build up a laminar flow around the droplet due to the moving interface.

2.2.5 Gravitation vs Diffusion

Depending on the size range additionally sedimentation or diffusion can play a role in the particle motion. For small particles, smaller than 500nm, usually Brownian motion is significant. For large particles, larger than 10µm, sedimentation due to gravity is dominant. In the intermediate size range a combination of both motions can occur. To estimate which of both motions is dominant, often the Peclet number Pe is used. It is a dimensionless number, which describes the ratio between advective and diffusive motion.

$$Pe = \frac{\tau_b}{\tau_s} \tag{2.37}$$

with τ_b and τ_s the typical timescales for Brownian motion and sedimentation.
The diffusion of spherical particles in a liquid with viscosity η is described by the Einstein-Smoluchowski equation [45, 46]:

$$D = \frac{k_B T}{6\pi\eta R_p} \tag{2.38}$$

The typical timescale for a particle to diffuse over a distance of its own particle radius R_p is hence:

$$\tau_b = \frac{R_p^2}{D} \tag{2.39}$$

When a particle is sedimenting in the same liquid, the timescale for the sedimentation over a distance of one particle radius is

$$\tau_s = \frac{R_p}{v_s} \tag{2.40}$$

with v_s the sedimentation velocity. When the particle has reached a constant sedimentation velocity the gravitation force F_g and the friction force F_f from the surrounding liquid acting on the particle are balanced.

$$F_g = m \cdot g = \frac{4}{3}\pi R_p^3 \Delta\,\varrho \cdot g \equiv 6\pi\eta R_p \cdot v_s = F_f \tag{2.41}$$

with $\Delta\varrho$ the density difference between the sphere and the surrounding liquid. Combining the two timescales the Peclet number is:

$$Pe = \frac{4\pi R_p^4 \Delta\varrho g}{3 k_B T} \tag{2.42}$$

In the case $Pe \ll 1$ the gravitation negligible and the particles are mainly diffusing, while for $Pe \gg 1$ the gravitation is dominant.

2.3 Contact Mechanics of Single Particles

2.3.1 Introduction to Contact Mechanics

Contact mechanics is the science of solid objects in contact and their behavior under mechanical load [47]. If a solid object is exposed to mechanical loads, i.e. when forces are acting onto the surfaces, the object is feeling a so-called "stress" σ. Exposed to stresses the object reacts with elongations and displacements u_i of parts of its volume along different axes i. This leads to a deformation of its shape and a volume change. A measure of the relative deformation is the so-called "strain" ϵ. Contact mechanics now try to describe the relationship between stress and strain and the dependence on material parameters like elasticity.

Uniaxial stress Considering a 2-dimensional volume with length L_x in x-direction (Fig.2.11). An applied stress σ_x along the x-axis leads to an elongation Δu_x. For an uniaxial deformation the strain is then defined as

$$\epsilon_x = \frac{\partial u_x}{\partial x}, \qquad \epsilon_y = \frac{\partial u_y}{\partial y}, \qquad \epsilon_z = \frac{\partial u_z}{\partial z} \tag{2.43}$$

with ∂u_i the relative displacement of the object along the axis i.

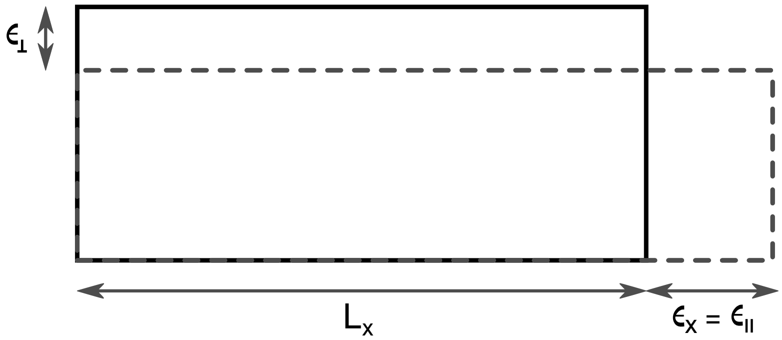

Figure 2.11: Volume element with lateral length L_x elongated along the x-axis. An elastic elongation along the x-axis and a contraction perpendicular to that occured

Up to a critical stress σ_c this elongation is reversible, which means that when the stress is decreased or removed, the volume comes back to its original length. This range of reversible elongations Δu_x and possible strains ϵ_x is called elastic regime (Fig.2.12). Exceeding the critical stress the object is plastically deformed. In the elastic regime for most materials objects show a tangential contracting when they are elongated along the normal direction. This happens at a critical tensile stress σ_{tens} and is called Poisson effect [48]. The Poisson ratio ν_p is a material parameter and describes the amount of contraction strain $\epsilon_\perp$ compared to the normal strain $\epsilon_\parallel$.

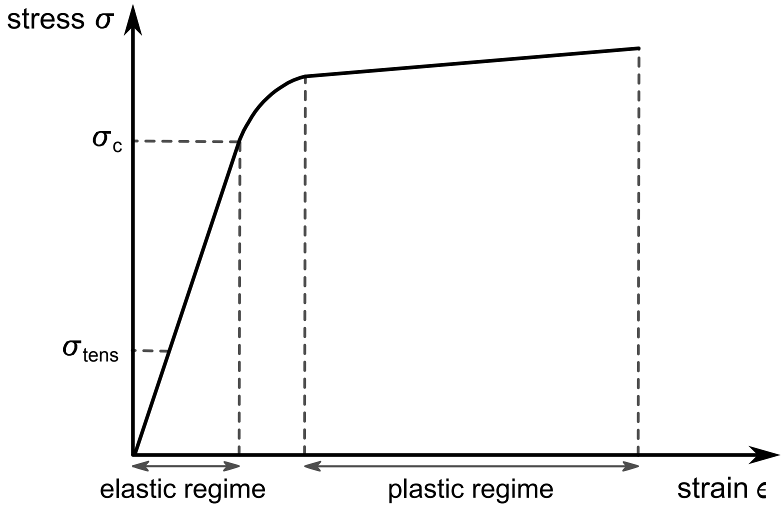

Figure 2.12: Schematic stress-strain diagram. Up to a critical stress a linear response to the stress is observed, which is called the elastic regime. Afterwards at higher stresses the material deforms plastically

$$\nu_p = -\frac{\epsilon_\perp}{\epsilon_\parallel} \tag{2.44}$$

The maximum value is 0.5 and is for a perfectly incompressible volume. Typical values for the poisson ratio are in the range of 0.2-0.3. There exist also elastic and isotropic materials with negative Poisson's ratio, showing a contraction perpendicular to the compression direction [49].

For isotropic materials there is a linear relationship between the applied stress σ_x and the strain ϵ_x.

$$\sigma_x = \mathcal{E}\epsilon_x \tag{2.45}$$

with $\mathcal{E}$ the elasticity or Young's modulus. Typical values of the Young's modulus for soft materials as polymers are a few GPa, around 70GPa for fused silica and roughly 1200GPa for diamond. Very often when considering the contact between two materials A and B a reduced Young's modulus $\mathcal{E}^*$ is used.

$$\mathcal{E}^* = \left(\frac{1-\nu_{p,A}^2}{\mathcal{E}_A} + \frac{1-\nu_{p,B}^2}{\mathcal{E}_B}\right)^{-1} \tag{2.46}$$

with Young's moduli $\mathcal{E}_i$ and Poisson ratios $\nu_{p,i}$ of the materials A and B.

Tri-axial stress For the non uniaxial case, the forces are acting on all surfaces of the object into arbitrary directions. Considering an infinitesimal small volume element $dV = dxdydz$ submitted to forces $F_i = (F_{ix}, F_{iy}, F_{iz})$ (Fig.2.13). The first subscript describes the direction of the surface normal, the second subscript the direction of the force component. The stress can be divided into two categories, normal and tangential stresses. Normal stresses σ_{ii} occur, when the force component act in normal direction onto the volume elements plane, i.e. parallel to the surface normal.

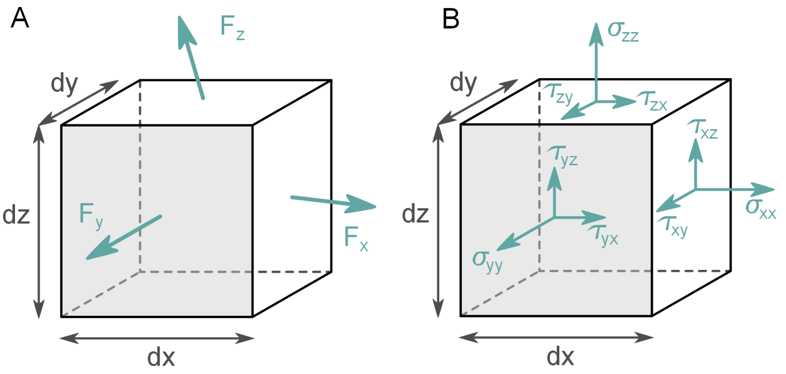

Figure 2.13: Volume element dV with acting forces and the resulting normal and tangential stresses

$$\sigma_{xx} = \frac{dF_{xx}}{dydz}, \qquad \sigma_{yy} = \frac{dF_{xy}}{dzdx}, \qquad \sigma_{zz} = \frac{dF_{xz}}{dxdy} \tag{2.47}$$

with dF_{ij} the force components acting along axis j on the plane with surface normal along i. Tangential stresses, also called shear stresses are acting parallel to the plane. For a force acting along the x-axis onto a perpendicular plane the shear stress is:

$$\tau_{yx} = \frac{dF_x}{dxdz} \tag{2.48}$$

The total stress at an arbitrary point within the object is then a combination of normal and tangential stresses and can be described with the stress tensor

$$\underline{\underline{S}} = \begin{pmatrix} \sigma_{xx} & \tau_{xy} & \tau_{xz} \\ \tau_{yx} & \sigma_{yy} & \tau_{yz} \\ \tau_{zx} & \tau_{zy} & \sigma_{zz} \end{pmatrix} \tag{2.49}$$

The deformation of an object, subjected to such stresses is usually not uniaxial, but the object is distorted in 3D under the stress. Normal strains are in this case defined analog to the uniaxial case, i.e.

$$\epsilon_{xx} = \frac{\partial u_x}{\partial x}, \qquad \epsilon_{yy} = \frac{\partial u_y}{\partial y}, \qquad \epsilon_{zz} = \frac{\partial u_z}{\partial z} \tag{2.50}$$

The deformations along tangential axes are then described with the shear strains.

$$\epsilon_{xy} = \frac{1}{2}\left(\frac{\partial u_x}{\partial y} + \frac{\partial u_y}{\partial x}\right) \tag{2.51}$$

$$\epsilon_{yz} = \frac{1}{2}\left(\frac{\partial u_y}{\partial z} + \frac{\partial u_z}{\partial y}\right) \tag{2.52}$$

$$\epsilon_{zx} = \frac{1}{2}\left(\frac{\partial u_z}{\partial x} + \frac{\partial u_x}{\partial z}\right) \tag{2.53}$$

The complete deformation at an arbitrary point within the object is described by the strain tensor

$$\underline{\underline{\epsilon}} = \begin{pmatrix} \epsilon_{xx} & \epsilon_{xy} & \epsilon_{xz} \\ \epsilon_{yx} & \epsilon_{yy} & \epsilon_{yz} \\ \epsilon_{zx} & \epsilon_{zy} & \epsilon_{zz} \end{pmatrix} \tag{2.54}$$

which is a symmetric tensor of rank two. In general stress and strain are then related by a matrix of constants $\mathcal{E}_{ijkl}$.

$$\sigma_{ij} = \mathcal{E}_{ijkl}\epsilon_{kl} \tag{2.55}$$

For normal stresses and strains the relationship can be described with a combination of the Young's modulus and the Poisson ratio.

$$\epsilon_{xx} = \frac{1}{\mathcal{E}} \cdot \left[\sigma_x - \nu_p\left(\sigma_y + \sigma_z\right)\right] \tag{2.56}$$

and analog for the normal strains along the y- and z-axis.

$$\epsilon_{xy} = \underbrace{\frac{\mathcal{E}}{2(1+\nu_p)}}_{G} \tau_{xy} \tag{2.57}$$

with G the shear modulus, indicating the resistance of the object to shear.

Nanoindentation

For measuring the elastic and plastic properties of materials a technique called "nanoindentation" is widely used [47]. Thereby an indentation tip with predefined tip geometry is pressed into the material of interest. The indentation process is performed in two steps, a loading with a compressive force and an unloading step. During the whole process the indentation depth δ and the normal force acting on the tip is recorded. From the resulting force-depth curve (Fig.2.14) mechanical properties, e.g. Young's modulus or the hardness H can be obtained. During the loading the material is deformed elastically and plastically. The force needed to reach the maximum indentation depth δ_{max}, normalized with the projected area A_{pro} describes the hardness of the material. During the unloading the tip is retracted out of the material, which recovers partially its shape. This is an elastic recovery of the material from which the Young's modulus can be calculated.

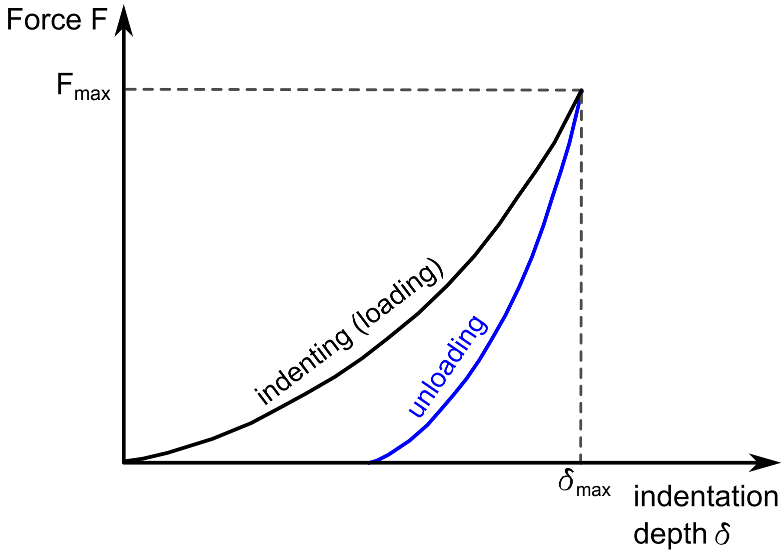

Figure 2.14: Schematic force-depth curve of a nanoindentation with loading and unloading part. The hardness is described by the maximum force at maximum indentation depth

2.3.2 Adhesion

When two objects are in contact, a certain force is required to separate the two objects. This force is called adhesion force F_{adh} and is the sum of all attractive forces.

$$F_{adh} = F_{VdW} + F_{el} + F_{cap} + ... \tag{2.58}$$

with F_{VdW} the Van der Waals force, F_{el} an electrostatic force and F_{cap} the capillary force. Due to the surface roughness the real surface over which the attractive forces are acting is smaller than the apparent surface. Hence the experimentally determined adhesion forces are smaller than the theoretically obtained forces.
For example the adhesion force between a sphere and a plane [42, 52] is

$$F_{adh} = -2\pi R_p w_{adh} \tag{2.59}$$

with w_{adh} the adhesion energy per area.

The contact mechanics between two elastic spheres (Fig.2.15) in the presence or absence of adhesion is described by various models, e.g. the Hertz, the JKR or the DMT model. They relate contact parameters, e.g. the contact radius a_c or indentation depth δ with the elastic properties of the spheres. For these models different assumptions concerning the interactions between the spheres in and outside the contact area were made.

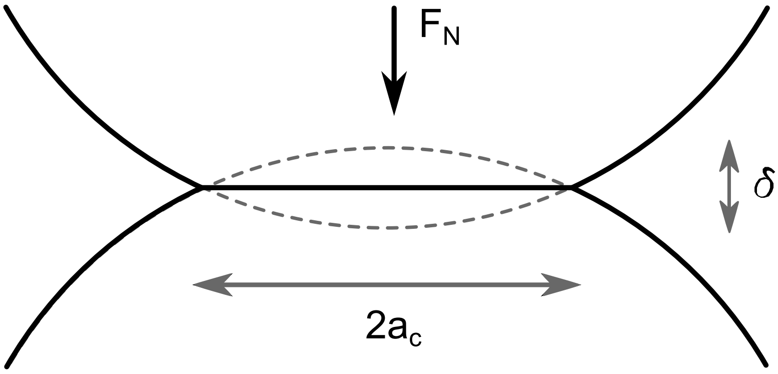

Figure 2.15: Elastic deformation of two contacting spheres. The contact is loaded with a normal force F_N, creating a contact zone of radius a_c with an indentation depth δ

Hertz model In the Hertz theory [53] the contact was assumed to be frictionless and with the absence of tensile stresses. Further surface forces, e.g. adhesion in and outside the contact area were neglected. For small contact areas with $a_c << R_i$ the contact radius can be described with

$$a_c = \frac{3F_N R^*}{4\mathcal{E}^*} \tag{2.60}$$

with R^* the reduced radius (see Eq.2.28), $\mathcal{E}^*$ the reduced Young's modulus and F_N the normal force onto the contact area. The normal force required to reach a certain indentation depth δ is

$$F_N(\delta) = \frac{4}{3}\mathcal{E}^*\sqrt{R^*}\delta^{\frac{3}{2}} \tag{2.61}$$

with an indentation depth

$$\delta = \frac{a_c^2}{R^*} \tag{2.62}$$

These equations are only valid for small contact areas ($a_c << R_i$). For large indentation depth δ this is often not the case. The resulting strains are here no longer in the elastic regime and plastic deformation of the spheres occurred. Ting [54] and Sneddon [55] studied the indented a elastic half-space with a sphere to study the limits of the Hertz theory. They concluded that the Hertz theory was valid up to a value of $a_c/R_p < 0.4$.

JKR model An improvement of the Hertz theory was provided by Johnson, Kendall and Roberts in 1971 [56]. In their so-called JKR-theory they took additional surface forces inside the contact area into account, which were neglected in the Hertz theory.

Further interactions outside the contact were not considered.
The obtained distribution of the normal stress σ_N along the contact width $2a_c$ is a sum of the distributions of a Hertzian contact with loading force $F_{N,Hertz}$ and of a flat indenter (see Sec.3.2) contact with tensile force $(F_{N,Hertz} - F_{N,JKR})$. In the inner part of the contact area, roughly up to $0.8a_c$, compressive stresses are acting, while in the rim zone tensile stresses are present. The adhesive force between two spheres with reduced radius R^* is

$$F_{adh} = -\frac{3}{2}\pi R^* w_{adh} \tag{2.63}$$

Compared to a Hertzian contact, the contact area and the indentation depth are in the JKR model increased.

DMT model In 1975 an alternative contact model was proposed by Derjaguin, Muller and Toporov, called DMT-theory [57]. They assumed that inside the contact area the mechanics would follow the Hertzian theory. Outside the contact in an annular ring called the cohesive zone additional attractive forces such as Van der Waals should be present. It was assumed that these additional forces do not deform the cohesive zone.
For the calculation of the contact radius and the indentation depth the additional surface forces were just added to the acting normal forces in the Hertz theory. With that the adhesion force was calculated to be

$$F_{adh} = -2\pi R^* w_{adh} \tag{2.64}$$

which is 1.33 times larger than in the JKR theory.

There were discrepancies between the JKR- and the DMT-theory. The JKR-theory considered no surface forces outside the contact area, but allowed deviations from the Hertzian theory concerning deformations of the contact area. Hence the JKR-theory was suited for large soft spheres and high adhesion energies w_{adh}. In contrast the DMT-theory took additional surface forces outside the contact area into account, but considered no deformations by these forces. The DMT-theory was best for small hard spheres and low adhesion energies w_{adh}. Further models try to describe the transition between the JKR- and the DMT-theory, for example Maugis in 1992 [58]. He explained the transition between the two models by using a dugdale (square well) interaction potential.

Adhesion force measurements

For the measurement of adhesion forces several techniques are approved. Widely used is centrifugation [59]. The particles are mounted on surfaces on a ultracentrifuge and the centrifugal force for particle detachment is measured. After each run at a certain rotation speed the surface is imaged to control if particles have detached. This method is limited in the rotation speed of the ultracentrifuge. Due to this only particles larger than a few micrometers could be measured. Newer methods using a Hopkinson bar are able to measure higher adhesion forces for smaller particles in the size range between roughly 1µm and 10µm [60]. A further method for adhesion measurements is to use a

AFM with the colloidal probe technique. The particles are glued onto a cantilever and pressed onto a surface. The force required to detach the particles is recorded.
From optical measurements of the contact area, e.g. with a scanning electron microscope (SEM), contact radius and indentation depth can be measured, from which adhesion forces can be deduced [61].

2.3.3 Friction

Friction describes the force which hinders and slows down the relative motion between two interacting macroscopic objects. One distinguishes between the static and the dynamic friction. The static friction has to be overcome before two objects can move relative to each other. Once the objects are in motion, the dynamic friction slows down this motion and is hence smaller than the static friction. In 1699 Amontons formulated that the lateral friction force F_L is proportional to the applied normal force F_N, but independent from the contact area.

$$F_L = \mu F_N \tag{2.65}$$

with μ the friction coefficient. The independence of the friction force from the contact area can be explained by considering the influence of the surface roughness. Due to this the real contact area A_{real} is smaller than the apparent contact area A_{app}. When an object is now sliding over a surface, the friction force is proportional to the real contact area:

$$F_L = \tau_c \cdot A_{real} \tag{2.66}$$

with τ_c the yield stress during the sliding. Combining Eq.2.65 with Eq.2.66 this proportionality leads to a linear decrease of the real contact area with increasing applied normal force.
Two different models describe the influence of the surface roughness in detail: The Bowden-Tabor model and the Greenwood-Williams model.

Bowden-Tabor model Bowden and Tabor formulated a model which describes plastic deformation of the surface asperities as the source of the change in A_{real} during loading [62]. When the normal force exceeds a critical normal stress σ_c, plastic deformation sets in. A further increase of F_N leads to a linear increase of the real contact area, while the normal stress remains constant. The friction coefficient was calculated with that to

$$\mu = \frac{\tau_c}{\sigma_N} \tag{2.67}$$

resembling Antomons' law (see Eq.2.65).

Greenwood-Williams model Greenwood and Williams assumed an elastic deformation of the surface asperities following the Hertz theory [63]. They modeled the asperities as spherical caps with identical radii of curvature but different heights, resembling a Gaussian height distribution. With that they obtained the linear dependence of the real contact area with the applied normal force and hence Antomons' law.

Usually the friction increases, when adhesion gets stronger. As the adhesion force acts also normal to the contact area, it simply can be added to the applied normal force, when calculating the friction:

$$F_L = \mu \left(F_N + F_{adh} \right) \tag{2.68}$$

For macroscopic objects the adhesion force is small compared to the applied normal force and can then be neglected.

Rolling friction

The dynamic friction can be divided in two components. The sliding friction occurs, when two objects move transversal against each other. During rolling friction an object, e.g. a sphere, is slowed down when rolling over a surface. Experimentally it was observed that the rolling friction was smaller than the sliding friction. The origin of the rolling friction is an energy dissipation during the rolling. This energy dissipation has different contributions. One is plastic deformation of the contact area at high normal and tangential stresses [64]. A further contribution is an adhesion hysteresis. During the rolling new contact in front the object are formed, while at the back side the existing contacts are breaking. Depending on the kind of interaction the breakage of the contact leads to an energy dissipation [65]. A third contribution comes from an additional sliding of the objects during rolling. When the two objects have different elastic properties, i.e. Young's moduli, they are differently stretched and hence slide against each other [66].

The rolling friction is proportional to the applied normal force and inverse proportional to the radius R_r of the rolling object:

$$M = \mu_r \frac{F_N}{R_r} \tag{2.69}$$

with M the torque of the rolling object. In analogy to Antomons' law often a dimensionless rolling friction coefficient is used.

$$F_L = \mu_r F_N \tag{2.70}$$

Friction force measurements

For measuring friction forces often so-called tribometers are used. A sharp tip is pointing onto the material of interest, which is placed on a rotating disk. During the disk rotation the material is moved under the tip, which scratched of the surface. The applied normal and resulting lateral force acting on the tip are measured and friction coefficients calculated. Further techniques for friction force measurements are using the SFA or the AFM with the colloidal probe technique (see Sec.2.2.1).

In detail sliding friction for particles can be examined by using ultracentrifugation as for adhesion force measurements (see Sec.2.3.2). The particles are not mounted in centrifugal force direction, but on a perpendicular plane. The loading normal force is then the gravitation. At a certain rotation speed the particles are sliding off the surface and the corresponding lateral force and sliding friction coefficient can be obtained.

For measuring rolling friction particles should be able to rotate freely. This can be obtained by using commercial nanoindentation devices (for details see Sec.4.1.2). The particles are pressed with a flat punch indenter tip onto a surface and are rolled laterally. From the resulting lateral force acting onto the indenter the rolling friction coefficient is deduced.

Typical values for sliding friction are in the range between 0.02 and 0.60 and can exceed also values larger than one [67]. Rolling friction coefficients are explicitly smaller than sliding friction coefficients and are dependent on the radius of the rolling object. They are typically lying in the order of 10^{-3}m [44].

2.4 Granulate Bulk Phenomena

2.4.1 Contact Mechanics in Granulates

As observed for macroscopic solids, bulk granulates at rest can exhibit different stresses along different directions. As a consequence, when a granulate volume element is loaded with a vertical stress σ_v, a horizontal stress σ_h is set up (Fig.2.16A), with the resulting horizontal stress being smaller than the vertical one. The ratio between horizontal and vertical normal stress is called “lateral stress ratio” K and is a characteristic value of the considered bulk granulate.

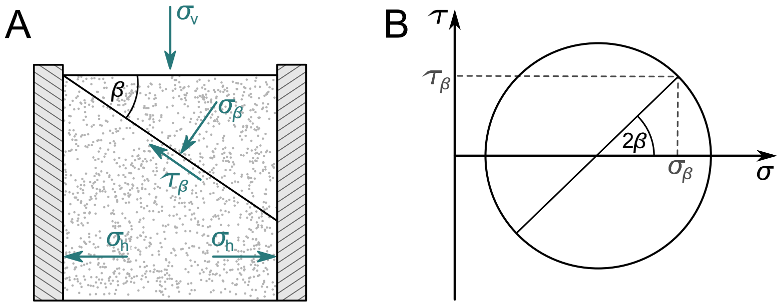

Figure 2.16: Granulate volume element loaded with a vertical stress and horizontal stresses acting onto the side walls (A). The normal stresses generate tangential stresses on planes inside the bulk. The resulting stress-strain relations are described by Mohr’s circle (B)

$$K = \frac{\sigma_h}{\sigma_v} \tag{2.71}$$

It is assumed that on the surfaces of the volume element only normal stresses are acting. Inside the bulk they can also generate tangential stresses.

The stresses, which can occur on an arbitrary plane under an angle β (Fig.2.16) can be calculated with

$$\sigma_\beta = \frac{\sigma_v + \sigma_h}{2} + \frac{\sigma_v + \sigma_h}{2} \cdot \cos(2\beta) \tag{2.72}$$

and

$$\tau_\beta = \frac{\sigma_v - \sigma_h}{2} \cdot \sin(2\beta) \tag{2.73}$$

The pairs of values (σ_β,τ_β) form a circle in the σ-τ diagram, which is called "Mohr's circle" (Fig.2.16B).

All the stresses acting on the volume element lead to a deformation of the bulk. Usually in granular systems elastic deformations of the bulk are small compared to plastic deformations and can hence be neglected in most cases. The main contribution to the plastic deformation of a bulk granular system is not from the deformation of single particle contacts, but from a particle rearrangement. During the plastic deformation particle contacts are breaking and relative motion of the particles against each other sets in. In this case a plastic deformation is usually called "flowing".

2.4.2 Granulates under Compression

When a granulate is compressed uniaxially, the bulk gets compacted and the volume fraction is increasing. Particle contacts get harder and more adhesive due to the compression. Particles oriented in chains along the compression direction exhibit predominantly large stresses compared to perpendicular oriented chains. These chains, where the stresses are dominating are called "force chains" (Fig.2.17).

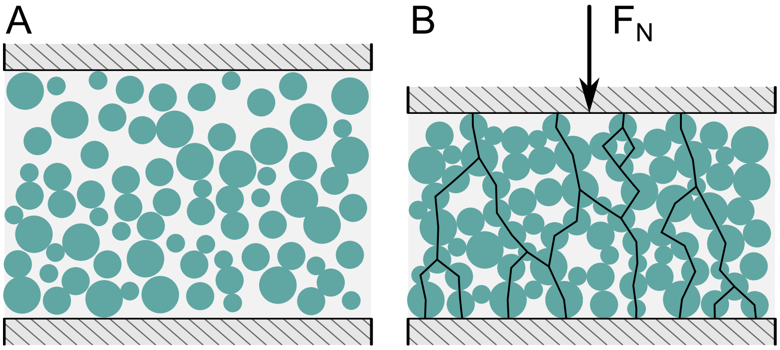

Figure 2.17: Stress distribution and force chains in granulates under uniaxial compression. The stress distribution is directed with the particle chains along the compression direction. The chains with dominating stress are called force chains

At a certain point a critical normal stress is reached and the granulate bulk starts to flow. Usually in closed compression cells the side walls confining the granulate volume are subjected to horizontal normal stresses σ_h (see Sec.2.4.1). In this geometry the lateral stress ratio K is constant during the compression. In compression cells with open boundaries the missing side walls can not carry the increasing horizontal stress during compression and the particles are squeezed out of the volume. This means that the granulate bulk is compressed along one direction, while expanding perpendicular to it. The lateral stress ratio K is then changing with ongoing compression in this geometry.

2.4.3 Granulates under Shear

For investigating the granulate bulk behavior under shear many different geometries of shear cells are available [3]. The most common shear cell in classical granular matter science is the Jenike cell [68], which uses a plate-plate geometry. The granular system is loaded with a constant normal stress σ_N and is then sheared. The upper shear plate is moved with a constant velocity $\vec{v}$ in one direction and the resulting tangential shear stress is measured. Depending on the initial particle number density, i.e. the volume fraction, different behavior of the granular bulk is observed.

Shear of a low density granulate Due to the initial loading with a normal stress, the granular bulk was slightly compacted and the initial volume fraction increased. With beginning shear the particles are pressed against each other and as a result the tangential stress increases (Fig.2.18A, region I). When the granular bulk starts to flow, the plastic deformation leads to a compaction of the structure, which is indicated with a volume fraction increase (region II). Granular systems, which get compacted under shear are called underconsolidated.

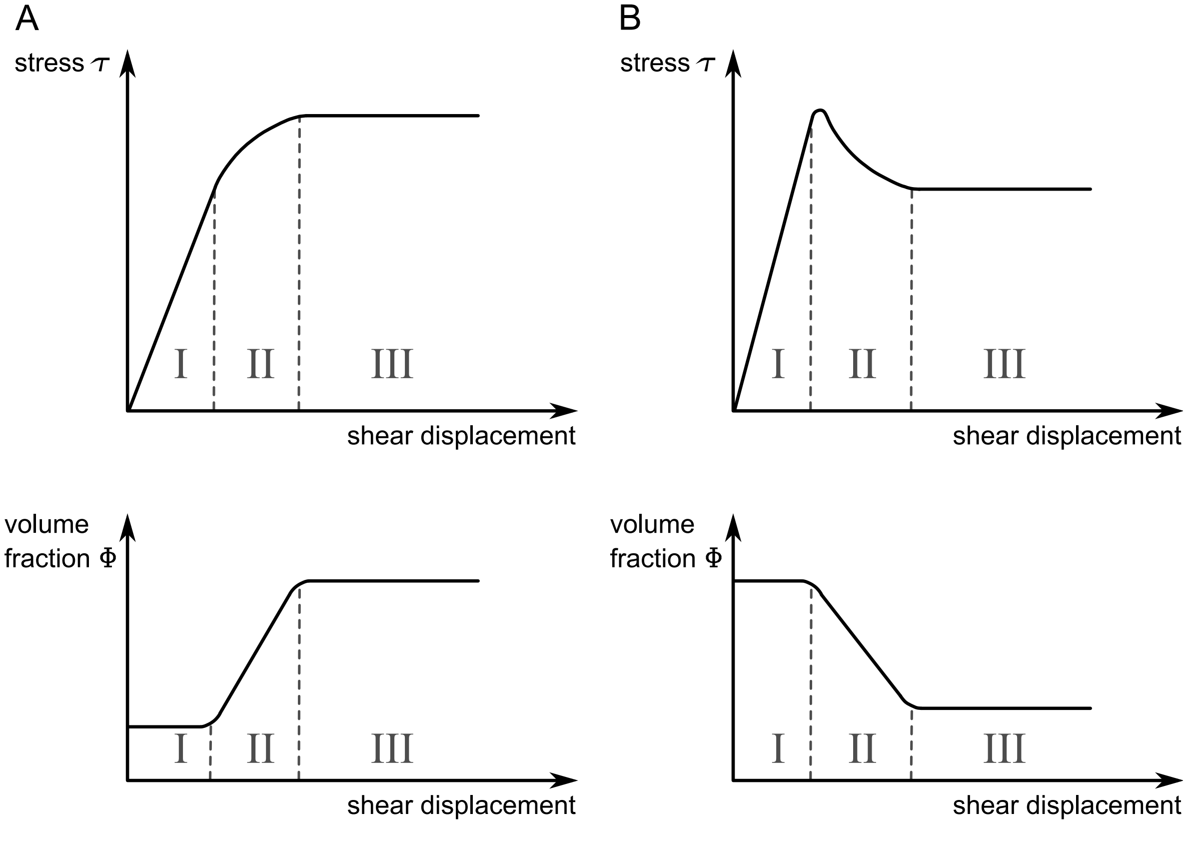

Figure 2.18: Dependence of tangential shear stress and volume fraction on the applied shear displacement for a underconsolidated granulate (A) and a overconsolidated granulate (B). In both cases at large shear displacements the steady state flow sets in with constant tangential stress and volume fraction (after [22])

At a certain point during the shear the tangential stress and the volume fraction remain constant (region III). The granular bulk flow in this regime is then a so-called "steady state flow". Granular systems, which show constant tangential stress and volume fraction during the shear are "critically consolidated".

Shear of a high density granulate In granulates with a high initial particle density the single particle contacts are very strong and cohesive due to a previous compaction. When this granular bulk is sheared afterwards the occurring tangential stress needs to be high enough to break the particle contacts and for moving the particles against each other. Before reaching this critical tangential stress the granular bulk is first only elastically deformed (Fig.2.18B, region I). At the critical shear stress a plastic deformation sets in and the granular bulk starts to flow. After the onset of flow the tangential shear stress drops down (region II). Further shearing of the sample leads to a loosening of the structure and the volume fraction decreases until a state of steady state flow is reached (region III). Granular systems where the structure gets looser under shear are called "overconsolidated". The granular flow is usually not observed for the whole bulk volume, but is localized in a small area, the "shear zone".

Shear zone formation

Areas, where a high particle flow and high dynamic single particle motions occur compared to the surrounding, are the so-called "shear zones". In these zones plastic deformation of the granular bulk occurs. In underconsolidated granular systems the tangential stresses are increasing with ongoing shear. Due to that the granular bulk gets compacted inside the shear zone. Adjacent areas to the shear zone can not bear the further increasing tangential stress and get also deformed and compacted. Due to that in underconsolidated granular systems the shear zone gets extended under shear.

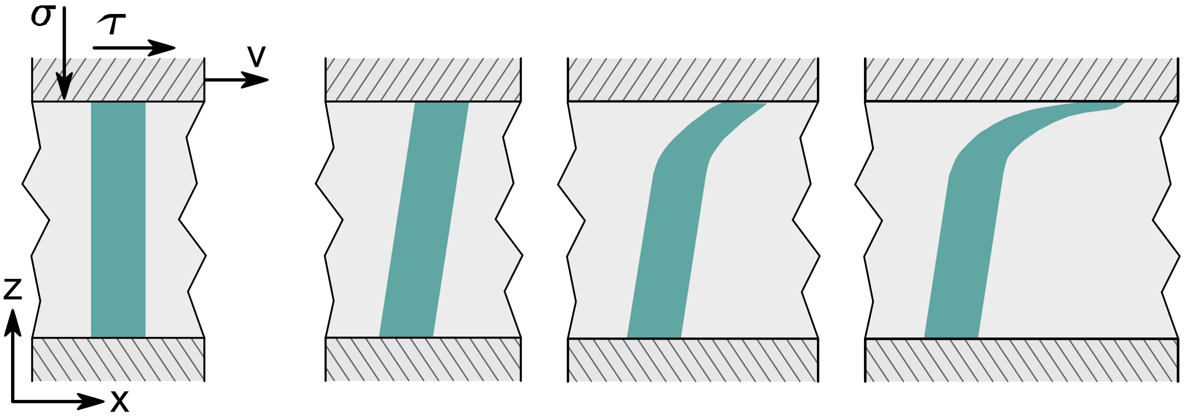

Figure 2.19: Localization of a shear zone near the upper shear plate, which is moved with constant velocity v. At the beginning of the shear the granulate is uniformly deformed. With ongoing shear the shear zone is narrowing and the granulate in the upper part is only flowing

Overconsolidated granular systems show a contrary behavior under shear. At the beginning the shear deformation is uniformly distributed along the sample height. At the point, when the granular bulk starts to flow, the tangential stress drops down and is not sufficient to loosen the adjacent granulate areas. With ongoing shear the shear zone is narrowing and gets more and more gets localized (Fig.2.19). This localization is predominantly occurring near the moving upper shear plate. This localization process gets enhanced, as the normal stress increases from top to bottom due to gravity. Lower tangential stresses are then required to deform the upper granulate part.
Independently from the initial particle density before the shear, once the steady state flow is reached, the tangential stresses are decreasing and the shear zone gets localized.

Shear dilatation

When shearing a overconsolidated granular bulk in a Jenike cell, the decrease of the volume fraction comes along with a volume expansion of the granular bulk. This effect is called “shear dilatation”. The reason for the volume expansion of the granular system is the rearing up of the force chains under shear (Fig.2.20). When sheared, the particles want to rearrange and move relative against each other. The force chains have to rear up, to generate a locally diluted region, where a lateral motion of the particles is possible. During further shearing the particles start to slide and roll against each other and the force chain is collapsing. At a certain point, the granular bulk is no longer expanding with ongoing shear and a maximum volume is reached. The rearing up and the collapsing of force chains are then in equilibrium. At the collapse of the force chains, the chain is reared up to its maximum height. The shear direction is then parallel to the averaged tangential plane of the particle chain contact. As a consequence shear dilatation, i.e. a volume expansion of the granular system only occurs, when the applied macroscopic shear plane is not identical with the averaged tangential plane of the particle contacts.

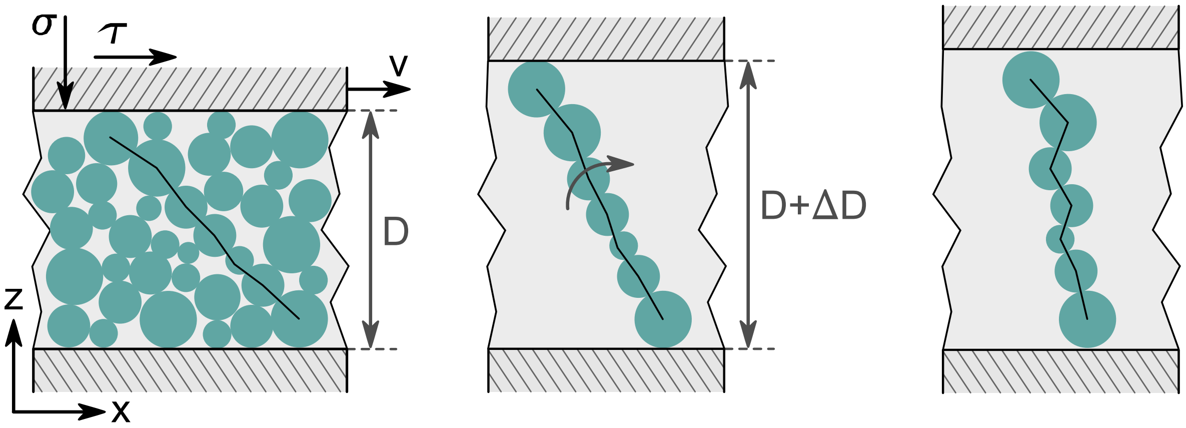

Figure 2.20: During shear dilatation the force chains in the granulate are rearing up to develop free volume for particle rearrangement. At maximum rearing up of the chains the granulate volume is fully expanded and stays constant

3 Experimental Devices

For obtaining the relationship between the macroscopic and microscopic behavior of granulate model systems, 3D imaging was combined with simultaneous mechanical testings. The 3D imaging was performed with laser scanning confocal microscopy [69, 70]. In this work a home-built laser scanning confocal microscope (LSCM) was used. A home-built setup compared to commercial available laser scanning confocal microscopes had the advantage that it was easily combinable with the mechanical testing device, as the beam path was freely accessible. The mechanical testings were performed with a home-built nano-manipulator (see Sec.3.2). With this device large mechanical deformations (compared to the particle size) could be applied, i.e. shear and compression. In contrast to commercially available nanoindenters, the used nano-manipulator had no force control. Hence all measurements in this work were performed strain-controlled.
In 2012 several extensions of the confocal microscopy setup have been made. The previous setup was extended by a second beam path. This enabled the visualization of different sample components, labeled with different dyes. The previous setup is indicated with “1-color mode LSCM”, while the new setup extension is referred as “2-color mode LSCM” or “2-color mode” in the following.

3.1 Laser Scanning Confocal Microscope

3.1.1 1-color mode LSCM

The 1-color mode setup of the home-built laser scanning confocal microscope (LSCM) [71, 72] contained only one illumination and detection line (Fig.3.1). The illuminating laser beam (Cobolt Samba, 532nm, 25mW maximum power, Cobolt AB, Sweden) was coupled over mirrors into the optical path. With the combination of a Glan-Thompson prism (PGT 2.08.05, Bernhard Halle Nachfl. GmbH, Germany) and a $\lambda/4$-plate (Linos, Germany) the laser beam was circularly polarized and slightly attenuated. The laser intensity could be adjusted with a neutral density filter wheel with transmittance from 0.1% to 100%. After passing a telescope the beam had a diameter of 8mm. A beam splitter splitted the laser beam into two main parts. One was directed onto a powermeter (PM100D compact power meter, Thorlabs GmbH, Germany), the second one was used for illuminating the sample. Additionally a small fraction was separated and directed onto a CCD camera (Philips Webcam SPC900NC VGA-CCD, Inmac GmbH, Germany), which was used for the detection of a sample reference signal for beam diagnosis. Here the reflection of the interface between the sample suspension and the bottom cover slide could be visualized. This reflection was a reference for the actual position of the focus

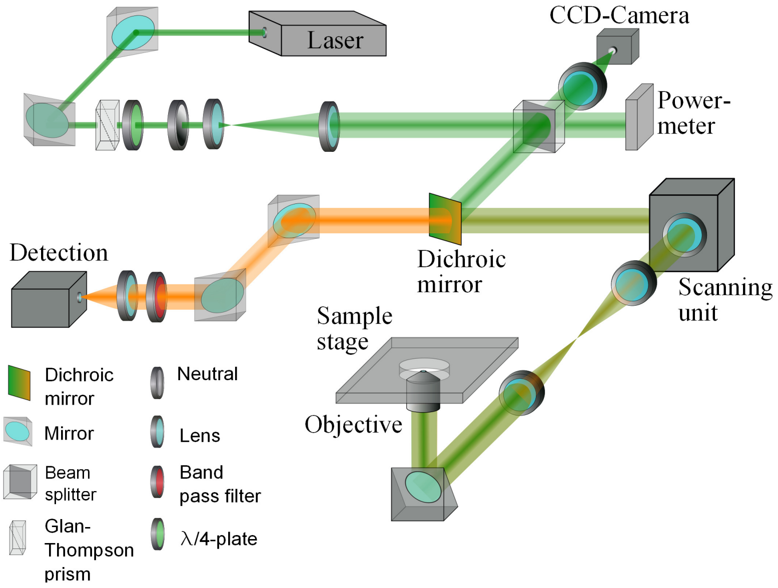

Figure 3.1: Schematic setup of the home-built 1-color mode laser scanning confocal microscope (LSCM). Devices for mechanical testings (e.g. nano-manipulator, Fig.3.5) can be placed onto the sample stage

point in the sample.

The sample was placed onto the sample stage, which was moved in x-y-z by stepping motors for a coarse positioning (miCos GmbH, Germany, and HVM 100 from OWIS GmbH, Germany, controlled with a LSTEP-PCI module, Lang GmbH & Co.KG, Germany). With a scanning unit (SCANcube7, SCANLAB AG, Germany) the sample was probed pointwise in x-y-plane with a frame rate of one to two frames per second. A telescope projected the pivot point of the scanning unit into the entrance of the objective (UPlanApo PH3, 100× oil immersion, NA=1.35, working distance 170µm, Olympus Deutschland GmbH, Germany). The z-position of the focus point in the sample was controlled by a piezo-actuator (nanoX 200 S, ENV 40 SG nanoX, Piezosysteme Jena GmbH, Germany), which drove the objective along the beam axis. The piezo-actuator had a maximum achievable displacement of 160µm with an positioning accuracy of 3nm. Due to that, the maximum height of a sample which can be scanned was 160µm. Laterally observation sizes up to 100µm could be achieved. During the 3D scanning the fluorescent dye molecules, which were incorporated in the particles (see Sec.4.1.1) were excited. The emitted fluorescent light was collected through the same objective and was separated from the illuminating beam after passing a dichroic mirror (Laser-beamsplitter z 532 RDC, 90% transmission above 545 nm, AFH Analysetechnik AG, Germany). A lens focused the detection beam onto the active area (diameter 20µm) of an avalanche photodiode (APD, id100, idquantique, Switzerland), which acted as the confocal pinhole. The detection signal was counted with a maximum count rate of 17MHz (NI PCI-6602 Counter/Timer, National Instruments Germany GmbH, Germany). As APDs work with a high quantum efficiency, only a low illuminating laser power of less than 1.5µW was needed. With this low laser power during the measurements also a bleaching of the fluorescent dyes could be avoided.

3.1.2 2-color mode LSCM

The new implementation of a second illumination and detection path (Fig.3.2) enabled measurements of different sample components, labeled with different fluorescent dyes. The second illumination laser beam (Sapphire 458 LP, 458nm, 20mW maximum power, Coherent (Deutschland) GmbH) was coupled over mirrors into the optical path. To superpose the two laser beams, an additional dichroic mirror was introduced between the lasers and the Glan-Thompson prism. The sample suspension could be illuminated simultaneously with both lasers or only with a single laser beam. For a larger observation volume, the previous objective was exchanged with an objective with a lower magnification (PLAPON 60XO, 60× oil immersion, NA=1.42, working distance 150µm, Olympus Deutschland GmbH, Germany). The observation size in lateral direction could be extended up to roughly 150µm.

To separate the informations of the different colored sample components in the fluorescent beam path, a further dichroic mirror was used (Fig.3.2, gray detection box). This dichroic mirror was transparent for wavelength below 500nm and above 550nm. For

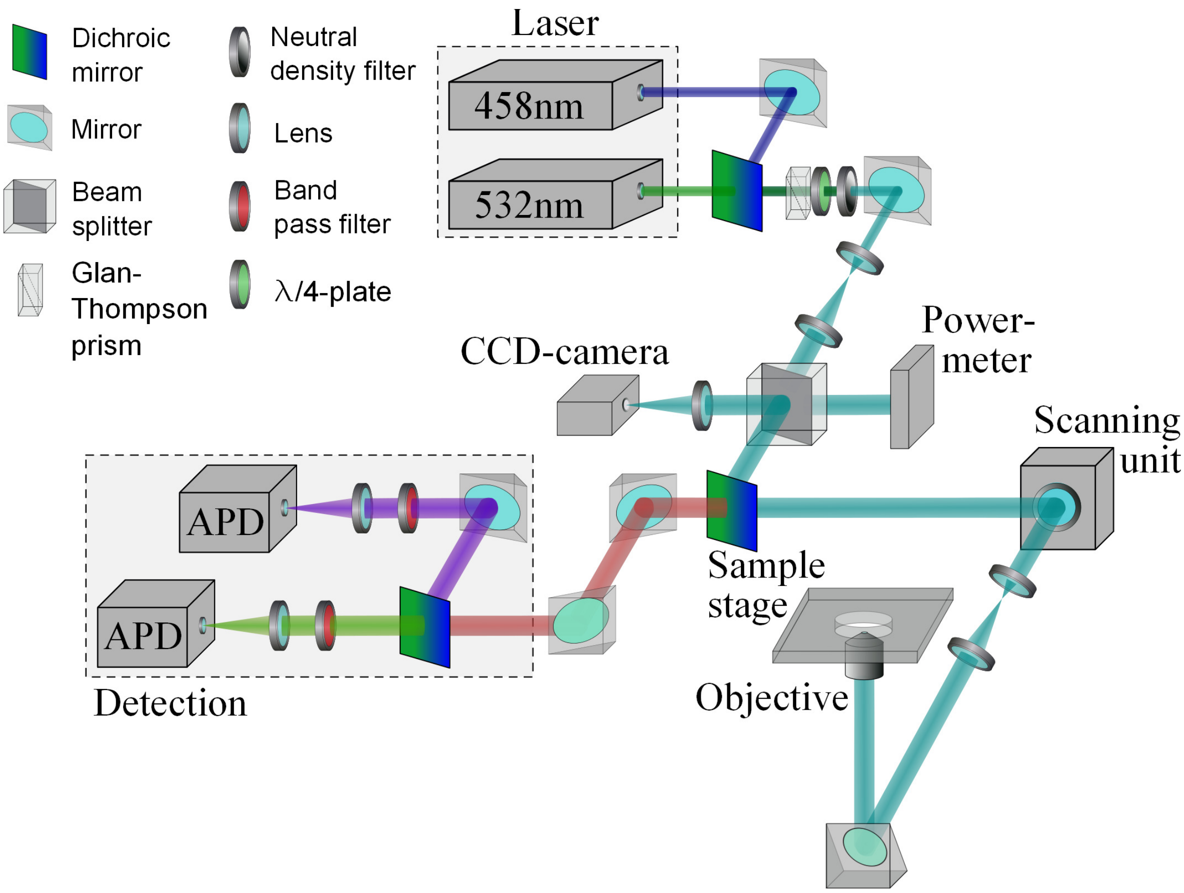

Figure 3.2: Schematic setup of the 2-color mode the home-built laser scanning confocal microscope (LSCM). The previous setup was extended by a second illumination and detection line (gray-shaded boxes)

coloring the sample components, different fluorescent dyes were used. For the 1-color mode LSCM the dyes Rhodamine B and Nile Red were used, which were excitable with the green laser at a wavelength of 532nm. Their fluorescence spectra were typically lying above 560nm. To label further sample components, dyes were needed, which had a negligible overlap in the fluorescence spectra with the already used dyes. Suitable were Coumarin derivates, which were excitable with a wavelength of 458nm. With the combination of different razor edge filters the available wavelength spectra for the two detectors could be tuned precisely. The bottom detector lying in transmission direction of the dichroic mirror was used for the detection of the green fluorescent light, i.e. fluorescence of sample components labeled with Rhodamine B or Nile Red. A razor edge long pass filter (et555lp, Chroma Technology Corp., Rockingham, USA) in front of this detector blocked all wavelengths below 555nm to separate this fluorescence (Fig.3.3). For detecting the fluorescence of the Coumarine derivates, the second detector was used.

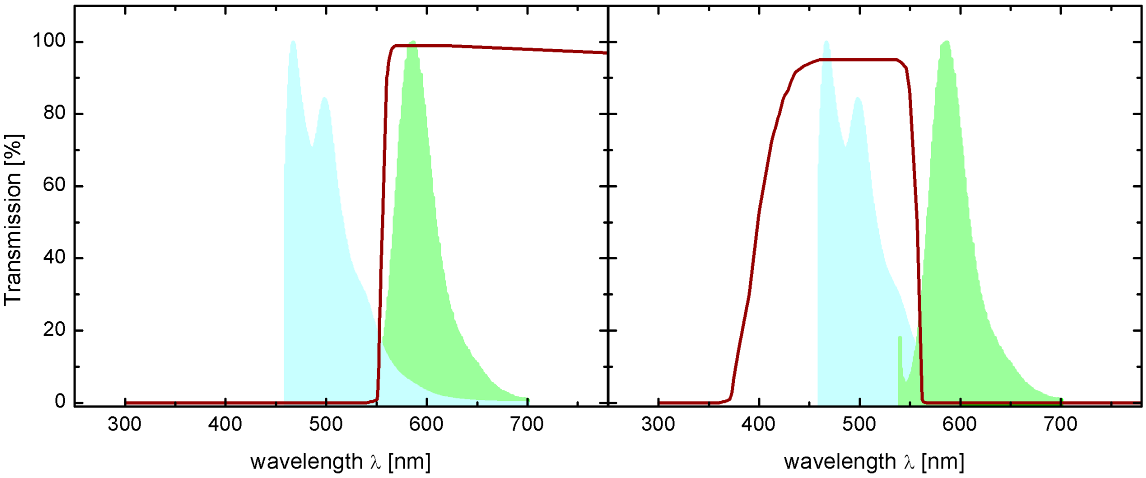

Figure 3.3: Detection spectra at the different detectors in the 2-color mode LSCM. The fluorescence spectra of Coumarin 6 in arbitrary units is indicated in blue, the fluorescence of Rhodamine B in green. The detection spectra at the bottom detector is only sensitive on wavelength above 560nm due to the razor edge filters (left). At the top detector above 560nm most parts of the green fluorescence are blocked away (right)

This top detector was lying in reflection direction of the dichroic mirror. For avoiding an overlap with the green fluorescence, a razor edge short pass filter (hq550sp, Chroma Technology Corp., Rockingham, USA) in the beam path blocked all wavelengths above 550nm. As the sample was illuminated simultaneously with both lasers, an additional single notch filter (F40-532, AHF Analysentechik AG, Germany) could be inserted in the beam path for blocking the green illumination laser.

On both detectors also the reflection of non-fluorescent and non-index matched objects, e.g. a diamond nano-indenter tip (see Sec.3.2), could be detected (Fig.3.4). As their reflections were at wavelengths of the illuminating lasers, the filters had to be removed for detecting these objects.

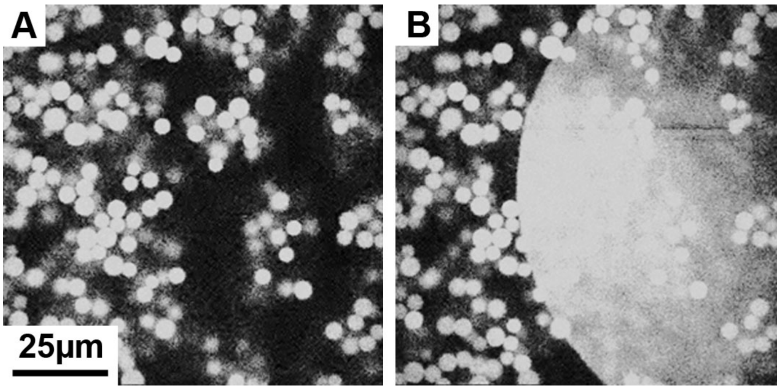

Figure 3.4: LSCM image of a reflective non-fluorescent object in fluorescence mode (A) and in reflection mode (B). The razor edge filters blocked the reflected light of the nano-indenter tip in the fluorescence mode

3.2 Nano-manipulator

Measurements under mechanical load were performed with a home-built nano-manipulator (Fig.3.5). It was a combination of a translation stage and a mounted diamond indenter tip (Synton-MDP AG, Switzerland) for applying a mechanical load. The indenter tip had a flat circular surface with different available surface diameters: 20μm, 200μm and 650μm (Fig.3.6). The sample was placed as a suspension droplet onto a thin cover slide (thickness 170μm, Menzel, Germany). In combination with this cover slide the indenter tip surface acted as a load cell in plate-plate geometry (Fig.3.7A). Since the suspension droplet was much larger in diameter than the indenter tip surface, only a small volume of the sample was actually probed (Fig.3.7B). As solvents with low vapor pressures and large suspension droplet volumes were used, solvent evaporation did not effect the measurements.

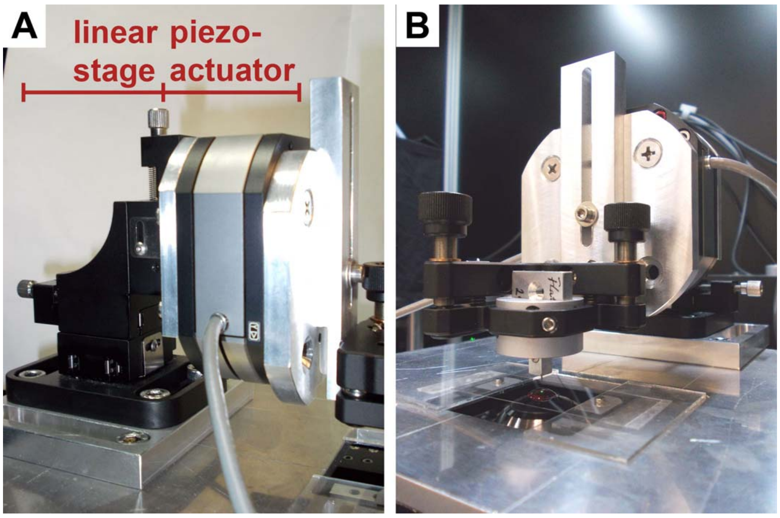

Figure 3.5: Nano-manipulator setup consisting of a translation stage and a diamond indenter tip. The translation stage was composed of a 3-axis linear stage and a a piezo-actuator (A). The diamond indenter tip could be aligned with a mirror holder (B)

The translation stage contained a 3-axis linear stage (Linos, Germany) and a biaxial piezo-actuator (PXY 200 SG, piezosystem jena GmbH, Germany) for driving the indenter tip. The 3-axis linear stage was used for positioning of the indenter tip in the observation volume. First the tip was positioned coarsely in respect to the laser focus of the LSCM. The maximum achievable displacement of the 3-axis linear stage is 5mm with

Figure 3.6: Overview of the diamond nano-indenter tips. Tip with circular surface with 20μm diameter (A) and 200μm (B)

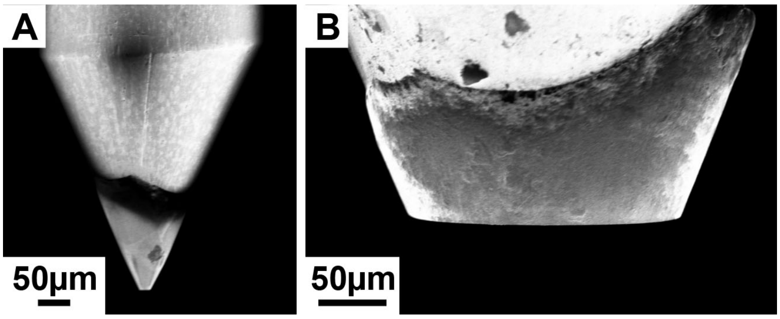

an accuracy of roughly 5μm. A fine positioning was done with the piezo-actuator while scanning in 2D and observing the reflection of the indenter tip surface. The parallelism of the indenter tip in respect to the cover slide was adjusted with a biaxial mirror holder, where the tip was centered.
The biaxial piezo-actuator enabled applying the mechanical load in two different directions. Therewith a linear shear could be accomplished while moving the indenter along the x-axis or a compression when moving along the z-axis. The maximum achievable displacement of the piezo-actuator and hence the tip was 160μm in both directions with a maximum driving velocity of 3.75mm/s. The positioning of the indenter tip with the piezo-actuator was able with an accurancy of 3nm. Via changing the plate-plate distance, the sample thickness could be adjusted freely. Usually the plate-plate distance was in the range from 10μm to 160μm. During the 3D imaging of the sample the plate distance was always kept constant, as strain-controlled experiments were performed.

Figure 3.7: Schematic view of the plate-plate geometry (not to scale) (A). Suspension droplet sitting on the cover slide. The indenter tip is located above the droplet (B)

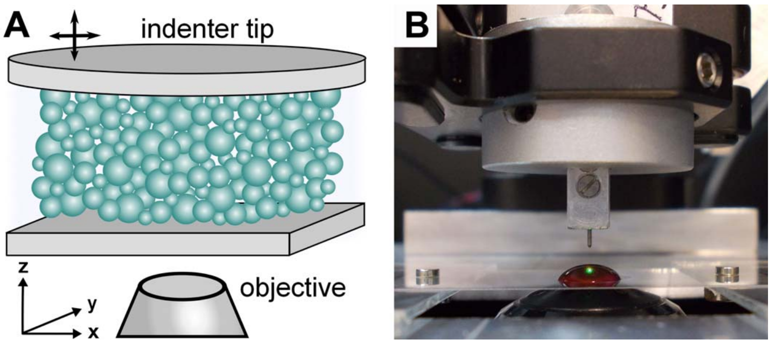

4 Model Systems

4.1 Particles

All studied samples consisted of polydisperse and nano-porous silica spheres (Kromasil 100 Sil 7µm, Batch AT0295, Akzo Nobel, Sweden, purchased from MZ-Analysentechnik GmbH, Germany) (Fig.4.1A). As they were originally used for chromatography, they were well defined concerning their bulk and surface properties (see Sec.10.1). The particles exhibited a large specific surface area of $306\mathrm{m}^2/\mathrm{g}$ with pore volumes of 0.83ml/g and pore sizes of 10nm in diameter (Fig.4.1B). The diameters ranged from 5µm up to 10µm with a mean diameter of 7.39µm and a standard deviation of 0.69µm (see Sec.4.1.2).

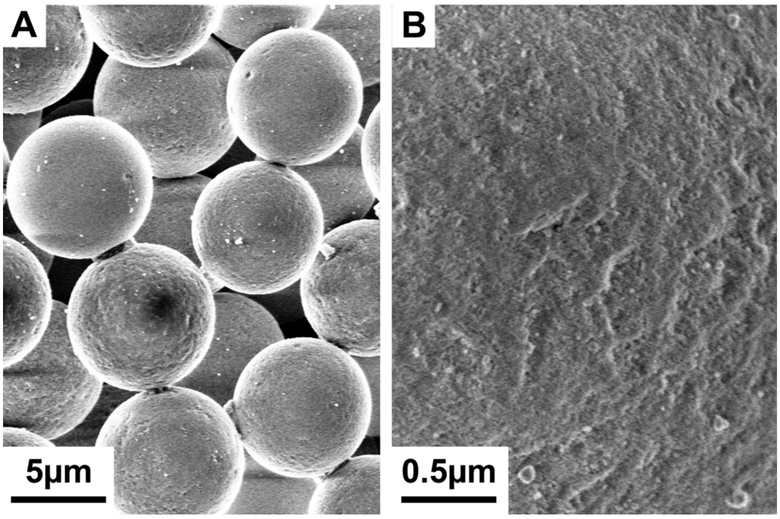

Figure 4.1: Scanning electron microscope images from the silica particles as purchased (A). The particle surface had a nm-scaled roughness (B)

4.1.1 Synthesis for Particle Coloring

For imaging the particles with confocal microscopy, they were fluorescently labeled via Stöber synthesis [73, 74]. Rhodamine B isothiocyanate (mixed isomer, Sigma-Aldrich Chemie GmbH, Germany) as fluorescent dye for the synthesis was used. The dye could be excited with a wavelength of 532nm and had a quantum yield of roughly 40% [75]. For the experiments diffusion and translation of the dye molecules in the silica matrix were undesirable. To avoid the diffusion, the dye molecules were covalently bound to a silane molecule (APS, (3-aminopropyl)triethoxysilane, Sigma-Aldrich Chemie GmbH, Germany) (Fig.4.2), which is later incorporated during the synthesis permanently into the silica matrix.

Preparation of Rhodamine B-APS solution

The Rhodamine B-APS solution for the fluorescence labeling was synthesized and provided by Gabriele Schäfer. 0.1178g Rhodamine B isothiocyanate and 0.0938g APS were dissolved in 10ml ethanol and stirred darkened for more than 12 hours at room temperature. In the reaction the free electron pair of the amin group (NH_2) in the APS attacks the electrophilic carbon of the isothiocyanate complex. The double bond breaks and the amin binds with the nitrogen to the carbon with one hydrogen being bound to the nitrogen of the isothiocyanate.

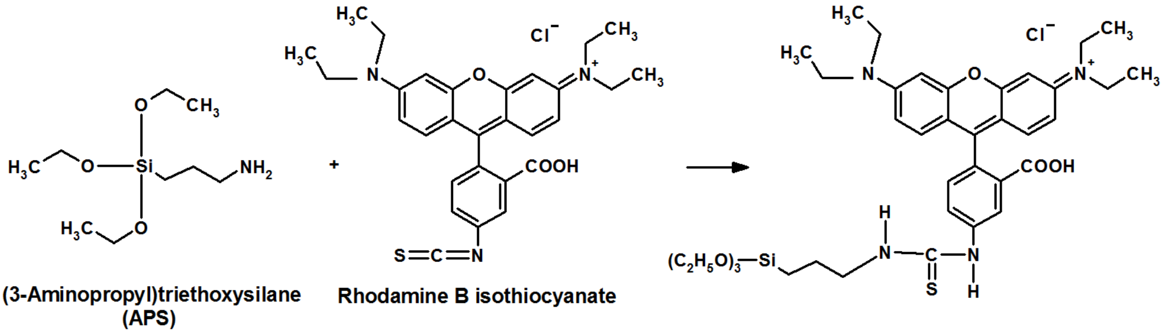

Figure 4.2: The Rhodamine B isothiocyanate molecule was covalently bound to a silane molecule (APS). This Rhodamine B-APS compound was later used for the fluorescence labeling of the silica particles

Fluorescence labeling

For the Stöber synthesis the silica particles were dispersed in ethanol (PA grade, Sigma-Aldrich Chemie GmbH, Germany). An 28w% ammonia solution was added to generate a basic environment. The Rhodamine B-APS solution and tetraethoxysilane (TES, Sigma-Aldrich Chemie GmbH, Germany) were added. The solution was stirred for 12 hours at room temperature. During the synthesis the ammonium hydroxide in the water solution acted as a catalyst, while producing free OH-groups. The free electron pair of the OH-group attacked the electrophilic silicon in the TES molecule. The side arm of the TES was dissociated and reacted with water, generating ethanol and new free OH-groups. The leaving TES group could then be further dissociated. Two dissociated TES molecules condensated with splitting of an ethanol molecule. During this polycondensation process the silica matrix was growing. As the APS-Rhodamine B complex was chemically a functionalized TES molecule, it polycondensated similarly as the TES and was incorporated into the silica matrix.
To remove unreacted dye molecules, the particles were washed several times with ethanol until the natant solvent was clear. During the synthesis one made use of the fact that the silica particles were porous on the nm-scale. The TES molecules acted as initiators for the growth of silica inside the pores of the particles. After the reaction the bulk

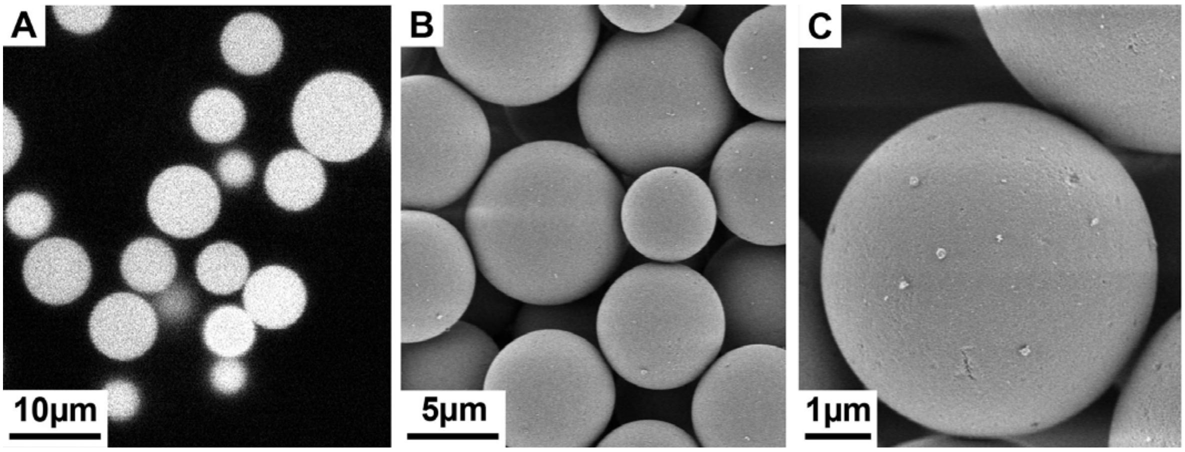

Figure 4.3: Confocal microscopy image of fluorescently labeled particles (A). Scanning electron microscope image from particles after the synthesis: Overview (B) and close-up view (C)

of the particles was fluorescently labeled (Fig.4.3A). Particle diameters and polydispersity were only slightly changed during the synthesis. Also a smoothening of the surface (Fig.4.3C) was observed. The actual size distribution was determined from SEM (1530 Gemini LEO, Zeiss, Jena, Germany) images and compared with the particle diameters before the synthesis (see Sec.4.1.2).
A thin non-fluorescent shell of roughly 100nm was afterwards synthesized with Stöber synthesis onto the labeled particles. This guaranteed that the dye molecules were protected and unable to react with following surface modifications. Additionally the particle-particle interaction was unaffected as due to the shell it was purely an interaction between silica surfaces. The particles were washed several times with ethanol and clean water (MilliQ) to remove remaining ammonia in the solution.

4.1.2 Physical Properties

Optical properties

For measuring particle refractive indices, the continuous medium should be matched onto the refractive index of the particles. As the core-shell particles were hydrophilic after the Stöber synthesis, an aqueous solution was needed. For this purpose a high concentrated salt solution with the salt sodium thiocyanate (NaSCN, AppliChem GmbH, Darmstadt, Germany) was used. When dissolved in water, the salt shifts the refractive index of the aqueous solution to higher values compared to the pure water refractive index.
The NaSCN was dissolved in clean water (MilliQ) until saturation was reached. Afterwards the particles were dispersed in this aqueous salt solution. The dispersion was then diluted down with clean water until it turned transparent. At this point the NaSCN-solution had the same refractive index as the particles, as then no scattering at the solution-particle interface occurred. The core-shell particles had after the Stöber syn-

thesis a refractive index of 1.443±0.003.

The NaSCN-solution was used in the following also as continuous medium for several model systems (see Sec.4.2 and Sec.4.2.2). The concentration of the NaSCN in water varied slightly, to achieve different refractive indices for these model systems. For obtaining an refractive index of $n = 1.445$ of the NaSCN-solution, roughly 1g of NaSCN had to be dissolved in 1.15ml water. This corresponded to a particle number density of roughly $6 \cdot 10^{27}\mathrm{m}^{-3}$.

Particle size and size distribution

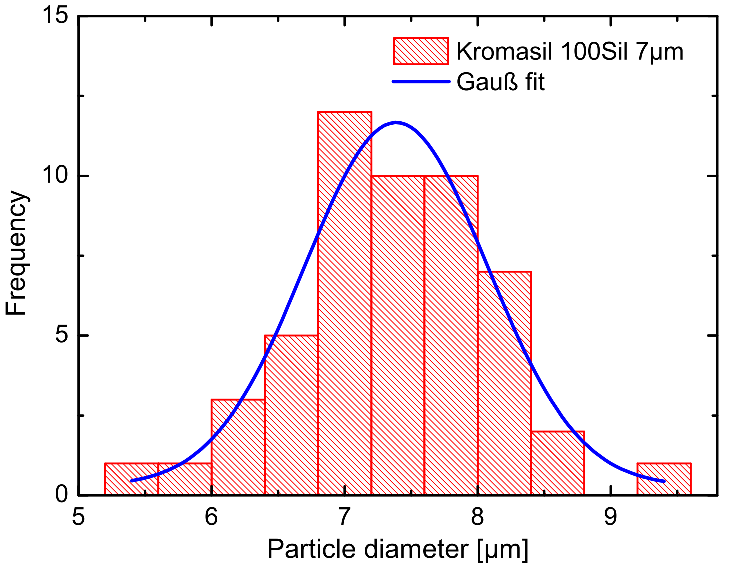

Figure 4.4: Size distribution of the silica particles as purchased. The particle sizes were determined optically from SEM images and had a Gaussian-like distribution

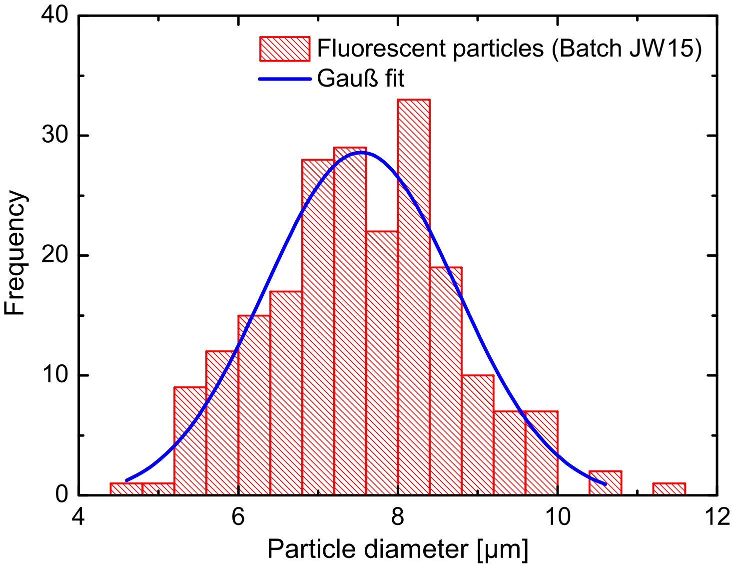

Figure 4.5: Size distribution of the silica particles after the fluorescence labeling. The particle sizes were determined optically from SEM images. The Gaussian-like distribution was broaden during the Stöber synthesis

The particle diameters were determined from SEM images by measuring optically the particle extension. The SEM images were provided by Lena Mammen and Dirk Schneider. 52 particles as purchased (Kromasil 100 Sil 7µm) were explored. The particle diameters were measured with an accuracy of 5% and had a gaussian-like distribution (Fig.4.4). The particles had a mean diameter of 7.39µm and a standard deviation of 0.69µm. After the fluorescence labeling the particle diameter distribution was broaden but still gaussian-like (Fig.4.5). Here 213 particles were examined with an accurancy of 7%. The mean particle diameter was increased to 7.54µm±1.20µm, as a thin non-fluorescent shell of roughly 75nm thickness was synthesized onto the fluorescent particles. The measured particles diameters were later compared with the diameters obtained from LSCM images (see Sec.5.1.2).

Coefficient of rolling friction

Determing the rolling friction coefficient μ_r requires to measure the lateral force F_L needed to roll a spherical particle over a surface (Fig.4.6A). This measurement was performed and provided by Regina Fuchs (Institute of Materials Engineering, University of Siegen, Siegen). To measure the forces a nanoindenter device (TriboIndenter, Hysitron, Minneapolis, USA) in friction loop mode was used. The particle was pressed with a flat indenter tip (see Sec.3.2) onto a smooth silicon substrate and was moved laterally over the surface. To avoid torsion or a sliding motion, the particle was guided along the surface in a “railway system”. This railway was a narrow triangular slit and was etched with a focused ion beam (FIB) into the silicon substrate (Fig.4.6B). The particle motion was dependent on the opening angle of this slit. Rolling motion occurs at large opening angles of about 130°.

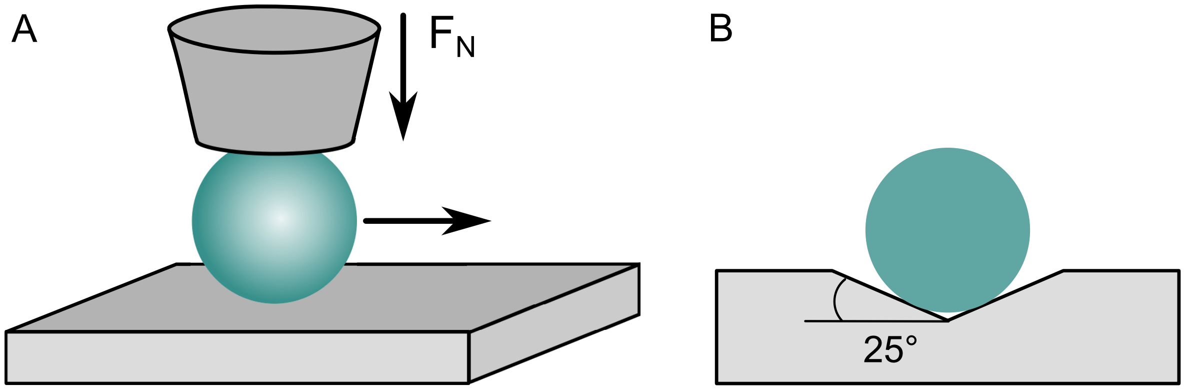

Figure 4.6: For measuring the rolling friction coefficient the particle is pressed onto the surface and moved laterally (A). To avoid torsion or sliding the particle is guided in a railway system (B)

For three different particles of comparable size the lateral force F_L in dependence of the applied normal force F_N was measured (Fig.4.7). The lateral force was averaged over five single measurements. Above a critical normal force of 100µN a rolling motion was observed. At 3000µN a plastic deformation of the particles occurred. For an averaged particle radius of $\overline{R}_p = (3.73 \pm 0.40)\mu$m the coefficient of rolling friction was obtained by a linear fit (see Sec.2.3.3) and was $\overline{\mu}_r = 0.0046$.

Figure 4.7: Rolling friction measurement of silica particles. The lateral force needed to roll the particle over a surface for different normal forces was measured. The rolling friction was obtained by a linear relationship

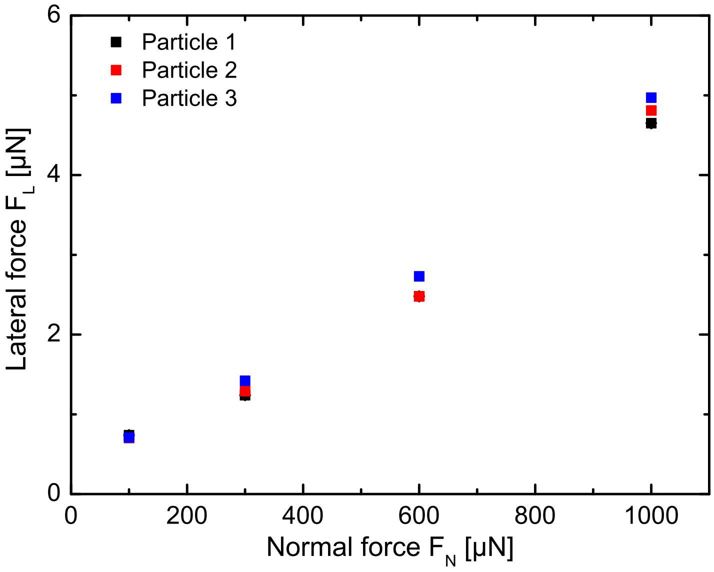

4.2 Sample Systems

Laser scanning techniques like confocal microscopy impose certain requirements on the measured sample. For a high optical resolution along the beam direction (z-axis) it is necessary to avoid scattering at the particle surface. To achieve this, the gaseous environment has to be exchanged by a liquid, having the same refractive index as the particles of interest. To disperse the particles in the surrounding liquid, usually surface modifications are necessary. Different surface modifications and liquids can lead to a wide range of particle-particle interaction. These can range from nearly hard-sphere like (see below) to slightly cohesive (see Sec.4.2.1), or even with an additional binding liquid can act over capillary bridges (see Sec.4.2.2).

Reference system - Model system for dry hard-sphere like powders

As a reference system for the later model system a system with a hard-sphere like particle interaction was used. The system contained the hydrophilic silica particles as obtained from the Stöber synthesis in a NaSCN-solution with refractive index $n = 1.443$. The system is dominated by gravitation, as the Peclet number for silica particles in the NaSCN-solution is $Pe = 1.56 \cdot 10^3$ (see Sec.2.2.5 and Sec.10.4). The volume fraction of the sediment directly after sample preparation was 0.228 ± 0.005 (see Sec.10.2).
Due to the high salt concentration in the NaSCN solution an electrostatic interaction could be neglected. The Debye length in such a system would be $\kappa^{-1} = 22$pm (see Sec.10.4), which is smaller than one atomic diameter. Hence the particle interaction is a

Van der Waals interaction. The minimum separation distance between two silica spheres was then the diameter of a Na^+ ion with its hydration shell and was 560pm [76]. As the NaSCN-solution was matched onto the refractive index of the silica particles, the second term in Eq.2.8 disappeared. The Hamaker constant for silica interacting over a NaSCN-solution with this minimum separation distance was calculated to be $A_H = 2.7 \cdot 10^{22}$J. Hence the interaction energy between two identical silica spheres of radius 3.77µm was $E_{NaSCN} = -36.6\mathrm{k_B T}$ (see Eq.2.7). This small interaction energy shows that they behaved nearly like hard spheres with only a very slight attraction.

When applying a mechanical load, the motion of the indenter plate created a flow near the plate surface. With a maximum displacement of 2µm per load step in the following measurements and a reaction time of 40ms of the driving piezo-actuator, a resulting velocity of the indenter plate of 0.05mm/s was obtained (see Sec.10.4). Due to this small plate velocity the resulting flow was laminar with a Reynolds number of $Re = 4 \cdot 10^{-5}$. As the timescale of the laminar flow $\tau_{lam} = 4.3 \cdot 10^{-5}$s was smaller than the reaction time of the driving piezo-actuator, the flow was instantly following the motion of the indenter plate. After the maximum displacement of 2µm, the laminar flow was then decaying within $4.3 \cdot 10^{-5}$s. As this time was larger than the time needed for dragging a particle along with the flow ($\tau_{drag} = 6.5 \cdot 10^{-6}$s), the granulates felt a drag force. The applied force on the particle with an indenter plate velocity of 0.05mm/s, was 10pN. A free particle, which was not connected to further particles, was dragged with the flow. Particles in contact with others particles were too strongly bound with adhesive forces of 0.3nN for being dragged away.

4.2.1 Model System for Dry Cohesive Powders

Sample preparation

To prepare a model system for a dry powder the particle surface was hydrophobized with long C18-alkyl chains. 50mg of dried particles were dispersed in 1ml of a mixture of 10vol% DMOAP (Dimethyloctadecyl[3-(trimethoxysilyl)propyl] ammonium chloride, Fluka, Sigma-Aldrich Chemie GmbH, Germany) with clean water (MilliQ) (Fig.4.8A). The whole solution was stirred for 2 hours at room temperature. During the reaction the trimethoxy silyl part of the DMOAP attacked the Si-OH groups on the silica surface. Under the deprotonation of the oxygen and a split-off of one methoxy group the silicon bound covalently to the silica surface. The nitrogen only formed an ionic bond with a surface oxygen. Additionally between the silicon atoms of the DMOAP on the surface new oxygen bonds are formed under the release of methanol. After the reaction the particles were washed at least four times with clean ethanol and dried for storage. The DMOAP coating shifted the refractive index of the particles to 1.470 ± 0.003. The particles were finally dispersed in cis-decaline (cis-Decahydronaphtalene, Fluka, Sigma-Aldrich Chemie GmbH, Germany) for index-matching.
In the reaction the DMOAP-molecules bound covalently to the silica surface [77]. The combination of this surface modification and cis-decaline as dispersion medium led to a

slight cohesiveness of the particles [78, 79].

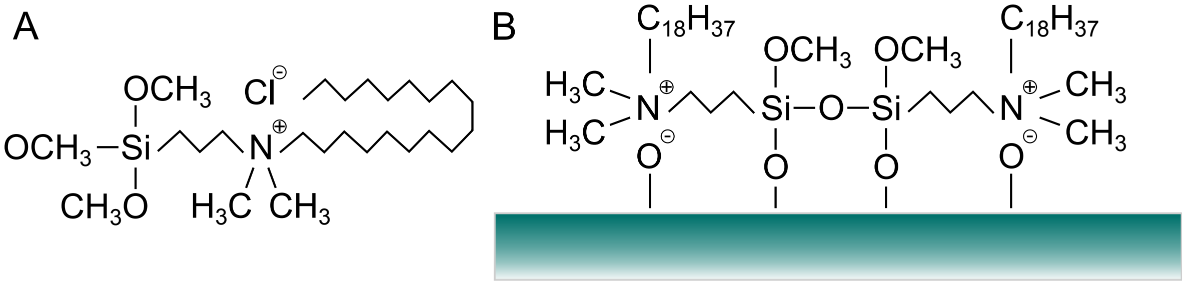

Figure 4.8: The DMOAP-molecule consists of a local charge in the middle part with a silyl and an alkyl chain at the sides (A). On the surface the silyl part forms stable silica bonds while the nitrogen is only bound over an ionic bond (B)

Interactions in dry cohesive model system

The underlying interaction of the particle cohesiveness after the DMOAP modification was a Van der Waals interaction. As the solvent cis-decaline had a very low dielectric constant of $\varepsilon_{deca} = 2.5$ (Tab.10.2), where the local charges of the DMOAP were not able to dissociate (Fig.4.8), an interaction from additional electrostatics could be neglected. In cis-decaline at room temperature the alkyl chains were no longer elongated but collapsed. The interactions of the chains at the surface with solvent molecules and the interactions of the chains between themselves were dominant. This thin layer of alkyl chains, represented by octadecane molecules, reduced the contribution of the silica core to Van der Waals interaction [80]. Hence two octadecane surfaces were interacting with each other over cis-decaline rather than two silica surfaces.

To estimate the thickness of the DMOAP layer on silica in cis-decaline, it was assumed that the alkyl chain behaved like a polymer chain when collapsing. The diameter of the alkyl chain ball was calculated with the radius of gyration (see Sec.10.4). A layer thickness of roughly 400pm of the DMOAP film was obtained. This large film thickness showed that not the silica surfaces are contributing to the Van der Waals interaction but the octadecane molecules at the particle surface. The Hamaker constant of two octadecane surfaces interacting over cis-decaline was calculated to be $A_H = 6.3 \cdot 10^{22}\mathrm{J}$ (Eq.2.8). For the calculation the material constants in Tab.10.2 were used. The minimum separation distance between these two surfaces was depending on the size of one cis-decaline molecule. The largest extension of the molecule was estimated to be 580pm, the smallest 160pm (see Sec.10.4). Depending on the orientation of the cis-decaline molecule the interaction energy obtained with Eq.2.7 ranged from $E_{deca} = -84.1\mathrm{k_B T}$ to $E_{deca} = -304.9\mathrm{k_B T}$. This showed that the particles were cohesive.

As in the reference model system the dry cohesive model system is dominated by gravity with a Peclet number of $Pe = 2.34 \cdot 10^3$. Particles are sedimenting directly after the sample preparation to the bottom cover slide. The volume fraction (see Sec.10.2) of the undisturbed sediment was $\phi_{ave} = 0.332 \pm 0.016$.

The hydrodynamic influence of the indenter plate motion was comparable to the reference system (See Sec.4.2). As the particles in the dry model system were more cohesive than in the hard-sphere like system, also here only free particles were able to be dragged with the flow.

4.2.2 Model System for Wet Powders

In a wet granular system, where air is the continuous medium, a binding liquid has always a finite contact angle with the particle surface. As for confocal microscopy all refractive indices have to be matched, the continuous medium had to be exchanged by a liquid. In this case the wet model system consisted of solid particles in a mixture of two liquids, one continuous liquid and one binding liquid. The aqueous NaSCN-solution was used for matching the refractive index of the silica particles (see Sec.4.1.2). The NaSCN-solution acted as continuous phase, the organic solvent cis-decaline as binder phase. When dispersing the hydrophilic silica particles after the Stöber synthesis in a mixture of NaSCN-solution and cis-decaline, the particles were all gathered in the water phase with a zero contact angle (Fig.4.9A). Particles hydrophobized with DMOAP (see Sec.4.2.1) dispersed in the same mixture of liquids led to the equivalent effect but with the particles gathered in the cis-decaline (Fig.4.9B). In both cases a macroscopic phase separation was observed.

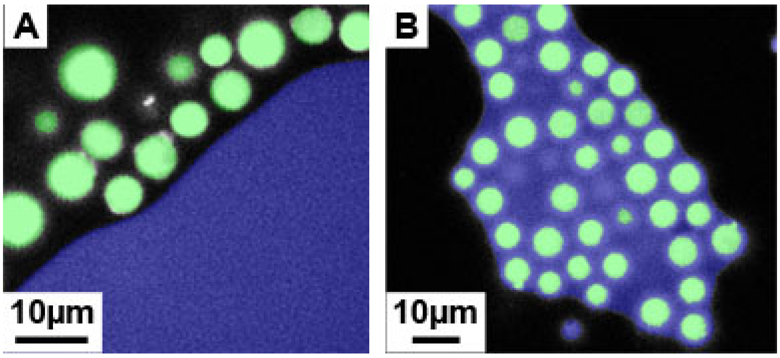

Figure 4.9: Phase separation in the 3-phase system. Hydrophilic particles are separated in the water phase (A), while hydrophobic particles are gathered in the organic solvent (B)

The challenge here was to tune the particle surface in such a way that the liquid-liquid interface had a finite contact angle with the particle surface (see Eq.2.21). The silica surface was covered with free Si-OH groups after the Stöber synthesis, which made the silica particles hydrophilic. With the surface agent Hexamethyl-Disilazane (HMDS, Sigma-Aldrich Chemie GmbH, Germany) it was possible to cover a part of the free Si-OH groups with carbon chains to make the silica surface more polar. The particles were now amphiphilic, so that the liquid-liquid interface could anker onto the surface.

Mechanism of the HMDS reaction

HMDS is a molecule to prepare trimethylsilyl (TMS) derivates via a silylation reaction [81]. In silylation the (trimethyl) silyl derivates are formed by replacing the hydrogen of the OH-group with a TMS group. The silyl derivates are thermally more stable and less polar. In the first reaction step the trimethyl silyl part of the HMDS attacks the Si-OH group, producing a zwitterionic transition state (Fig.4.10).

$$2\text{Si-OH} + (\text{CH}_3)_3\text{-Si-NH-Si-}(\text{CH}_3)_3 \rightarrow 2\text{Si-O-Si-}(\text{CH}_3)_3 + \text{NH}_3$$

In the second reaction step the oxygen is deprotonated. The leaving group (R) is binding at a further Si-OH group, while ammonia is produced.

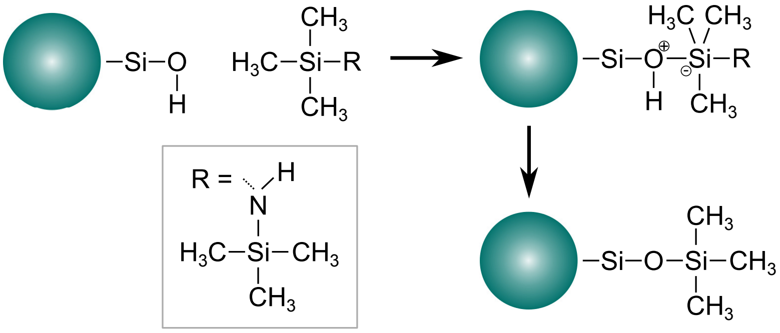

Figure 4.10: Reaction of HMDS with a hydrophilic silica surface. During the reaction parts of the OH-groups are exchanged by trimethylsilyl groups

Surface modification with HMDS

To obtain an amphiphilic particle, the TMS groups should be randomly distributed on the silica surface and cover 50% of the Si-OH groups. The median surface of the used silica particles is roughly $0.5\text{m}^2/\text{mg}$ (based on the supplier). It was assumed that $41.25 \cdot 10^{16}$ OH groups per squaremeter were located on the silica surface [82]. For a sample of 50mg of particles $1.30 \cdot 10^{-7}$mol of OH groups have to be converted by HMDS. For that $6.5 \cdot 10^{-8}$mol of HMDS were dissolved in 1ml tetrahydrofuran (THF, Sigma-Aldrich Chemie GmbH, Germany) and 50mg silica particles were dispersed while the whole solution was stirred for 30 minutes at room temperature. Afterwards the particles were washed several times with THF and clean water to remove the remaining ammonia in the solution. Finally the particles were dried for storage.

Sample preparation

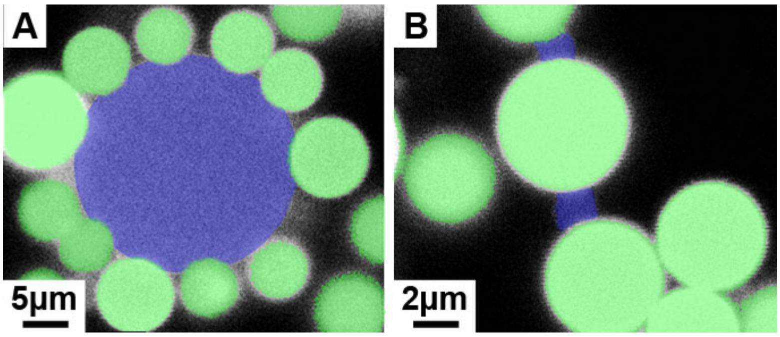

Figure 4.11: Finite contact of the liquid-liquid interface on the silica surface. For decaline droplets a contact angle of 130° (A), for single capillary bridges a contact angle of 90° (B) was obtained

The HMDS-modified particles were first dispersed in the NaSCN-solution. Then a saturated fluorescent cis-decaline solution with Coumarin 6 (Sigma-Aldrich Chemie GmbH, Germany)) as dye was added. The suspension was mixed by hand shaking. A finite contact angle of the liquid-liquid interface was now obtained (Fig.4.11). The obtained sample structure had a Pickering emulsion-like appearance. A system spanning network of the binding liquid was not observed. The observed contact angles for different samples varied from roughly 90° to 130°, depending on the strength of hand shaking.

Different mixing techniques were examined. Ultrasonication led to a phase separation of the two liquids, while mixing with magnetic stirrer the cis-decaline was bound to the teflon-coating of the stirrer. The best mixing technique was hand shaking as here cis-decaline droplets were formed and no phase separation of the liquids occurred. Depending on the energy input during the shaking, different initial cis-decaline droplet sizes were achieved. Slight shaking with a small energy input led to broad size distribution with a high amount of large droplets (Fig.4.12). Strong shaking with a small energy input resulted in many small droplets.

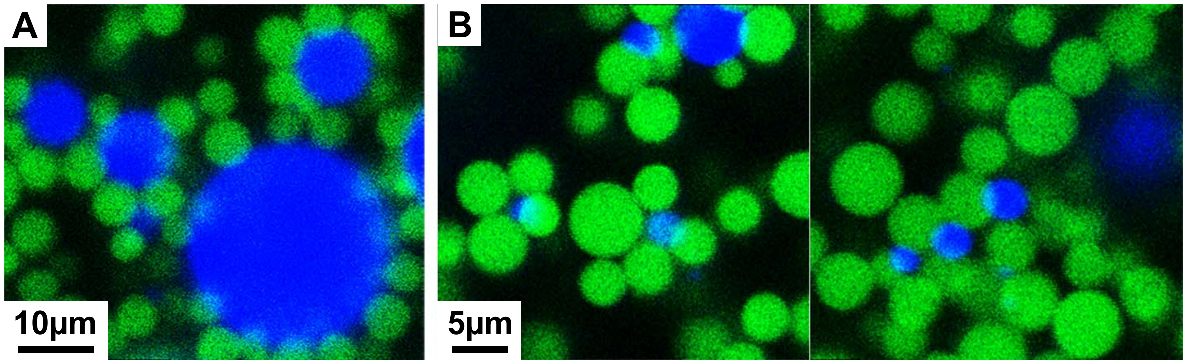

Figure 4.12: The energy input during sample shaking leads to different droplet sizes

Interactions in the wet model system

In the wet model system the interactions of the particles among each other and with the binding liquid have to be discussed separately. The particle-particle interaction was similar to the one in the reference system, as here the silica particles were in a NaSCN-solution. The interaction of the particles with the binding liquid was like in a Pickering emulsion. The binding mechanism was a capillary force and the binding energy of a particle with radius $R_p = 3.77\mu\text{m}$ at the liquid-liquid interface was $E_{bind} = 2.42 \cdot 10^7 \mathrm{k_B T}$ (Eq.2.25). This is explicitly larger than the particle-particle interaction, which can be then neglected if the particle is bound at the liquid-liquid interface. The surface tension of the liquid-liquid interface was measured with a Du Noüy Ring tensiometer and was $\gamma_{ll} = 17 \cdot 10^{-3}\mathrm{N/m}$.

As in the systems described before, the particles in the wet system were dominated by gravitation. The Peclet number was identical to the one of the reference system. The initial sediment volume fraction was $\phi_{ave} = 0.249 \pm 0.006$ (see Sec.10.2). The potential energy from sedimenting one particle radius was roughly $\Delta E_{pot} = 1.5 \cdot 10^3 \mathrm{k_B T}$ and was hence negligible compared to the binding energy of the particle at the liquid-liquid interface.

The hydrodynamic interactions of the particles here were identical to them in the dry cohesive model system and were in general not large enough for moving the particles within the flow (see Sec.4.2). The main hydrodynamic interaction could then arise from the motion of the cis-decaline droplets. A deformation of the droplet leads to an increase of the interface, as the droplet volume is conserved (see Sec.2.2.4). The energy for increasing the surface and deforming the droplet shape is stored inside the droplet and is denoted here as "deformation energy E_{deform}". The deformation of a droplet along one axis could be in the range of the indenter plate displacement per load step. But as the relaxation of the droplet surface occurs on timescales smaller than a millisecond [83], the applied drag force on particles in the surrounding would be more than two orders of magnitude larger than in the reference of the dry cohesive model system. In this case also particles bound to other particles or to the droplets surface could be moved by the laminar flow.

For estimating the deformation energy it was assumed that a spherical droplet was elongated along one axis by ten percent. The shape of the droplet turns then into a prolate ellipsoid. The deformation energy stored in the droplet is hence the energy for increasing the droplet surface. For a droplet in the size range of silica particles ($R_d = 4.00\mu\mathrm{m}$) this energy was $E_{deform} = 3.06 \cdot 10^6 \mathrm{k_B T}$ (see Sec.10.4). Depending on the strength of deformation and droplet size, this deformation energy can easily exceed the binding energy of the particles, causing a release from the liquid-liquid interface.

5 Experimental Techniques

Parts of the data analysis techniques used for polydisperse particles were already published. The sections 5.1.2 and 5.2 are based on the publication “Measurement of rotation of individual spherical particles in cohesive granulates” by Jennifer Wenzl, Ryohei Seto, Marcel Roth, Hans-Jürgen Butt and Günter K. Auernhammer [72].

5.1 Image Processing

5.1.1 Line-line Algorithm

When performing a 3D image, the sample is scanned plane by plane in lines along the x-axis. In a few cases in the measured 2D frame the lines could be shifted by a few pixel against each other (Fig.5.1A). This effect can have two contributions. The one is an inaccurate translation of the pixel-to-µm ratio into a voltage signal for the frequency generator, which drives the scanning unit. The second contribution is an asynchronism of the counting card with this frequency generator. To overcome this problem a new algorithm was developed for image processing. To enhance the particle localization the images were corrected concerning this line shifting.

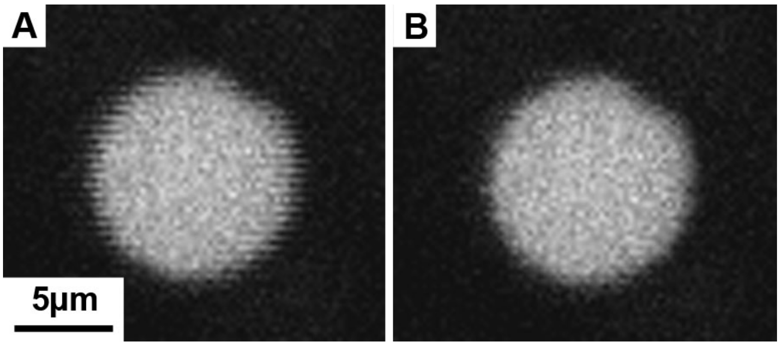

Figure 5.1: LSCM image of a fluorescent particle. Raw image (A) and after image processing with the line-line algorithm (B)

The working principle of this algorithm was a correlation and shifting of adjacent lines until the correlation maximum was reached. This was the case when the lines were shifted back in their original correct position. In detail first for every line the intensity was averaged over all pixels in this line. Afterwards in the original image for every pixel in this line the averaged intensity was subtracted. This was necessary as the correlation worked reliably for intensity signal distributed around a zero point. The intensities of adjacent pixel in two neighboring lines were then correlated, this was done for all pixels in these lines. The lines were shifted pixelwise against each other into positive and negative x-direction and correlated (Fig.5.2). At a certain number of shifted pixel the correlation maximum was reached. The correlated intensity profile was fitted with a polynomial of degree two and the maximum was calculated. The maximum was rounded to the next integer pixel value to obtain the number of shifted pixels for this pair of lines. This procedure was done for all pairs of adjacent lines of the entire image. Every second line was then shifted by the corresponding number of shifted pixels for getting a refined image (Fig.5.1B).

Figure 5.2: Correlated intensity profile of two adjacent lines versus the shifted pixels

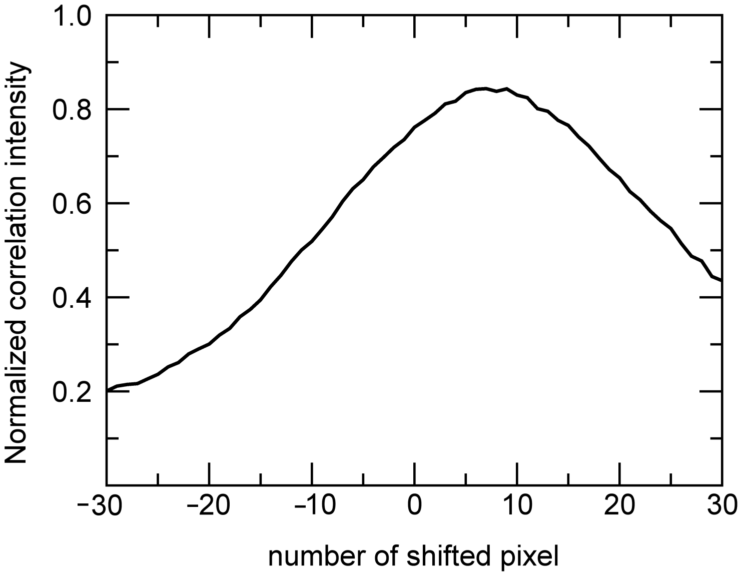

5.1.2 Particle Localization

The first algorithm for identifying and localizing spherical monodisperse particles was introduced 1996 by Crocker and Grier [84]. Weeks further developed this algorithm to a working routine [85]. The algorithm searches in the 3D image for intensity maxima and compares the surrounding intensity distribution with a predetermined characteristic particle intensity distribution. If the intensity profiles are matching, at this point in the 3D image a particle would be identified and localized. As the system used in this work consisted of large polydisperse particles, Marcel Roth developed a modification of the Weeks-routines [72]. In this modification the principal localization worked the same for mono- and polydisperse particles.

For localizing the particles as a first step a mask $M_{i,j,k}$, which mimics the size and intensity distribution of the particles was created (Fig.5.3B). For that, the intensity profile along one axis of a characteristic particle was fitted with a polynomial of degree four. A suitable intensity cutoff led to a Gaussian-like intensity distribution in 1D. With the assumption of a spherically symmetric intensity distribution inside the particle, a 3D mask $M_{i,j,k}$ is calculated mimicking the particle. The 3D image data $I_{i,j,k}$ was then spatially convolved with this mask.

$$C_{i,j,k} = \sum_{lmn=1}^{N} I_{i-l,j-m,k-n}\, M_{l,m,n} \tag{5.1}$$

As a result of the convolution the particles appeared in the convolved 3D image $C_{i,j,k}$ as sharp, smooth and isolated intensity maxima in the case of monodisperse particles (Fig.5.3C).

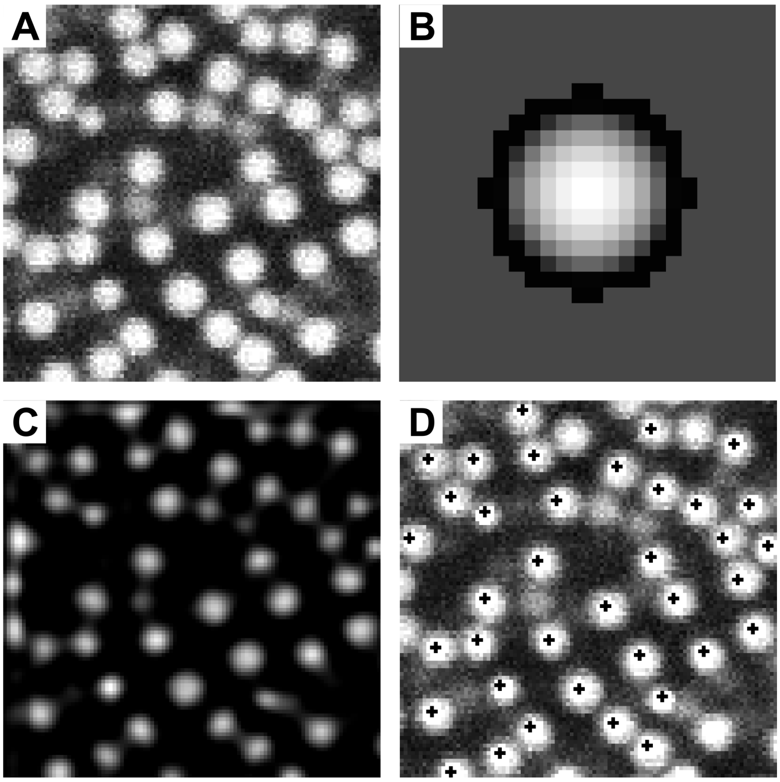

Figure 5.3: Confocal image during the localization process for monodisperse particles. Image as measured with LSCM (A), the mask $M_{i,j,k}$ (B), after the convolution with the mask (C) and with the localized particle positions marked with white circles and black crosses (D)

Dealing with polydisperse particles, a single mask could not match the size of all particles. Only particles in a certain size range appeared as isolated maxima in $C_{i,j,k}$. If the mask was to small compared to the real particle size, the particles appeared with a toroidal intensity distribution (Fig.5.4B). Particles convolved with a larger mask got blurred (Fig.5.4D). To overcome this problem the 3D image $I_{i,j,k}$ was convolved separately with two or more masks $M^{(\alpha)}_{i,j,k}$ of different sizes. The chosen sizes of $M^{(\alpha)}_{i,j,k}$ depended on the degree of the particles polydispersity and should cover the whole diameter range. Afterwards the individual convolved 3D images $C^{(\alpha)}_{i,j,k}$ were merged together by choosing the highest intensity for each individual pixel (Fig.5.4E).

$$C_{i,j,k} = \max_\alpha \left(C^{(\alpha)}_{i,j,k} \right) \tag{5.2}$$

From the resulting merged convolved 3D images $C_{i,j,k}$ the particle positions were found with the original algorithm (Fig.5.4F). For the 3D images 3 or 4 masks were sufficient

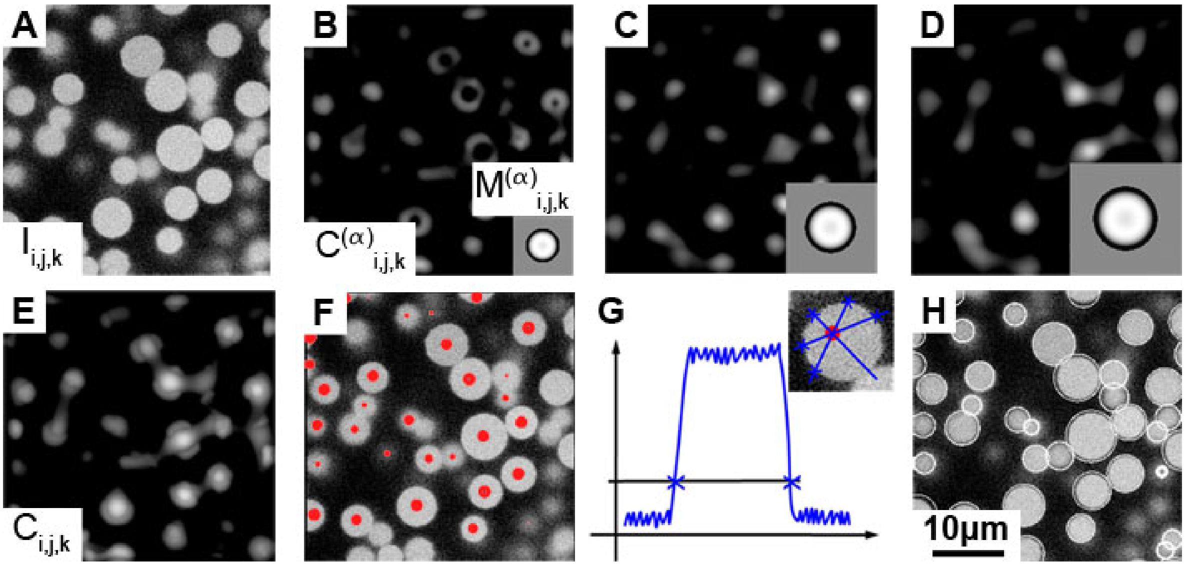

Figure 5.4: Confocal images at different image processing and localization steps for polydisperse particles. Image, as measured with LSCM (A), after the convolution with an undersized (B), an optimal sized (C) and oversized (D) mask $M_{i,j,k}$, merged data after convolution with different mask sizes (E), LSCM image with obtained particle positions marked with red dots (F). Intensity profile of a localized particle with obtained points at the rim (G), particles with obtained diameter after refinement step (H)

to localize all particles. The localization efficiency usually is higher than 95%. However, the quality of the positioning had a bigger error bar compared to the positioning of monodisperse particles. This was due to artifacts caused by the multiple convolutions. Therefore, the preliminary particle coordinates could only serve as starting points for an additional refinement step. For this refinement step it was essential to have a high contrast between the particles and the background in the original 3D image $I_{i,j,k}$. For each identified particle, intensity profiles through the preliminary particle position were determined (Fig.5.4G). These profiles showed a plateau in the interior and dropped down at the rim of the particle. With a suitable intensity threshold a set of 3D points (x_a, y_a, z_a) was extracted, which lied on the spherical particle surface. The exact center position (x_o, y_o, z_o) and diameter of the particle were obtained by fitting a sphere through the data points (x_a, y_a, z_a) (Fig.5.4H). This was done by minimizing the following expression:

$$\begin{aligned}\mathcal{F}(x_o, y_o, z_o, R_p) = \sum_a \big[&(x_a - x_o)^2 + (y_a - y_o)^2 \\ &+ (z_a - z_o)^2 - R_p^2 \big]\end{aligned} \tag{5.3}$$

Particles were localized with a positioning accurancy of 135nm in x- and y-direction and 248nm in z-direction. Diameters had an accurancy of 41nm (see Sec.10.3). Once the exact particle positions and diameters were determined, all structural properties of the sample, such as the volume fraction, Voronoi cells, etc. were obtained as described below.

The choice of the threshold for extracting (x_a, y_a, z_a) strongly affects the particle diameter obtained from LSCM images. For a compression measurement (see Sec.6.2.1) 5065 particles were examined (Fig.5.5). The obtained averaged particle diameter was 6.98µm±0.88µm and was roughly 8% smaller than the diameters from SEM images (Fig.4.5).

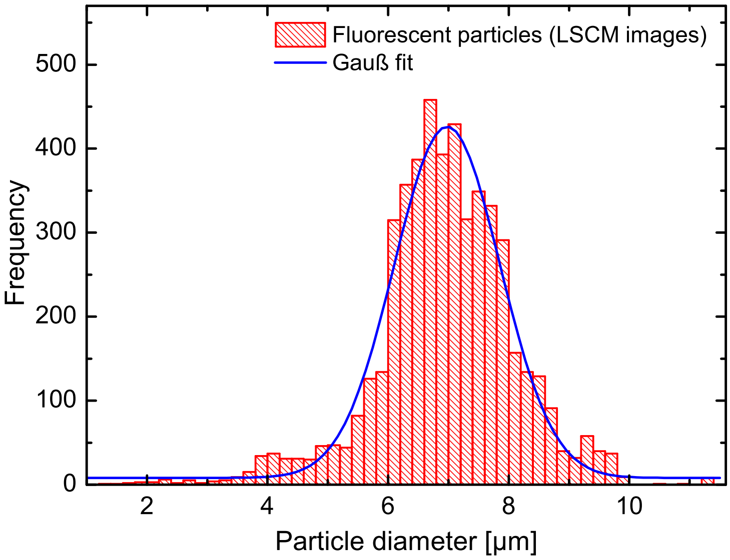

Figure 5.5: Size distribution of the silica particles obtained from LSCM images. The averaged particle diameter is smaller than obtained from SEM images

5.2 Structure Analysis

5.2.1 Voronoi Tesselation

The volume fraction, i.e. the ratio between the sum of all particle volumes and the volume of the entire system, is one of the key parameters to describe the structure of granular systems quantitatively. In many systems the particle distribution is not homogeneous, leading to local variations in the volume available for each particle. The distribution of local volume fractions can be used to characterize structural heterogeneities of granular systems. One way to determine the volume available for each particle and hence the local volume fraction was performing a Voronoi tessellation [86]. For monodisperse particles any spatial point $\vec{x}$ was associated to the nearest particle i, if $|\vec{x} - \vec{x}_i| < |\vec{x} - \vec{x}_j|$ was satisfied for all $j \neq i$. Here $\vec{x}_i$ was the central position of the particle i. All points in the system were then uniquely associated with a certain particle.

For polydisperse systems, the tessellation should be performed by considering the particle sizes. Otherwise, the borders of the cells might cross particles (Fig.5.6A). A straightforward extension for polydisperse systems was considering the nearest surface of the particles rather than the central position [87]. A point $\vec{x}$ was then associated to the particle i having the nearest surface point, if $|\vec{x} - \vec{x}_i| - R_i < |\vec{x} - \vec{x}_j| - R_j$ was satisfied

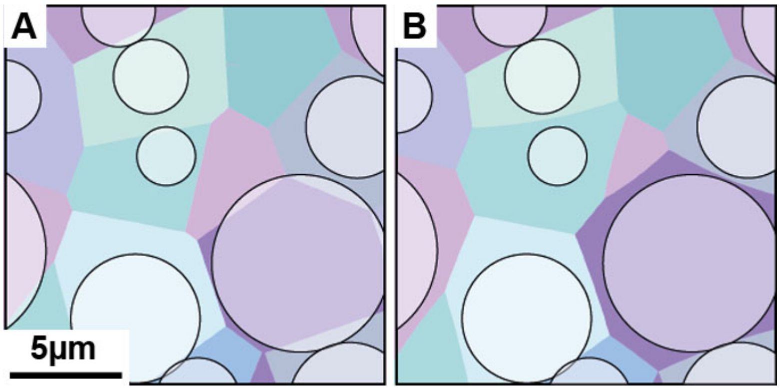

Figure 5.6: 2D plane of the 3D distribution of Voronoi cells for a polydisperse system. Standard Voronoi tessellation in terms of the central positions (A) and Voronoi tessellation by considering the distances to the surfaces (B)

for all $j \neq i$. The distances from the flat sample boundaries, i.e. the indenter and the glass substrate, were also considered. The boundaries of the Voronoi cells were no longer plane, but curved surfaces (Fig.5.6B). To perform the Voronoi tessellation every particle and every point of the observation volume was taken into account. However only particles with all adjacent neighbors in the imaged volume were included for calculating the local volume fractions. Hence, only particles distant laterally more than one diameter from the observation volume boundaries were taken.

5.2.2 Local and Averaged Volume Fraction

By using the Voronoi cell volume $V_{Vor,i}$, the local volume fraction could be defined for each particle i: $\phi_{local,i} \equiv (4/3\pi {R_p}^3)/V_{Vor,i}$. As the particle motion was dominated by gravitation, an inhomogeneous particle distribution along the z-axis was expected. To visualize these inhomogeneities a local volume fraction distribution $\phi_{local}(z)$ along the z-axis was calculated. For that the observation volume was divided into z-layers and the local volume fractions $\phi_{local,i}$ lying in these layers were averaged. In the following the local volume fraction distribution $\phi_{local}(z)$ was plotted versus the averaged z-position of the layer as shown in Fig.5.7.
For an averaged volume fraction ϕ_{ave}, i.e. the ratio between the sum of all particle volumes and the volume of the entire system, all local volume fractions $\phi_{local,i}$ were averaged.

$$\phi_{ave} = \frac{1}{N} \sum_i \phi_{local,i} \tag{5.4}$$

with the uncertainty

$$\Delta\phi_{ave} = \frac{1}{N} \sum_i \Delta\phi_{local,i} \tag{5.5}$$

The uncertainty of the local volume fraction was composed of three components: the particle volume (i.e. the particle radius), the pixelation of the Voronoi cell and the dependence of the Voronoi cell on the particle radius. Only the first two terms were calculated analytically. The third term was dependent on the uncertainties of the first two contributions and was estimated to be of the same order of magnitude as the sum

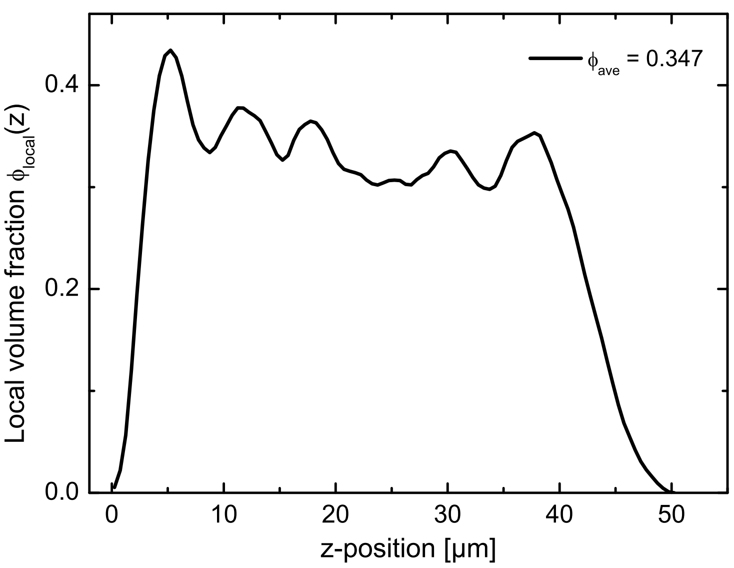

Figure 5.7: Local volume fraction distribution versus the z-position of a sedimented bed of dry cohesive silica particles

of them. The uncertainty of the local volume fraction of one particle was calculated to be

$$\Delta\phi_{local} = \pm 2\sqrt{\left(\frac{3\Delta R_p}{R_p}\cdot\phi_{local,i}\right)^2 + \left(\frac{\Delta V_{Vor}}{V_{Vor}}\cdot\phi_{local}\right)^2} \tag{5.6}$$

with an error of the particle radius of $\Delta R_p = 0.5\mu\text{m}$ and a pixelation of the Voronoi cell of $\Delta V_{Vor} = 10^{-3}\mu\text{m}^3$.

5.3 Particle Motion Analysis

5.3.1 Tracking

For determing the particle trajectories, the tracking algorithm developed by Weeks [85] was used. With this, the particle positions were followed over a series of 3D images. This only works reliably if the particles moved less than their own particle diameter between two consecutive 3D images. Otherwise the particle would be lost and tracked as a new particle. In systems with large structural reorganizations, i.e. large particle displacements only a small fraction of particles could be tracked. The tracking efficiency could than differ drastically from the localization efficiency, which was usually higher than 95% (see Sec.5.1.2).

There are three important parameters, which can be tuned for the particle tracking: the maximum detectable particle displacement, the minimum trajectory length and a memory parameter. The maximum particle displacement should be smaller than one particle diameter. It also should not be too small as then particles with large displacements would not be recognized. A good value here was 80% of the averaged particle diameter. The minimum trajectory length describes the minimum number of 3D images over which a particle trajectory was obtained. Hence only particle were tracked, when they were found at least in this number of consecutive 3D images. For samples with large structural reorganizations with large particle displacements it was difficult to follow the particle trajectory over a high number of 3D images. For describing the characteristic dynamics in the system, a certain number of tracked particles was needed. In this case when the minimal trajectory length was set to be too long, only a few particles were tracked. The number of tracked particles was then too low for appropriate particle statistics. When the minimum trajectory length was to small, no conclusion about the particle displacement and motion could be drawn. In general for reliable particle trajectories the minimum trajectory length should be roughly between 30% and 60% of the total number of measured 3D images.

The memory parameter gives the number of 3D images, in which a particle can disappear without being lost for the trajectory. This parameter should be set to zero, for having the entire trajectory, which is relatable to only one particle.

5.3.2 Particle Displacement

The total displacement of the particles was calculated as the end-to-end distance of the trajectory in x-, y- and z-direction. This total displacement was hence the distance between the particle position in the first and last 3D image for each tracked particle. As the trajectories were not of equal length for all particles (see Sec.5.3.1), they had to be normalized for a better comparison. The displacements were divided by the trajectory length, i.e. the number of 3D images of the trajectory. This gave for every single particle an averaged displacement per load step, with load being compression or shear.

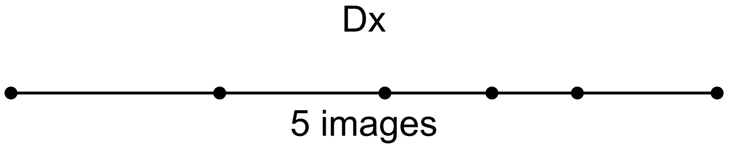

Figure 5.8: Calculation of a particle displacement in x-and y-direction from the particle trajectory. The trajectory is normalized with its length to obtain an averaged displacement per load step

6 Rotation of single spherical Particles

The relation between single particle motion and macroscopic behavior is of a fundamental interest in the scientific field of granular systems. The motion of granular particles, as of any rigid body, is characterized by six degrees of freedom, three for the rotational and three for the translational motion. The ability to measure all six degrees of freedom opens the way for a closer understanding of single particle dynamics in granular systems. Here simulation is an effective approach studying the rotation in granular systems. Simulation models require local force-displacement relationships for all distinct relative displacements. Hence the motion, microstructures and surface properties of all particles have to be considered for describing the macroscopic behavior of granular systems. As the rolling mode plays an important role in cohesive systems, a number of contact models considering the rolling mode have been applied [9, 88–92]. Experimentally the focus was on 2D systems [11] or limited on few particles [93,95]. To capture the full motion of spherical particles, Heim et al. used nano-manipulators with simultaneous scanning electron microscopy [94]. Hasan et al. investigated the translation and rotation of a small number of polydisperse and non-spherical grains in a quasi-static shear [96]. Colloidal science provides a couple of techniques for studying single particle behavior, which can be applied for granular matter. Single particle localization [84] and the introduction of optical anisotropies to spherical particles are two of them. Anthony et al. [97] used fluorescent Janus particles to follow the rotation of single particles with two rotational degrees of freedom. A metal coating on one half of the sphere modulated fluorescent light, while the particle rotated. However the system showed a complex interaction behavior due to the different surface properties of the hemispheres. Lettinga et al. introduced photobleaching [98] as a method to label spheres anisotropically. This idea was taken up for following the rotation of single particles [99]. Here fluorescent dyes incorporated in the particles absorb light only along their dipole orientation. With polarized laser light dye molecules of a certain orientation were bleached, giving the particles a predominant polarized direction. However this method can only resolve the rotation relative to the axis given by the polarization of the bleaching laser.

In this chapter, a new photobleaching technique was developed, which now allows to measure in three dimensions the full motion of spherical particles, i.e., translation and rotation. With compression of a granular bed, the influence of the applied load on the sediment structure and the single particle motion, especially the rotation was investigated. The focus in this work was on the first steps of a compression. The sections 6.1 and 6.2 are based on the publication “Measurement of rotation of individual spherical particles in cohesive granulates” by Jennifer Wenzl, Ryohei Seto, Marcel Roth, Hans-Jürgen Butt and Günter K. Auernhammer [72].

6.1 How to Detect Rotation

Following the rotation of spherical particles requires an optical anisotropy of these particles. This could be achieved by selectively photobleaching a small fraction of the fluorescent dye inside the particles. The photobleaching process required high laser powers and was directly performed in the LSCM. The laser power for bleaching was increased to values higher than 100µW. For the later measurements the laser power was reduced again below 1.5µW to avoid a further bleaching of the fluorescent dyes. As the dye molecules were covalently bound to silane molecules during synthesis (see Sec.4.1.1), they were unable to diffuse inside the silica matrix. This guaranteed that bleached and unbleached molecules did not mix during the measurements and avoided a blurring of the bleached area. A further advantage was that the fluorescent dyes were only located in the inner part of the silica particles and not in the thin silica shell. Hence the bleaching process only changed the particles internal structure without affecting external properties, e.g. the particle-particle interaction.

Bleaching process

To obtain a bleached area inside the particle, the LSCM laser beam was focused along the z-axis onto the mid-plane of the sphere with a power of 113µW. Moving the laser focus along the x-axis, a line in the x-y-plane (Fig.6.1) throughout the particle was bleached out. Due to the conical shape of the laser beam close to the focus point, the non-fluorescent part formed a biconcave area in y-z-plane.

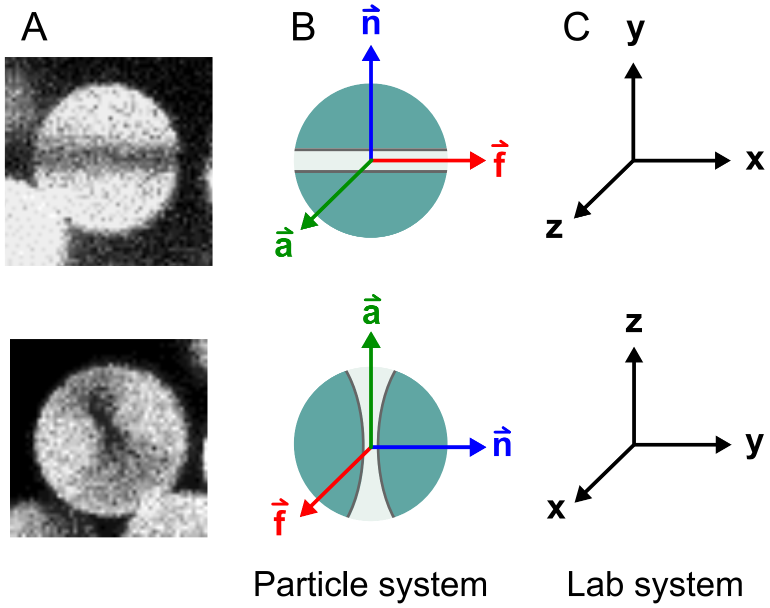

Figure 6.1: Confocal microscope image of a bleached particle with a diameter of 7.3µm (A). The bleaching geometry in the particle coordinate system is described by three orthogonal vectors (B). The particle coordinate system was then transferred into the lab coordinate system (C)

Definition of the particle coordinate system

To simplify the problem, the non-fluorescent part could be described as a plane through the particle, created by the beam direction $\vec{a}$ while bleaching. This bleached part allowed defining two additional orthogonal vectors $\vec{f}$ and $\vec{n}$, connected to the orientation of the individual particles. $\vec{f}$ defined the focal vector, pointing along the line of the laser focus during bleaching (Fig.6.1). In the starting configuration $\vec{f}$ was directed along the x-axis. $\vec{n}$ was denoting the normal vector of the plane, pointing initially into the positive y-direction. The vectors $\vec{a}$, $\vec{f}$ and $\vec{n}$ were the base vectors of the particle coordinate system.
When a particle rotates, the orientation of this particle coordinate system in respect to the lab system changes (Fig.6.2). Converting the rotated particle coordinate system, respectively $\vec{f}$ and $\vec{n}$, into a spherical coordinate system gave two sets of two rotation angles, (φ_n, ϑ_n) and (φ_f, ϑ_f) (for details of the coordinate conversion see Sec.10.5). For the initial configuration, i.e. when $\vec{n}$ was parallel to the y-axis and $\vec{f}$ to the x-axis, the rotation angles had the values (90°, 90°) and (0°, 90°). In this description of the particle orientation only three angles were independent, as φ_n and φ_f carried the same information and were only shifted by 90°. In the following the rotation of the particles was described by the angles φ_n, ϑ_n and ϑ_f.

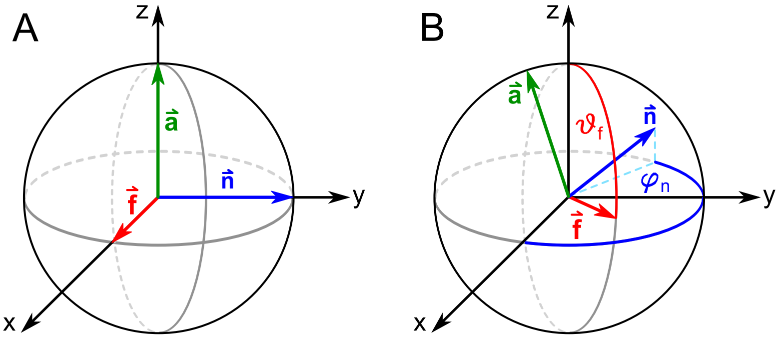

Figure 6.2: Particle coordinate system in respect to the lab system in the initial configuration (A). After rotation the orientation of the particle coordinate system has changed and is described by the angles (φ_n, ϑ_n) and (φ_f, ϑ_f) (B)

Experimental determination of the particle base vectors

The vectors $\vec{n}$ and $\vec{f}$ were determined manually from the experimental data. The bleached area could be divided in two parts. The darkest area was a line centered in the bleached area, created by the laser focus point during bleaching. This darkest line is the focal line and contained the focal vector $\vec{f}$ of the particle coordinate system. The second part of the bleached area was the two-sided concave area beside the focal line. Together the concave area and the focal line described a plane. The normal vector of this plane described the second base vector of the particle coordinate system, the normal vector $\vec{n}$.
If the focal vector $\vec{f}$ was lying completely in the x-y-plane after rotation, the darkest area was located in one single frame of the 3D image (Fig.6.3A, red solid line). The concave area appeared then as rectangular dark areas in frames above and below the

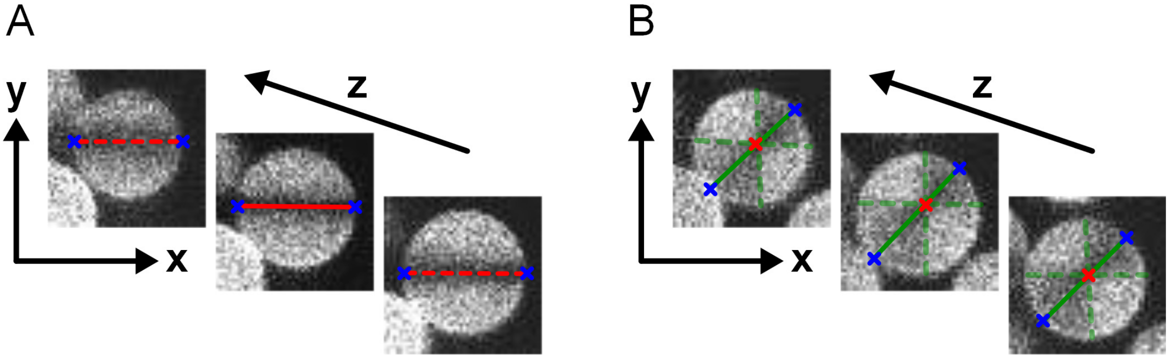

Figure 6.3: Determination of the base vectors of the particle coordinate system. Particle with the focal line lying in x-y-plane (A) and with the concave area lying in the x-y-plane (B). The focus vector $\vec{f}$ is denoted with a red line or red crosses respectively, points of the plane for calculating the normal vector $\vec{n}$ are denoted with a blue cross

focal line (Fig.6.3A, red dashed line). The start and end points of the bleached areas through all frames in which the bleached particle was visible remarked points on the plane (Fig.6.3A, blue crosses). By fitting a plane equation through this points, the normal vector $\vec{n}$ could be determined. If the focal vector $\vec{f}$ was not lying completely in the x-y-plane, the darkest area of the focal line appeared as dark spots at the focus point of the concave area (Fig.6.3B, red cross). The plane points for calculating the normal vector $\vec{n}$ were centered at the end of the concave area (Fig.6.3B, blue crosses).
As the base vectors were determined independently, the degree of orthogonality was hence an indication for the uncertainty of the vectors $\vec{f}$ and $\vec{n}$. The error bars were deduced from the orthogonality condition. The deviation of the angle between the two base vectors from 90° plus an additional constant uncertainty of 5° was chosen as the total uncertainty of the rotation angle (for details see Sec.10.5).

For a proof of principle, instead of addressing each particle individually, a line in x-y-plane was bleached through the whole observation volume. Therewith eight particles were marked with an optical anisotropy. Although not all of them were bleached through the center of the particles, they were all analyzable (see Sec.6.3). However particles bleached out along a line passing through their center turned out to give the smallest error bars for the rotation angles. For this reason, the focus of the analysis was on particles, which were bleached through their center points. The later discussion was focused on two particles, as they showed two types of characteristic behavior for this system.

6.2 Rotation - Results and Discussion

6.2.1 Measurement Procedure

The explored sample consisted of cohesive silica particles dispersed in cis-decaline (see Sec.4.2.1). The particles formed a sedimented bed with a thickness of approximately 32µm. The top of the sediment was not flat, but rough (Fig.6.4), meaning that the height varied by one or two particle diameters. The observation volume had a size of 100µm×100µm in the x-y-plane and a height of 48µm in z-direction with a resolution of 512px×512px×48px in x-y-z. The indenter tip was initially placed above the observation volume, so that approximately 40µm of natant solvent was between the top most particles of the sediment and the indenter tip. Before applying the compression, a 3D image of the initial sediment was taken. Afterwards the sample was compressed stepwise and imaged after each compression step at a laser power of 0.4µW. In total eight 3D images with seven compression steps in between were performed. In the following discussion the 3D images were denoted with the corresponding compression steps, to wit compression step one is the step following measurement one, and so on.

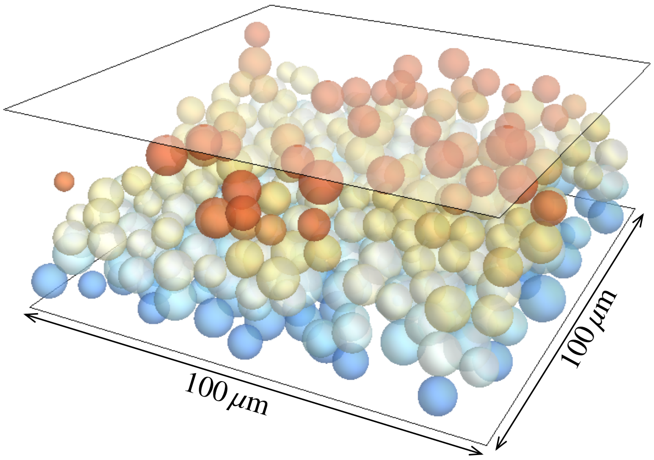

Figure 6.4: 3D reconstruction of the sediment with particle positions and diameters obtained from localization algorithms. Particles are color coded in respect to their z-position. The plane above the sediment indicates the indenter tip surface

The focus in this work was on the first steps of a compression of a granular bed. For a detailed look on this process, the displacements of the compression steps were not equidistant. The first compression step had a larger indenter displacement of 25µm to approach the tip to the sediment. Afterwards the compression step size was decreased to 5µm. In step four the tip reached the observation volume and in step five it started to touch the top sediment layer. For a closer look onto structural changes during the compression, in step six to eight the indenter tip displacement was further decreased to 2µm. The following discussion focused mainly on the compression steps four to eight, as here most of the structural changes happened.

6.2.2 Overview of the Compression

Global compression behavior

The global compression process was well represented by the averaged volume fraction (Fig.6.5). In the first three compression steps the indenter tip was approaching the sediment surface and the observation volume. After step five, when the indenter tip reached the top sediment layer, the averaged volume fraction started to increase. As the number of sediment particles did not change during compression, this increase in the averaged volume fraction was a compaction of the granulate sediment. The nearly constant particle number showed that in the early stages of the compression the horizontal stress was not high enough to lead to a particle flow outwards of the observation volume.

Figure 6.5: Averaged volume fraction versus compression step. The lines are a guide for the eye

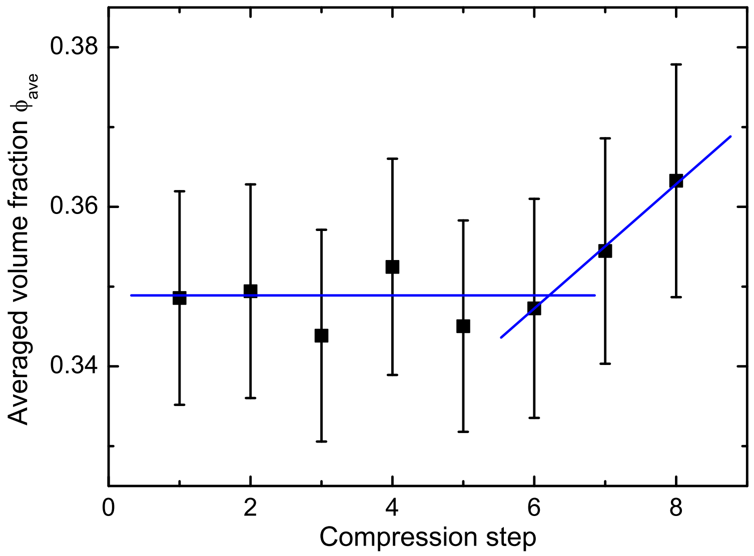

Local compression behavior

The local behavior of a sediment under compression was represented by the z-dependence of the local volume fraction distribution (Fig.6.6). The initial local volume fraction profile showed a plateau of 20μm thickness and decreased slowly with increasing sediment height. This decreasing local volume fraction for heights from 20μm to 35μm reflected the rough structure of the top part of the sediment (Fig.6.4). For sediments with a smoother top surface, a steeper decay of the local volume fraction distribution in this region would be expected. The plateau had a number of small peaks, indicating a layering of the particles induced by sedimentation in the bottom part of the sediment. The mean volume fraction of the plateau was $\phi_{plateau}(z) \approx 0.45$, a moderate particle concentration. This volume fraction was consistent with the weakly cohesive character of the particles, as it was lower than random close packing of hard spheres ($\phi \approx 0.64$). During the approaching of the indenter tip to the sediment surface no remarkable movements of the particles took place, which means that hydrodynamic effects on the particle motion were

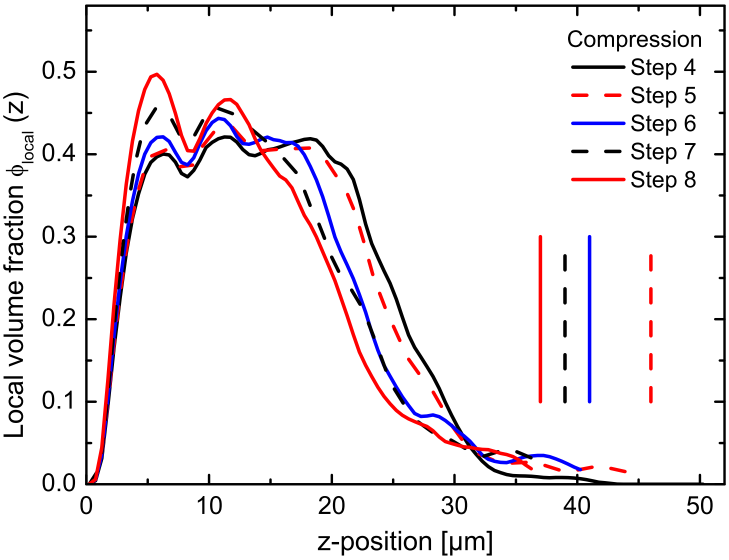

Figure 6.6: z-dependence of the local volume fractions during the compression steps four to eight. The vertical lines indicate the z-position of the indenter tip surface. The vertical line for step four is out of the z-range of this graph

negligible (see Sec.4.2.1). The local volume fraction profiles of these three approaching steps are not shown, but they were similar to the volume fraction profile of step four (Fig.6.6). The vertical lines indicate the z-position of the indenter tip surface for the following compression steps.
Between compression step four and five a decrease of the local volume fraction in the top part of the sediment ($z > 20\mu m$) and an increase of the layer peaks occured. This means that already a slight compaction of the sediment took place after step four, although the indenter touched the top sediment layer first in compression step five. With ongoing compression, a further increase of the first and the second peak of the plateau occurred, as indicated in the local volume fraction profiles $\phi_{local}(z)$ of steps five to eight. The thickness of the plateau part did not increase during the compression process, but rather decreased. Furthermore, the decreasing slopes of the volume fractions were resembling each other for all steps, indicating that the rough surface of the sediment remained during these initial steps of the compression. This is a hint that mainly the compaction occurred in the lower part of the sediment. Thus, the observed results of the initial steps of a compression were different to what would be expected for later stages of compression.

Further 3D reconstructions of the sediment with the local volume fractions of single particles were explored. Fig.6.7 visualizes the particles projected on the x-y- and x-z-plane with colors indicating the local volume fraction. The red circles show the positions of the bleached particles (see Sec.6.1). Between the 4th and the 5th compression step, the formation of particle chains between the sediment and the indenter (Fig.6.7, step six) was observed. Although electrostatic interaction between particles could be neglected (see Sec.4.2.1), a charging of the surface due to the presence of a strongly charged indenter tip surface might occur. Hence this particle chaining might be due to an electrostatic potential difference between the indenter and the substrate. Additionally a fracture appeared in the structure (Fig.6.7, step eight), leading locally to a reduced volume fraction in this region. This fracture opened wider during the compression and affected the translational and rotational motion of particle one (P1), as it was situated at the rim of the fracture.

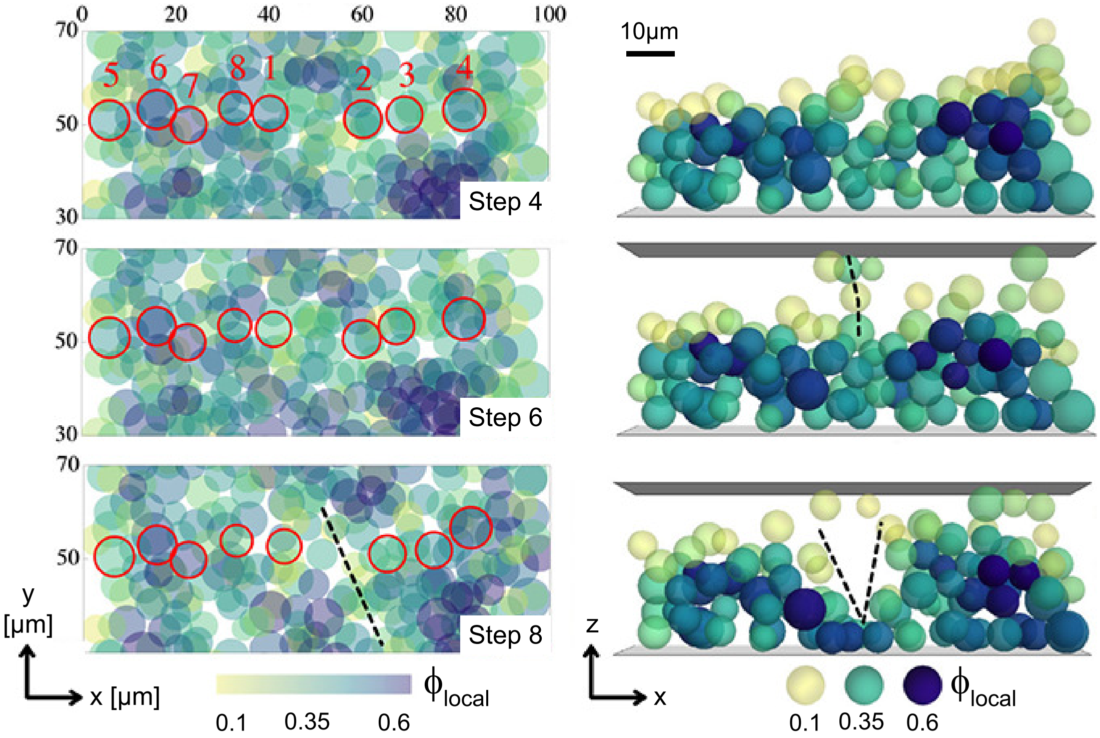

Figure 6.7: 3D reconstruction of the particle structure in x-y- (left column) and x-z-plane (right column). All particles in the left column are translucent. The color bar indicates the local volume fraction. Bleached particles are marked with red circles. The dashed line shows the particle chain (step six) and the fracture formation (step eight)

6.2.3 Rotation and Translation of Single Particles

Local structure near bleached particles

Eight particles were marked anisotropically via bleaching and followed during compression. To investigate the influence of the local structure and its change onto the single particle motion, the number of contacting particles and their local volume fraction ϕ_{local} for each compression step was determined. The averaged number of contacts in the sediment for all particles and all compression steps was around five. All bleached particles with contacting particles equal or less five were hence in a locally dilute region, bleached particles with more contacting neighbors in a relatively densely packed region (Fig.6.8). Three particles were in a relatively densely packed region, three others were in a less dense region. A derivation of the number of contacts for particle five (P5) was not possible, as it was lying close to the observation volume boundary and not all adjacent particles were imaged. In general the local environment of these particles was almost

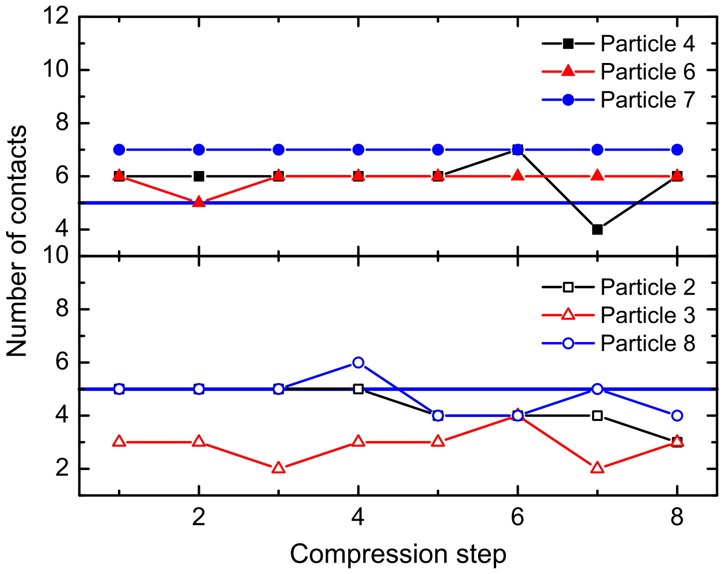

Figure 6.8: Change of the number of contacts of the bleached particles. Top inset: Particles in a locally dense region. Bottom inset: Particles in a locally diluted region. The blue line indicates the averaged number of contacts over the entire sediment

unchanged during the compression. Consistent with the number of contacts, the local volume fraction for the bleached particles showed the same behavior and was almost unchanged with compression (Fig.6.9). The calculation of ϕ_{local} for particle five (P5) was not possible, as the Voronoi tessellation was not accurate here (see Sec.5.2.1). Particles four, six and seven were in a similar dense local environment and their development of ϕ_{local} of was equivalent to P5.

In contrast to the particles discussed before, the local environment of particle one was changing drastically. At the beginning P1 was in a locally dense state with a local volume fraction of $\phi_{local} \approx 0.45$ (Fig.6.10). After compression step four a fracture appeared, while particle one was located at the rim of this fracture. Due to the strong structural

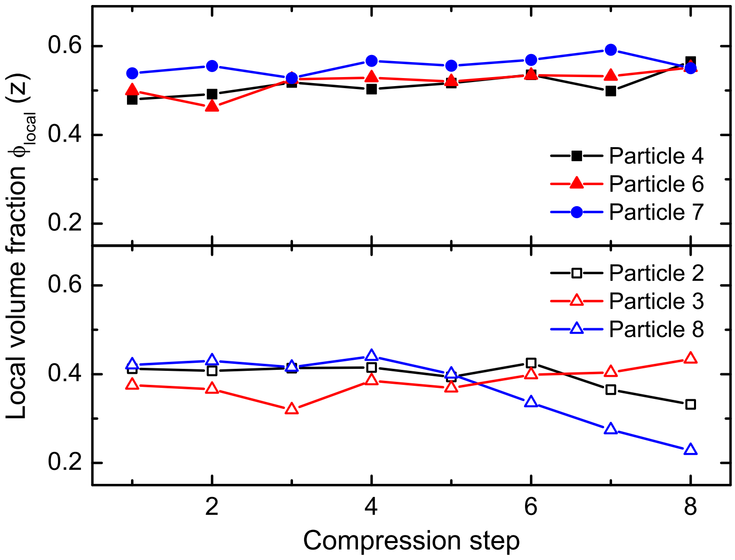

Figure 6.9: Change of the local volume fractions of the bleached particles. Top inset: Particles in a locally dense region. Bottom inset: Particles in a locally diluted region. Errors bars are not shown here, but are comparable to the ones of particle one (see also Fig.6.10)

changes both the number of contacting particles and the local volume fraction dropped. The translation and rotation of two bleached particles, namely particle one (P1) and particle five (P5) were here discussed in detail. P1 and P5 were both bleached through their particle center and were hence easily analyzable. They were typical examples of particles moving in a region with low and high local volume fraction, respectively.

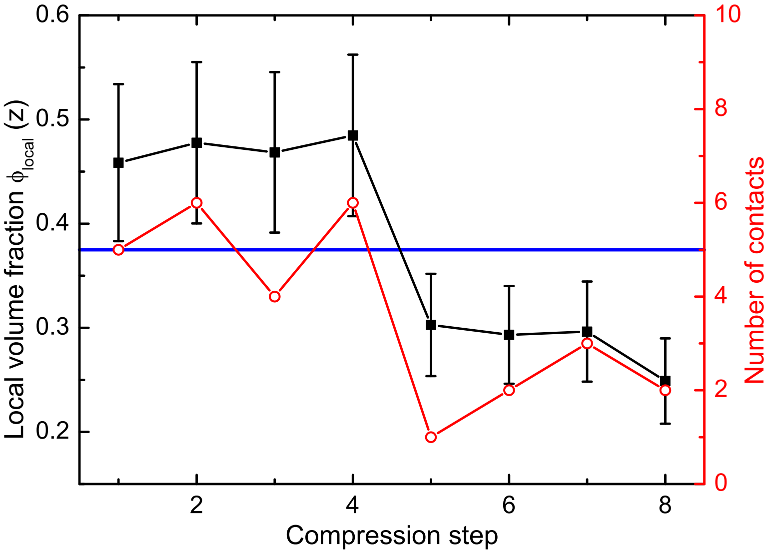

Figure 6.10: Number of contacts and local volume fraction of the bleached particle one. The number of contacting particles and the local volume fraction decreased after compression step four, as particle one was situated at the rim of a fracture, which occurred in the sediment. The blue line indicates the averaged number of contacts over the entire sediment

Rotation and translation of particle one and five

As during the compression process ϕ_{local} around P1 decreased due to a fracture formation, this particle exhibited the most significant rotation. Between compression steps four and six the rotation angles decreased. After step six a large increase of ϑ_n of about 100° was

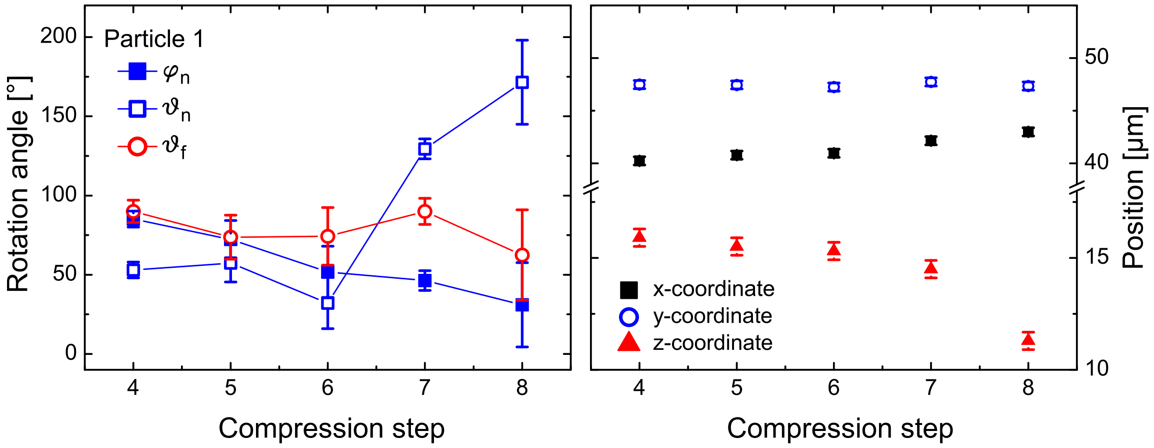

Figure 6.11: Rotation angles and coordinates of particle one

observed (Fig.6.11). In contrast to this, the position of P1 changed only slightly. This is illustrated by the 3D reconstruction of P1 and its local environment (Fig.6.12). It is visible that P1 was located at the boundary of the fracture formation line. Particles being left below of P1, as shown by opaque gray, were resting during the compression steps. Particles interacting from the right side were more mobile and were shaded translucent. The rotational motion of P1 is visualized by three vectors: the red and blue arrows indicate the focal and normal vectors, the green arrow is its vector product. The contact vector to its adjacent neighbor is indicated in orange. Here it is clearly visible that until step six the particle only had a rotational motion. Taking the contact with its neighbor into account, this motion could be described as a torsion between two particles. The contact itself between P1 and its adjacent particle was not affected by the compression. After step six the contact probably broke and the large increase in the rotation angle ϑ_n and a moderate change in the position occurred. The rolling motion might be overlayed by an additional sliding motion. Compared to the translation the rotational motion set in earlier. Due to the lower coefficient of rolling friction (see Sec.4.1.2), the rotational motion was favored and was more sensitive on structural changes than the translation.

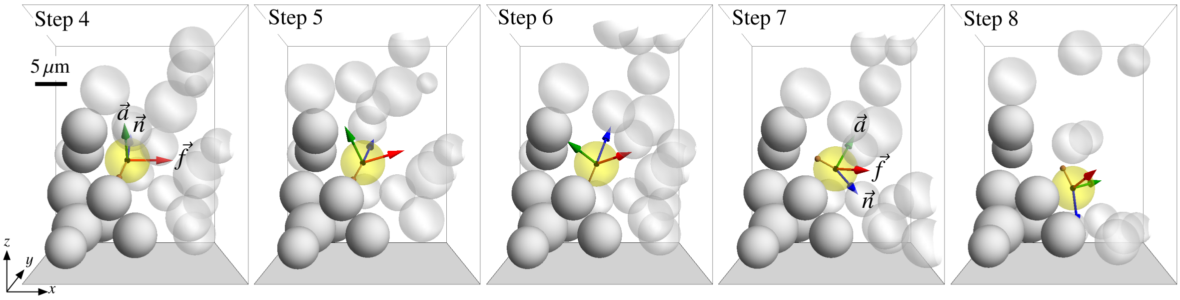

Figure 6.12: Visualization of rotation and translation of particle one. Resting particles are shown by opaque gray, the others translucent. The red and blue arrows indicate the focal and normal vectors, the green arrow its vector product

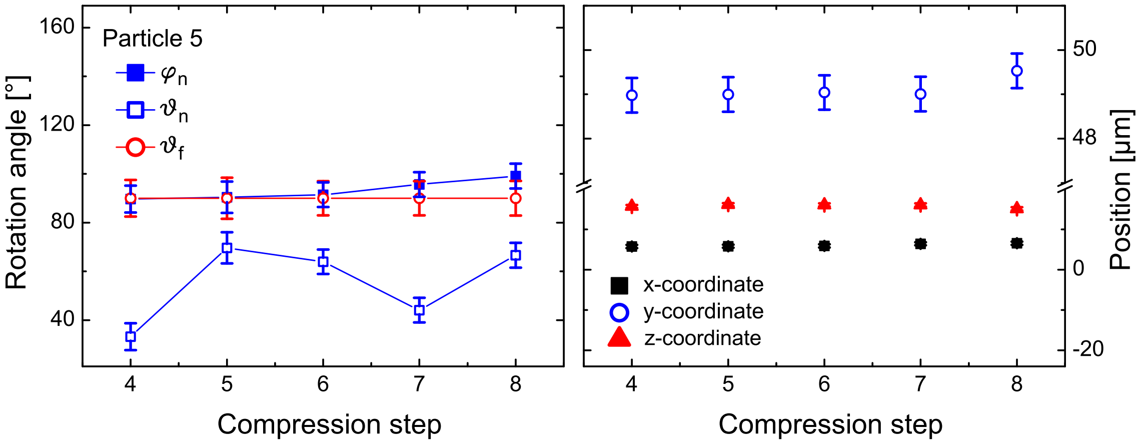

Figure 6.13: Rotation angles and coordinates of particle five

Particle five (P5) showed an opposite behavior to P1, as it was in a local dense region (Fig.6.9). During the compression no significant changes in the local structure occurred. Only the rotation angle ϑ_n had a slightly higher variation than the other two, but was still significantly smaller than compared to particle one (Fig.6.13). According to that, only small changes in the rotation angles and the translational motion of P5 were observed.

6.3 Automatic Detection of the Particle Orientation

The determination of the particle orientation was done in this chapter optically by hand. For a fast and efficient determination of the particle orientation an automatic detection algorithm is required. As the particle had after the bleaching process no longer a spherically symmetric but an anisotropic intensity distribution, the concept of an 'inertia tensor" could be used. Therewith the inertia tensor of the bleached particle is calculated, whereby the pixel intensity represents the inertial mass. After a principal component analysis (principal axis transformation) the particle coordinate system (respectively $\vec{f}$ and $\vec{n}$) could be determined and hence the particle orientation. This concept does not rely on particles bleached through their center. For the case that the particles are bleached through their mid-plane, the principal component analysis is a diagonalization of the inertia tensor and the particle base vectors are identical to the tensor main axes. In a different particle system of hollow spheres under deformation this technique has already been used for determing the particle orientation [99].

For the above described automatic detection the particle positions and diameters have to be determined reliably. The used localization algorithm would fail in the case of a bleached particle, as here the intensity profile is no longer spherically symmetric. To solve this problem 2-colored particles, i.e. particles labeled with two different dyes, could be used. One color will partially be bleached out, creating anisotropically marked particles. The second color remains unbleached. With the non-bleached color, the particles have a spherically symmetric intensity distribution and their position and diameter can be determined as described in Sec.5.1.2. Once the positions and diameters are obtained

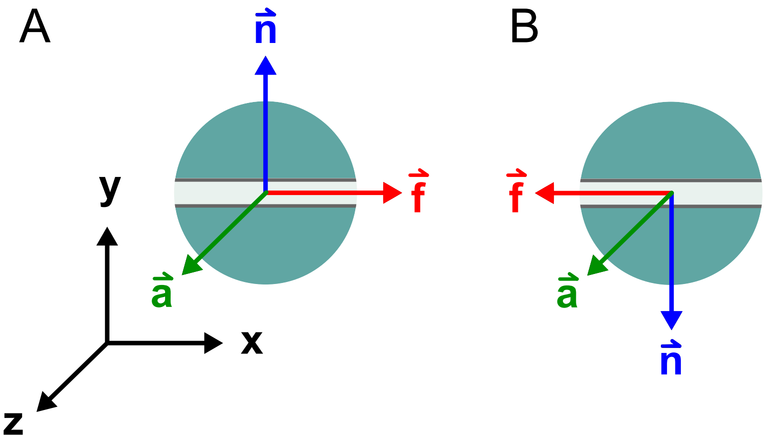

Figure 6.14: Particle coordinate system after the principal component analysis in the unflipped (A) and flipped (B) state. In both cases the coordinate system describes the orientation of the bleached particle with the same handedness, but the direction of the base vector in respect to the lab system differs. this leads to different rotation angles

the inertia tensor of the intensity distribution is calculated. Afterwards a principal component analysis is performed. The principal axes are then oriented along the base vectors $\vec{f}$ and $\vec{n}$ of the particle coordinate system (see Sec.6.1). This principal component analysis gives only the orientation, but not the direction of these base vectors.
In some cases the direction of the calculated particle coordinate system is flipped, i.e. two base vectors were shifted by 180°, after the principal component analysis (Fig.6.14). First tests have shown that such flips occur frequently and limit the usability. Once a flip occurs between two consecutive images, a wrong development of the rotating angles for a measured serie of 3D images is obtained. This flip problem can be solved by describing the rotation with quaternions [100] instead of rotation angles.

6.4 Conclusion and Outlook

Conclusion

In this chapter a novel technique was introduced for measuring the rotation of micrometer sized spherical particles. The particles were marked with an optical anisotropy by photobleaching a part of the fluorescent dye. As this bleaching process only affected the internal structure, the isotropic particle-particle interaction was not changed. With the specific bleaching geometry used here (see Sec.6.1) the particle was marked with its own coordinate system, allowing to detect the full orientation in 3D and all rotation angles.
Experimentally structural changes and their influence on the rotation and translation of polydisperse cohesive silica particles in a compression experiment were studied. Globally a compaction of the sediment under compression was observed. On a local scale during the initial compression steps the compaction predominantly occurred in the lower part of the sediment. Further complex structural changes of the sediment happened. Phenomena such as particle chain formation and fracture formation were observed. The local structural changes, in particular the development of the local volume fractions, were related to the single particle motion of the bleached particles. Their rotation and translation strongly depended on the local structure of the sediment. Particles located in locally dense regions showed a less pronounced translational and rotational motion. In regions, where mainly the structural changes happended, the particles showed a significant rotation before the onset of a translational motion. Due to the lower coefficient of friction (see Sec.4.1.2), the rotational motion was favored and was more sensitive on structural changes than the translation.

Outlook

The measurements so far were a proof of principle of this new technique. In future with 2-colored particles and an automatic detection of the particle orientation a higher amount of particles could be analyzed. In this chapter only the behavior of the single particle motion under compression was investigated. With an increased particle statistics the current relationships between the structural changes and single particle motions, which were drawn here could be verified also for different applied mechanical load as shear.

With a higher number of bleached particles also possible anisotropies in the rotational behavior along the sediment height could be investigated.

7 Shear Dilatation and Shear Zone Formation

When exposed to high mechanical stress, many granular systems behave no longer elastically, but start to flow [101, 102]. Slow shearing of dense granular matter is often characterized by a volume change, i.e. shear dilatation and the formation of shear bands [103, 104]. For many types of granular matter Schall et al. give an overview of shear bands with their principal mechanisms and characteristics [105]. Stress-strain relations for bulk systems are widely examined in simulations and experimentally. Thornton et al. [106] investigated with DEM simulation a cohesionless powder under shear and the evolution of stress-strain-dilatation, which qualitatively agreed with experiments. Beside of this, the influence of the applied stress on the formation of shear zones and the single particle motion inside this zone is still under investigation. Pattern formation in shear zones was investigated by Abedi et al. in a dense sand packing under a plane strain compression [107]. With digital image correlation they tracked displacement fluctuations inside the system. They observed the formation of vortices, which are correlated with fluctuations in the macroscopic shear stress. Lätzel et al. had a closer look on the single particle behavior under shear [108]. They compared the motion of polydisperse 2D disks in a Couette cell with molecular dynamics simulations. Following the positions and orientations of the disks revealed local density fluctuations and shear banding near the inner shearing ring. With 3D scanning techniques experimentally single particle motions inside the shear zone could be detected. Losert et al. analyzed the particle arrangement upon shear reversal in 3D using laser sheet scanning [109, 110]. They observed irreversible deformations in the shear zone due to particle reorganizations. Hasan et al. investigated the behavior of sand under a quasi-static shear [96] with X-ray tomography. As sand is polydisperse and non-spherical, they were able to follow the translation and rotation of a small number of grains.

In this work the relation between the global and local shear behavior in dependence on the applied uniaxial shear was explored in 3D. The focus was on the formation of shear zones and shear dilatation on a single particle level. This chapter is based on the manuscript “Sheared granulates in strain-controlled geometry - A confocal microscopy study on a single particle level” by Jennifer Wenzl, Ryohei Seto, Roman Mayer, Thomas M.L. Palmer, Günter K. Auernhammer [111].

7.1 Measurement Procedure

The explored sample was made of cohesive silica particles dispersed in cis-decaline (see Sec.4.2.1). In shear experiments two different geometries concerning the tilting angle of the upper shear plate were investigated. One had a wedge geometry with a tilting angle of 4° along the y-axis (Fig.7.1). The second one was a parallel plate geometry with a parallelism better than 0.33°. The shear was applied stepwise with step sizes of 2µm and a total shear displacement of 50µm in the wedge geometry and 1µm step size and 26µm total shear displacement in the parallel plate geometry. Before applying the shear and after each shear step the particle configuration was imaged for both geometries in an observation volume of 100µm×100µm in x-y-plane and 38µm in z-direction with a resolution of 512px×512px×48px. Before starting the shear, the samples were compacted to averaged volume fractions in the order of 0.53 by decreasing the plate distance. The used load cell geometry was different compared to classical shear cells [68]. The used cell had a constant plate distance, which means that the measurements were strain- and not force-controlled. Furthermore, no sidewalls were existing to confine the granulate volume laterally. The influence of the load cell geometry, i.e. the absence of the confining side walls will be discussed later in Sec.7.2.3.

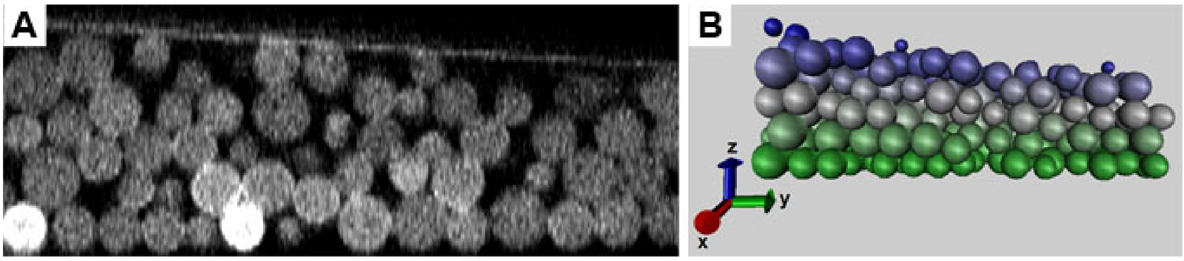

Figure 7.1: Laser scanning confocal microscope image of the initial particle configuration in y-z-plane (A) and 3D reconstruction (B). Due to the precompaction of the sample the particles filled the total cell height

7.2 Wedge Geometry

7.2.1 Global Behavior under Shear

To investigate the global bulk behavior of the examined model granulate the averaged volume fraction ϕ_{ave} (see Sec.5.2.2) was plotted versus the plate displacement of the upper shear plate (Fig.7.2). The initial averaged volume fraction was $\phi_{ave} = 0.539 \pm 0.017$. At the beginning of the shear ϕ_{ave} remained constant. At a plate displacement of 4µm (corresponding to a global shear strain of $\gamma = 0.13$) a linear decrease set in. With ongoing shear a decrease down to $\phi_{ave} = 0.476 \pm 0.017$ was observed. After a plate displacement of 28µm the averaged volume fraction leveled off and reached a plateau. The decrease in averaged volume fraction and its delayed onset was a clear indication for shear dilatation (see Sec.2.4.3). The following plateau showed that after a plate displacement of 28µm steady state flow set in. On a global bulk scale this explored sample showed the behavior of an overconsolidated granulate under shear.

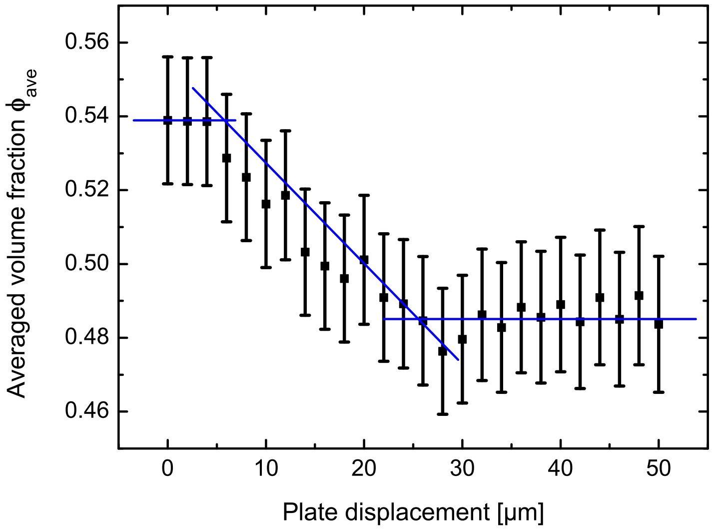

Figure 7.2: Averaged volume fraction versus upper shear plate displacement for the wedge geometry. The lines are a guide for the eye

7.2.2 Shear Zone Formation

To visualize local variations in the structure the local volume fraction distribution $\phi_{local}(z)$ versus the z-position was plotted for different shear plate displacements (Fig.7.3). The position $z = 0$ corresponded to the bottom shear plate. The particle layering at lower z-positions was induced by sedimentation to the bottom shear plate and the precompaction before shearing. With increasing z-position the layering became less

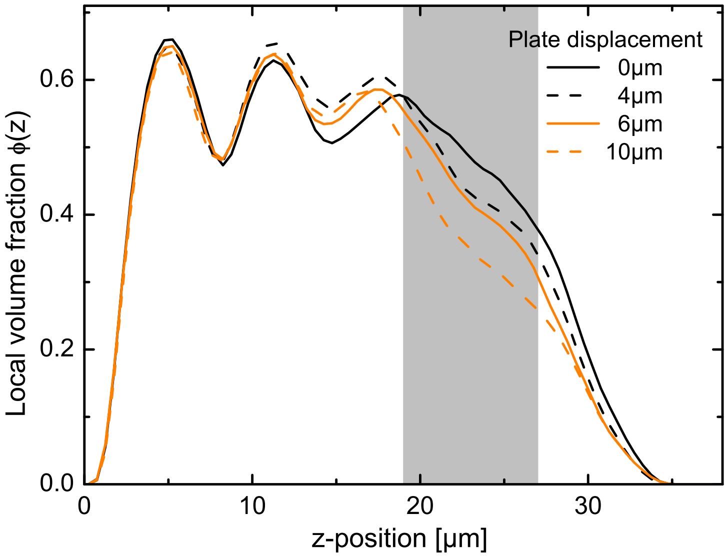

Figure 7.3: Local volume fraction distribution in dependency of the z-position at the beginning of the shear process for the wedge geometry. In the upper part of the granulate bed a reduction of the local volume fraction distribution indicated the onset of particle flow and the formation of a shear zone. The locally diluted region is shaded in gray

pronounced. Already in the initial configuration in a region at the top of the sample (between 19µm and 27µm in z) the local volume fraction was slightly lower. This "locally diluted region" might be influenced by the precompaction with an tilted shear plate (see Sec.7.4) and played a role in the following shear zone formation.
At the beginning of the shear a further dilution of the particle number density in this locally diluted region of the granulate bed was observed. This decrease in $\phi_{local}(z)$ was an indication for a beginning particle flow and the formation of a shear zone. Already at a shear plate displacement of 4µm the local volume fraction here was reduced significantly, e.g. at a z-position of 23µm a reduction from roughly $\phi_{local} = 0.48$ to $\phi_{local} = 0.43$ occurred. This is in contrast to the global behavior, as here the decrease in the averaged volume fraction was observed for shear plate displacements larger than 4µm. This shows that shear dilatation and shear zone formation set in before it could be detected by a change in global bulk parameters as the averaged volume fraction.
This locally diluted region played an important role during the shear dilatation. In overconsolidated granulates the particle rearrangement occurs by increasing the granulate bulk volume. This is usually obtained by a change in the plate distance of the load cell. In load cells with constant plate distance the rearrangement could only happen, if a certain free volume is provided, e.g. in a locally diluted region. In the case of the cell geometry used here, the locally diluted region enhanced the shear zone formation and the shear dilatation.
With ongoing shear the shear zone spread further into the sample, as the local volume fraction decreased already at z-positions larger than 18µm (Fig.7.4) and got steeper. Nevertheless the shear zone remained localized in the upper half of the sample over the

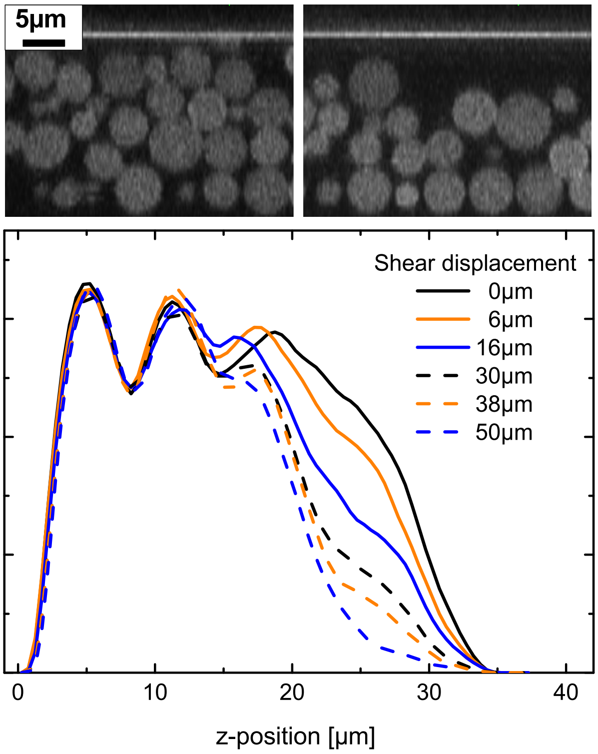

Figure 7.4: Laser scanning confocal microscope image of the sample in x-z-plane at the beginning of the shear (top left) and at a shear plate displacement of 16µm (top right) for the wedge geometry. Local volume fraction distribution in dependency of the z-position over the entire shear process (bottom)

entire shear process. Near the shear plate ($z > 25$µm) a further reduction of the local density was observed for shear plate displacements larger than 30µm, although from the global behavior a steady state flow would be expected. In contrast to the significant changes in the upper part of the of the granulate, the density profile $\phi_{local}(z)$ in the two lower layers ($z < 15$µm) remained almost unchanged during the shear.

7.2.3 Single Particle Motion in the Shear Zone

Particle trajectories

For all 3D images the particle positions and diameters were determined. Trajectories were computed if the motion of the particle was traceable at least in ten consecutive 3D images (see Sec.5.3.1). The efficiency of the particle tracking varied with the z-position within the sample (Fig.7.5). In the bottom layer ($z < 8$µm) it was possible to follow the motion of over 90% of the particles. This ratio decreased continuously to roughly 25% in the two uppermost layers ($z > 25$µm). On average 60% of the localized particles were tracked, corresponding to 656 analyzed particle trajectories.

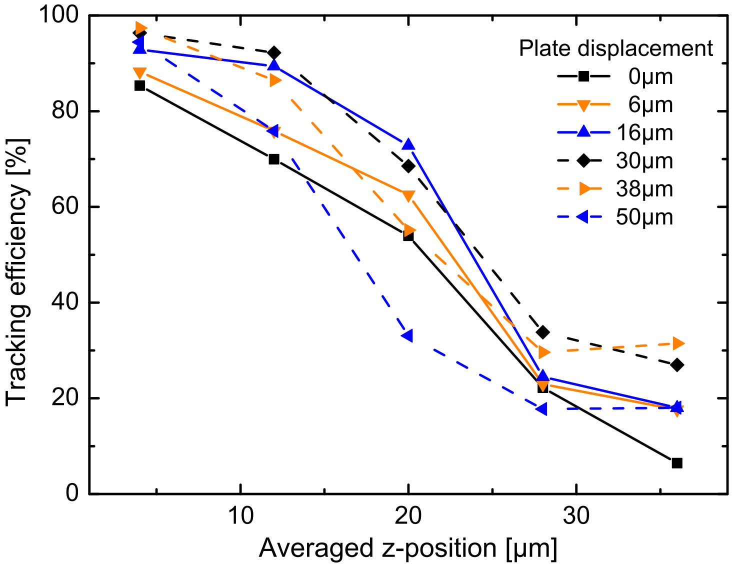

Figure 7.5: Tracking efficiency for different shear plate displacements in dependence of the z-position for the wedge geometry. In the upper part of the granulate bed the efficiency dropped down due to fast processes, which could not be followed with the tracking algorithm

Processes that involve particle displacements larger than one particle diameter can not be captured in the tracking process. Due to the shear flow and the shear zone formation in the upper part of the sediment, large particle displacements in this region occurred, although the shear step size was smaller than one particle radius. An additional origin for large particle displacements in this region can be shear dilatation. Elastic energy, which was stored in force chains, was suddenly released when the force chains broke. The release of the elastic energy led to particle displacements which were too large to be followed with the tracking algorithm. In total the averaged displacements of the particles in the upper sample layers were systematically underestimated since selectively the fast particles were not tracked. With low tracking efficiencies fast processes could be identified. The tracking efficiency can hence be used as a new parameter for single particle dynamics of granulates under shear and as an indication for shear flow.

Particle displacements

The total displacements (the end-to-end distances of the trajectory) along x, y and z were calculated for each tracked particle (see Sec.5.3.2). The total displacement for each particle was averaged over the entire length of its trajectory to obtain an averaged displacement per shear step. The averaged displacements in the x-, y- and z-direction were plotted versus the corresponding z-position (Fig.7.6 and Fig.7.7). Particles sticking at the lower part of the shear plate are indicated with orange triangles. The region of the sample with particles with a low tracking efficiency is shaded in gray.

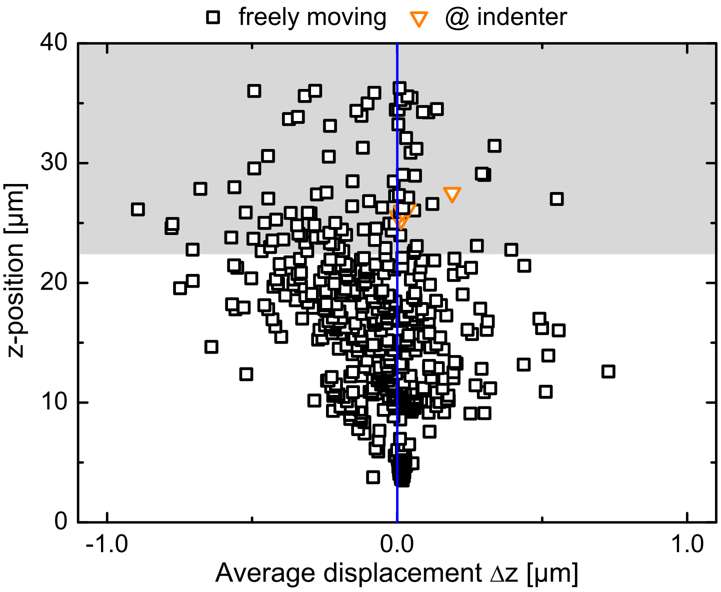

Figure 7.6: Initial particle z-position versus the average displacement per shear step along the z-axis for each tracked particle for the wedge geometry. Particles sticking at the lower part of the shear plate are indicated with orange triangles. The fraction of particles with a low tracking efficiency is shaded in grey

Concerning their motion along the z-axis, particles showed negative and positive displacements (Fig.7.6). This shows that with the exception of the lowermost layer, particles moved upwards and downwards throughout the sample. The averaged vertical displacement per shear step reached typical values of up to 0.5µm, which was 25% of the maximum lateral motion per shear step. Particles located in the two lower layers ($z < 15$µm), where the density profile $\phi_{local}(z)$ almost remained unchanged during the shear (Fig.7.4), constantly changed z-position. As the maximum lateral motion over the entire shear process was in the order of one particle diameter, particles from this region were also exchanged with particles from the shear zone. In contrast to the expectations deduced from the volume fraction development, particle rearrangement was observed also outside the shear zone and a mixing of flowing and non-flowing regions occured.

Along the x-axis, particles in the upper part of the sample were mainly following the applied shear direction (Fig.7.7). But as the tracking of the particles in this region was not efficient enough, no further conclusions could be drawn. Most of the particles at

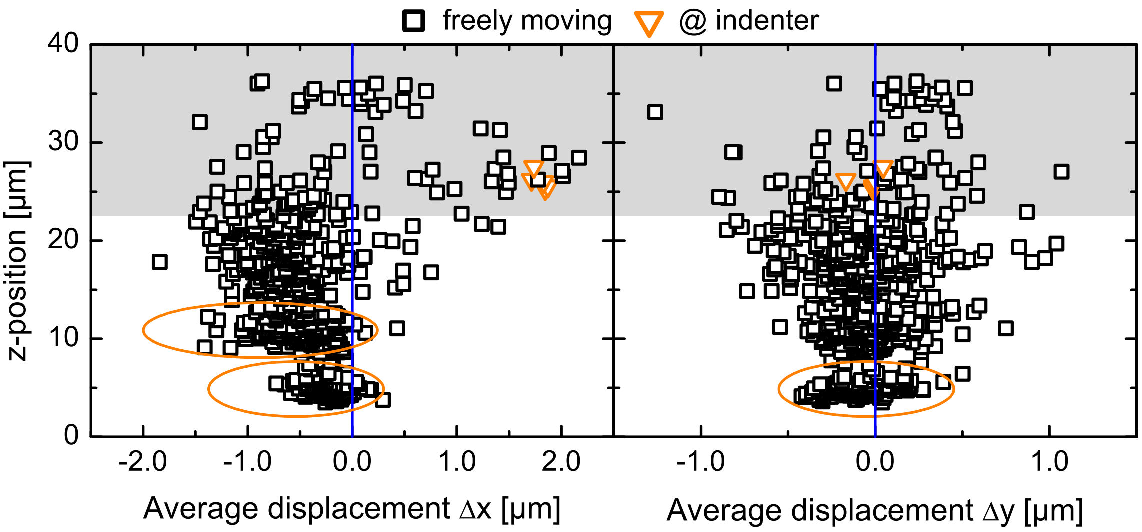

Figure 7.7: Initial particle z-position versus the average displacement per shear step along the x-axis (left) and y-axis (right) for each tracked particle for the wedge geometry

the bottom plate had a non-zero motion, i.e. they were not fixed to the plate. A large fraction of particles at z-positions lower than 25µm was moving mainly into the negative x-direction, opposite to the shear. This motion was effected by the special geometry of the used load cell and was discussed in the following. A symmetric scattering of the particle motion along the y-axis occurred. The averaged particle displacement per shear step got the largest at the boundary of the shear zone, i.e. between the flowing and non-flowing region. A symmetry breaking due to the tilting of the upper shear plate along the y-axis was not observed.

Influence of load cell geometry

During the shear the plate distance and hence the volume underneath the shear plate was constant. As a consequence the total number of particles in the shear gap had to decrease along with the averaged volume fraction. As there were no sidewalls, which confined the granulate volume laterally, the increasing horizontal stress (see Sec.2.4.1) squeezed the particles radially out of the shear gap. The initial motion of particles in the bottom part of the sample with the applied shear direction was then overlayed by the radial squeeze flow. Fig.7.8 showed the particle trajectories in the lowest layer ($z < 8$µm). Since the observation volume was slightly off-center to the upper plate, the preferred motion of the particles in the negative x-direction (Fig.7.7) can be explained in this way. An additional component on this radial squeeze flow due to the tilting of the upper plate which is widening the sample towards smaller y-values was not large enough to be detected in the particle trajectories.

Figure 7.8: 3D reconstruction of the particle positions at all shear steps for the wedge geometry, from the first measurement (blue) to the last measurement (green), showing the radially outwards directed squeeze flow. For a better visualization, the particle are reduced in size. The shear plate was moving along the x-direction. The cross indicates the center position, the dashed line the rim of the shear plate

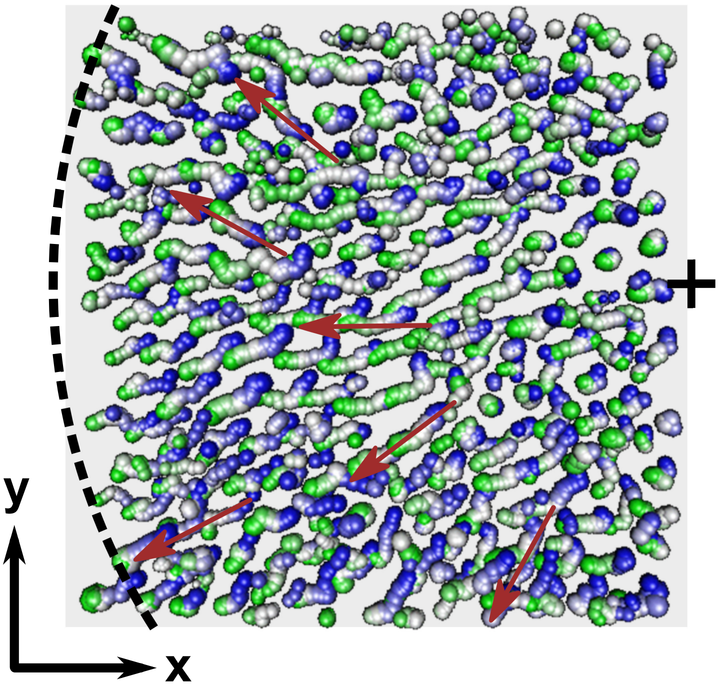

7.3 Parallel Plate Geometry

In a further experiment, the tilt angle was adjusted to be as small as possible (less than 0.33°) so that the sample was measured in a parallel plate geometry. The shear step size was halved to 1µm for improving the tracking efficiency in the upper part of the sample near the shear plate. The sample height of 25.6µm was comparable to the height in the wedge geometry sample at the narrow side of the wedge. Also the initial averaged volume fraction $\phi_{ave} = 0.511 \pm 0.017$ was chosen to be similar to the first sample.

Global shear behavior

The granulate sediment in the parallel plate geometry had a slightly lower initial averaged volume fraction than in the wedge geometry (Fig.7.9). Over the following entire shear process the averaged volume fraction ϕ_{ave} was only varying slightly and remained nearly constant. On a global bulk scale within the errors this explored sample showed the behavior of a critical consolidated granulate under shear (see Sec.2.4.3).

Local shear behavior

A particle layering due to sedimentation occurred also in the parallel plate geometry (Fig.7.10). In contrast to the wedge geometry, a region with a locally reduced volume fraction near the upper shear plate was not observed here. Beside that, the local volume fraction distribution $\phi_{local}(z)$ was changed only weakly during the shear. Especially near the upper shear plate, no clear decrease of $\phi_{local}(z)$ could be seen. This was a hint that in this parallel plate geometry no shear zone was formed, but that the whole granulate

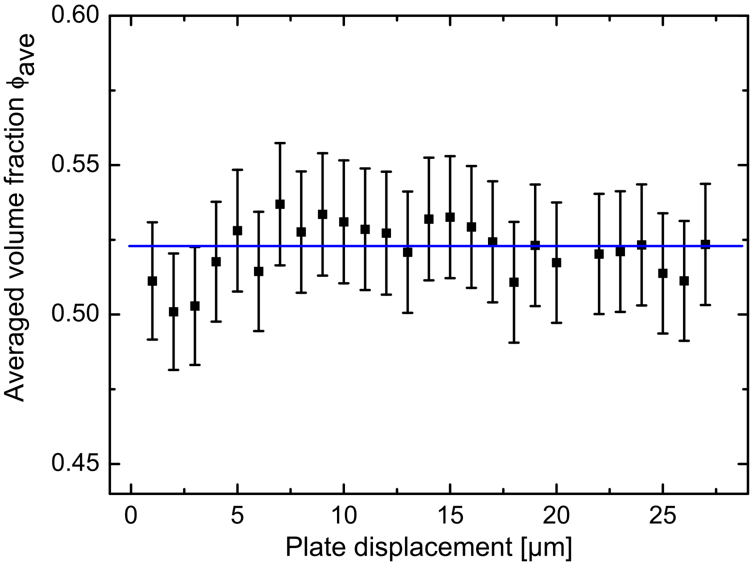

Figure 7.9: Averaged volume fraction versus upper shear plate displacement for the parallel plate geometry. The line is a guide for the eye

bulk was deformed homogeneously, as expected for granulates under steady state flow. Nevertheless the maximum height of the first layer peak ($z \approx 5$µm) decreased during the shear, while the second following peak ($z \approx 13$µm) was increasing. This indicated that here also an exchange of particles between different layers occurred.

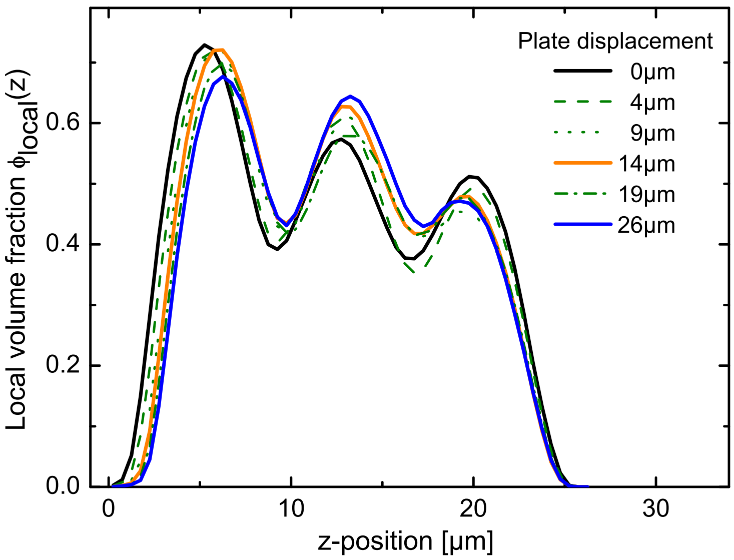

Figure 7.10: Local volume fraction distribution in dependency of the z-position for the parallel plate geometry

Trajectories and displacements

The smaller shear step size significantly increased the tracking efficiency in the upper sediment part. The tracking efficiency now only decreased slightly with increasing height in contrast to the wedge geometry. For the top most layer ($z > 17$µm) the fraction of tracked particles was on average above 70%. Due to the increased tracking efficiency a

Figure 7.11: Initial particle z-position versus the average displacement per shear step along the z-axis for each tracked particle for the parallel plate geometry. The particles in the upper sediment part showed an increased tracking efficiency

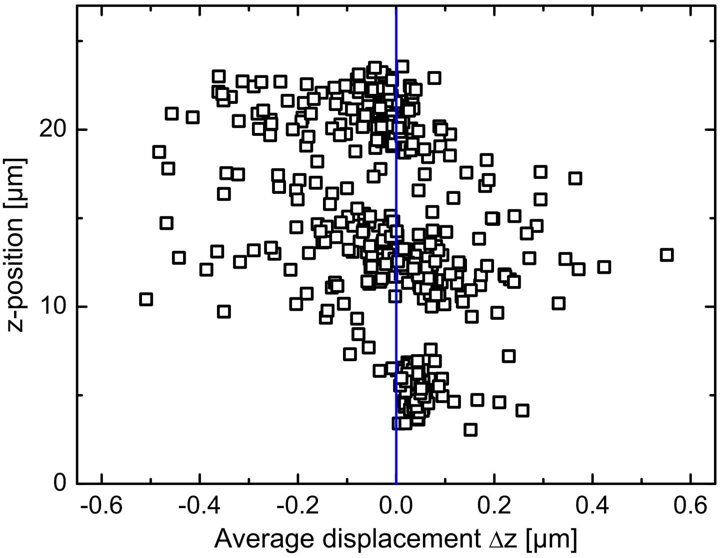

higher number of particle displacements, especially near the upper shear plate could be deduced.

The particles displacements along the z-axis had again negative and positive components, indicating the layer mixing (Fig.7.11). The exchange of particles between layers might be a global behavior of granulates under shear. Along the x-axis, the main fraction of particles was moving along the shear direction and the averaged displacements Δx built up a linear shear profile in z-direction (Fig.7.12). This linear shear profile showed that the flowing regime, i.e. the shear zone is distributed over the entire sample height. Still in the lower layers of the sample, a small fraction of particles had a negative x-

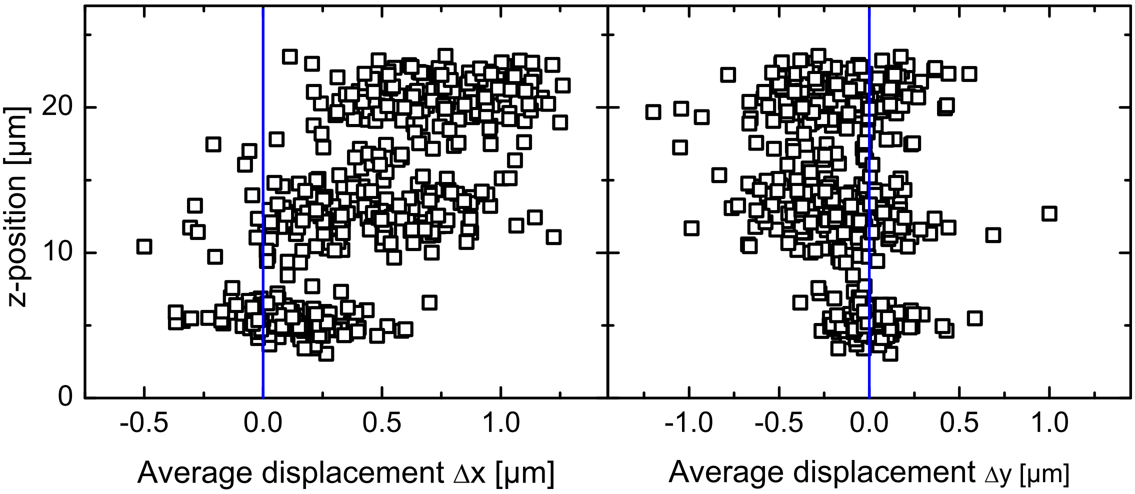

Figure 7.12: Initial particle z-position versus the average displacement per shear step along the x-axis (left) and y-axis (right) for each tracked particle for the parallel plate geometry

displacement. This negative x-displacement was an effect of the open cell geometry (see Sec.7.2.3). The observation volume and the shear plate were slightly off-centered, this caused the asymmetry in the particle displacements along the y-axis.
The influence of the open cell geometry can be more emphasized by visualizing the trajectories of the particles in the lowest layer ($z < 8$µm, Fig.7.13). At the beginning the initial motion of these particles had a clear component into the direction of the applied shear. At a shear displacement of 12µm (Fig.7.13B) an overlay with the squeeze flow set in.

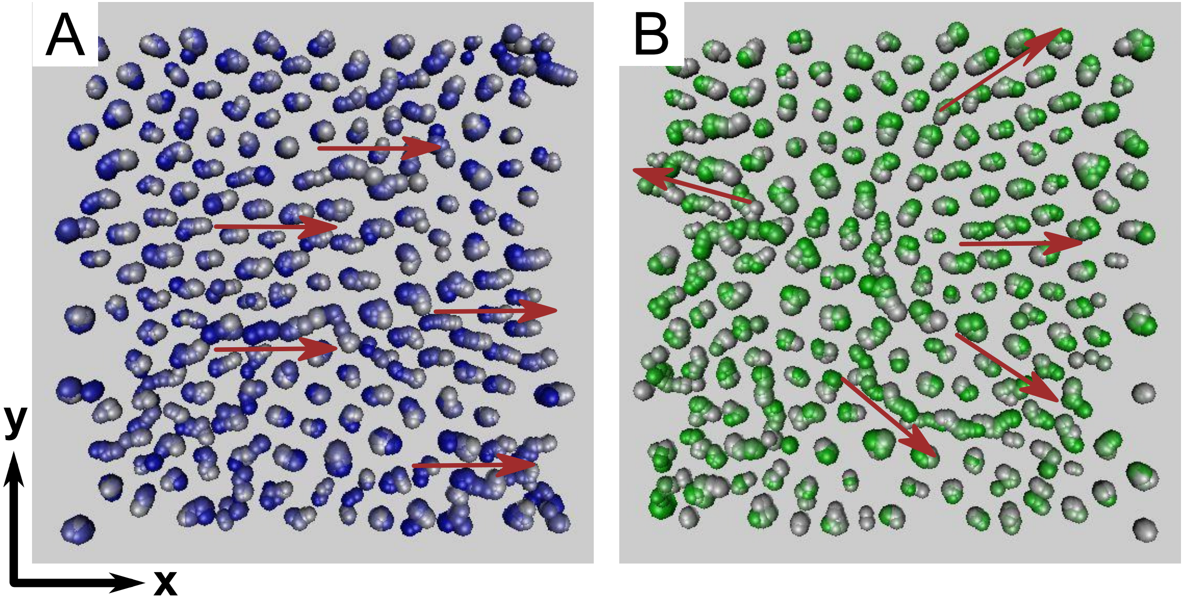

Figure 7.13: 3D reconstruction of the particle trajectories from the first (blue) to the last measurement (green). At the beginning the initial motion with the applied shear (A) was later overlayed by a squeeze flow (B)

7.4 Possible Influence of the Tilting Angle

Before starting the shear, a locally diluted region in the upper part between 19µm and 27µm in the wedge geometry sample was observed. The compression of the granulate with a tilted upper shear plate eventually led to an inhomogeneous compaction of the structure along the z-axis, creating this locally diluted region. This locally diluted region was not observed in the parallel plate geometry, although here the initial averaged volume fraction after precompaction was lower than in the wedge geometry.
After sedimentation the preferred averaged tangential plane of the particle contacts might be directed horizontally (see Sec.2.4.3). Shearing this sediment with a tilted shear plate has the effect that the applied macroscopic shear plane is not identical with this averaged tangential plane. This might enhance also the shear dilatation in the wedge geometry beside the high volume fraction in the overconsolidated regime.

7.5 Conclusion and Outlook

Conclusion

Experimentally a sedimented and precompacted bed of slightly cohesive silica particles submitted to a stepwise shear was studied. In detail two different geometries concerning the shear plate distance were examined, one wedge geometry and one parallel plate geometry. Different behavior under shear due to different initial volume fractions were observed. On a global bulk scale the explored samples showed the shear behavior, which was expected from classical shear experiments as with the Jenike cell. The sediment in the wedge geometry showed a shear behavior of a overconsolidated granulate, while the sediment in the parallel plate geometry had the behavior of a critical consolidated granulate.

In the wedge geometry a local diluted region near the upper shear plate enhanced the onset of the shear flow and shear zone formation. The decrease of the volume fraction in this region was interpreted as a result of shear dilatation. The onset of shear zone formation and dilatation on a local scale differed from the observed global behavior. These effects set in before they could be detected by a change in global bulk parameters as the averaged volume fraction.

On a single particle level shear flow and shear zone formation can be identified by following the particle trajectories. A low tracking efficiency can be a measure for these fast and high-dynamic processes. During the shear a rearrangement of particles along the sample height was observed. This was a mixing between lower lying particle layers. In the wedge geometry this exchange of particles occurred between the flowing (shear zone) and the non-flowing region. This interlayer mixing was observed in both plate geometries and was hence a global behavior of the here examined granulates. The open cell geometry with no existing side walls led to an additional squeeze flow, which overlayed the initial motion of particles in the bottom part of the sample with the applied shear direction.

Locally the behavior of the sediment under shear differed drastically from the global behavior. Global parameters as the averaged volume fraction are not sufficient to describe fully the behavior of granulates under shear. For flow and other dynamical processes as shear dilatation also the single particle motions have to be considered for understanding the complex structural changes in dense granular systems under shear or mechanical loads.

Outlook

These new insights into the local behavior of granulates under shear raised new questions, which have to be investigated experimentally. The sediment thickness was quite small compared to classical shear experiments. Here sample thicknesses of a few particle layers (less than six) were used for investigating and identifying the principal mechanism of the shear zone formation on a single particle level. In the next step larger sediments with thicknesses up to twenty particle layers should be investigated. It is expected that with this increased number of particle layers the transition to macroscopic samples and

behavior could be observed.
The main question is how large the influence of the used strain-controlled geometry is on the shear behavior. This question could be solved by using the 3D imaging in combination with a nanoindenter instead of the nano-manipulator. Commercial nanoindenter devices are able to apply mechanical loads either force-controlled with constant force and variable sample height or strain-controlled as used here. With the force sensitivity of the nanoindenter also the breakage of force chains during the shear dilatation should be detectable. The influence of the rolling motion on this force chain breakage could be addressed by giving the particles an optical anisotropy (see Sec.6.1).

8 Flow and Dynamics in Wet Granulates

In many industrial branches not only dry powders and granulates are widely used, but also granulates in the wet state. These are for example common in the oil and mining industry (e.g. oil sand) and are used for pharmaceutics and cosmetics in pastes and creams. In these systems the particles are connected via an additional binding liquid over capillary interaction. The additional binder liquid drastically changes the rheological behavior of the bulk granulate. In oscillatory shear measurements Koos et al. [112] investigated the shear strength, yield stress and viscosity of wet granulates in dependence of the amount of the binder liquid. They showed that the bulk behaved no longer viscous or weakly elastic, but highly elastic and gel-like. The influence of the additional binder liquid on the formation of shear bands was investigated numerically by Schwarze et al. [113] and was compared with shear experiments in a Couette-like rotating viscosimeter. The DEM simulations showed that the shear bands in wet granulates were qualitatively similar for dry granulates, but narrowed in size with increasing liquid content. However their model for the capillary network based on simplified pendular bridge contacts, which could not explain all details. To improve the description of capillary networks, experimental techniques for visualization are needed. Gögelein et al. [114] used bright field and confocal microscopy for investigating the capillary bridge formation between micrometer-sized spheres in 2D. For a 3D exploration of the capillary network X-ray tomography was used by Scheel et al. [115]. They investigated the number of bridges and the shape of the capillary network in dependence of the liquid content and related it to rheological bulk properties of the wet granulate, such as the tensile strength. Most of the investigations so far were on static properties of the capillary network and the particle distribution. Dynamics investigations have been done numerically with contact dynamics simulations by Mani et al. [116]. They simulated the migration of the binding liquid when the granulate was sheared. The origin of the migration was the rupture of the pendular bridges under shear and a redistribution at the particle contacts. For visualizing the dynamics of a network under capillary rising confocal microscopy was used by Krummel et al. [117]. They found out that the binding liquid can flow through thin layers on the particle surface, while the shape of the network was dependent on the shear history and capillary number.

Widely investigated were model systems, where the binding liquid is homogeneously distributed, i.e. where the binding liquid is building a connecting capillary network. In contrast wet granulate model systems with an inhomogeneous liquid distribution have been rarely in focus of research. A further complicacy is that for small granulates, i.e. fine powders, the capillary interaction gets dominant and can also be in the same order of magnitude or can even exceed common interactions, such as Van der Waals or gravitation. The focus of this chapter was the investigation of such a system, where the binding liquid forms Pickering emulsion like droplets. Explored were a single cluster and a loose bulk granulate under shear and compression. The focus was on the dynamics of the binding liquid droplets under load and their influence on the particle dynamics.

8.1 Deformation of a Single Wet Cluster

8.1.1 Measurement Procedure

The examined sample was a cluster of a wet powder. It consisted of roughly 30 silica particles and 5 droplets of the binding liquid cis-decaline (see Sec.4.2.2). For the sample preparation 50mg/ml of the HMDS-modified particles were suspended in a mixture of 85vol% NaSCN-solution (refractive index n = 1.470) and 15vol% cis-decaline, colored with Nile-Red. This sample was measured with the 1-color mode LSCM. As the refractive index of the HMDS-modified particles was 1.443 ± 0.003, a slight refractive index mismatch between the particles an the cis-decaline occured. For enhancing the contrast of the liquid-liquid interface, the refractive index of the surrounding NaSCN-solution was matched onto the cis-decaline.

The explored cluster was sticking at the side of the indenter tip surface (tip surface diameter 20μm), i.e. at the cone surface of the tip (Fig.8.1A). The bottom part of the cluster was situated at the cover slide. While moving the indenter tip into negative x-direction, the cluster was sheared and dragged along with the tip. The shear was applied stepwise in 0.25μm-steps with a total shear displacement of 7μm. The whole

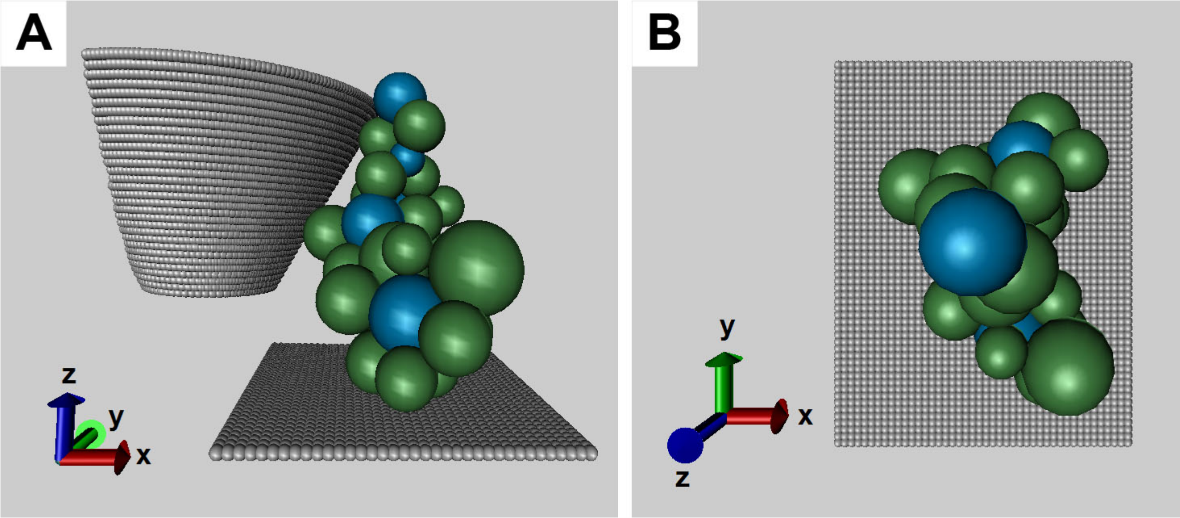

Figure 8.1: 3D reconstruction of the initial particle configuration of the wet cluster, side view (A) and top view (B). The particles are indicated with green, the cis-decaline droplets in blue. The cluster was sticking with two particles at the conical surface of the indenter tip and at the bottom cover slide

cluster was imaged in an observation volume of 100µm×100µm×40µm with a resolution of 512px×512px×96px.

In the 1-color mode LSCM images the decaline droplets were slightly darker than the particles. For localizing them an upper intensity threshold was chosen, neglecting each pixel in the LSCM image with higher intensities than the threshold. In the resulting LSCM image only the cis-decaline droplets were visible and could easily be localized (see Sec.5.1.2). The trajectories of three droplets could be followed over the whole shear measurement. As the measurement was performed with the 1-color mode LSCM, possible deformations of the droplet shape could not be resolved as the contrast between particles and droplets at the contact was too low. The droplets are hence visualized as spheres instead.

8.1.2 Global Cluster Motion

During the shear the coarse cluster shape was nearly unchanged and the cluster was not torn apart. As the cluster was attached to the bottom cover slide, a linear elongation along the x-axis, when moving the indenter in negative x-direction, was expected (see Sec.2.3.1). Against this expectation a reorganization with an elongation along the y-axis was observed (Fig.8.2). The cluster motion hence was inhomogeneous and non-linear, meaning that the cluster was not following the direction of the applied shear load. The question is, what was the origin of this non-linear cluster motion?

This motion could be caused by a hydrodynamic force acting on the cluster while shearing. But as the hydrodynamic flow created by a shear plate displacement of 0.25µm could not be large and fast enough for moving the particles (see Sec.4.2.2) this could not be responsible for the cluster motion.

8.1.3 Energy Interplay

This non-linear cluster motion and the internal cluster reorganization was caused by an interplay of two energies: The binding energies of the particles at the liquid-liquid interface and the deformation energy, which is stored in the droplets (see Sec.4.2.2). In general during the shear the droplet volume is conserved. A deformation of the droplet thus leads to a change in the liquid's surface. The required energy for increasing the droplet surface could be stored as deformation energy in the droplet. The droplet with its surrounding particles is then in a distorted configuration. This configuration and also the local structure can hinder the relaxation of the droplets surface. During further deformation, the particle-droplet configuration could get unstable and the droplet is relaxing. The stored deformation energy is then released on a very short time scale. This process is too fast to be captured with the used LSCM. The released energy can then be converted into kinetic energy of the silica particles at the liquid-liquid interface. The occurrence of this process can be recognized by large structural changes and particle displacements, which cannot be tracked anymore between two consecutive measurements.

In case of this kinetic energy being larger than the binding energy, particles could be released from the liquid-liquid interface. Otherwise particles are able to migrate on the

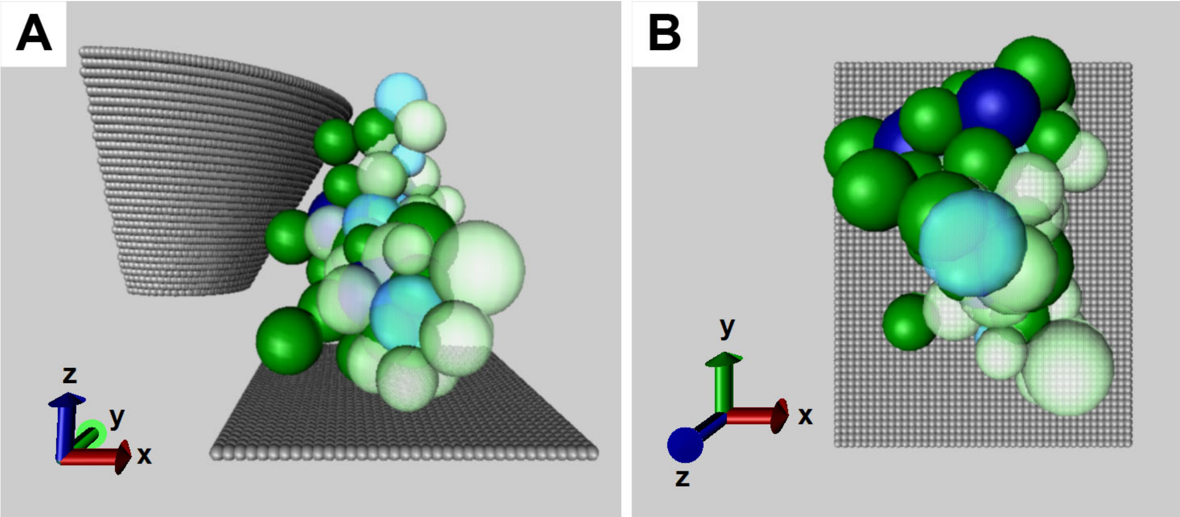

Figure 8.2: 3D reconstruction of the particle configuration of the wet cluster before the first and after the last shear step. The particles are indicated with green, the cis-decaline droplets in blue. Particles and droplets at the beginning of the shear are shaded translucent, particles and droplets after the last shear step in opaque

droplet's surface causing a structural reorganization of the local particle-droplet structure. In both cases additionally the released deformation energy can build up a laminar flow in the surrounding of the droplet. The hydrodynamic force caused by this flow can then move free unbound silica particles (see Sec.2.2.4). Additionally particles in contact with particles bound at the liquid-liquid interface could be dragged with the droplet deformation, which can change the particle structure in the local environment drastically.

In the following by means of a few exemplary structural changes the above explained effects were illustrated.

8.1.4 Local Cluster Motion and Single Particle Dynamics

In the case of the explored cluster, no breakage of the cluster and no release of particles from the liquid-liquid interface was observed. This is a hint that the released deformation energy was smaller than the binding energy of the particles. The silica particles were only able to migrate on the droplet surface (Fig.8.3).
After the first shear step with a shear displacement of 0.25µm the released deformation energy was rather small and led in average to particle displacements smaller than one particle diameter. The particle displacements were hence small enough for following the particle motion between the initial configuration and the first shear step. During this shear step, the cluster was not following the applied shear direction and was deformed inhomogeneously (Fig.8.4). In the cluster a torsion with particle translations clockwise around the z-axis occurred. The detailed origin of this torsion was not yet clear, but could be due to a symmetry breaking between the cluster and the indenter. As the

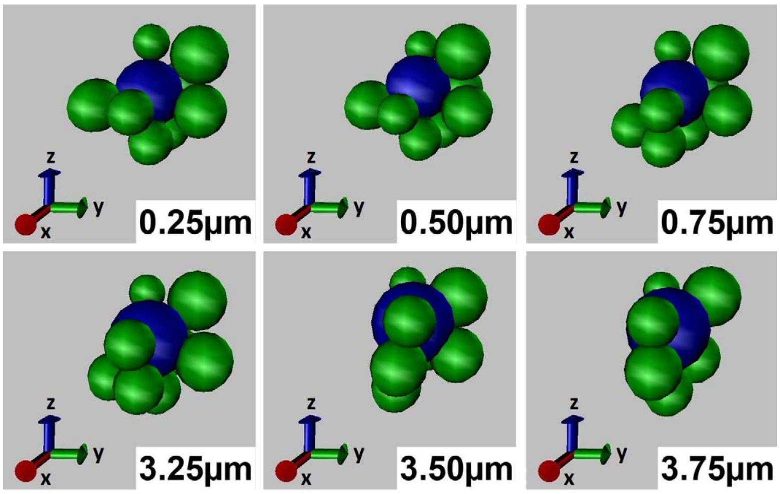

Figure 8.3: 3D reconstruction of the lowest cluster droplet with its local environment at different shear displacements. The droplet had a diameter of roughly $R_d = 8.5\mu m$ and initial z-position at $z = 10.59\mu m$. During the shear the silica particles were migrating on the droplet surface

contact point of the cluster with the indenter was not lying on the symmetry axis of the indenter, the shear displacement could generate a torque on the cluster, which caused the torsion.

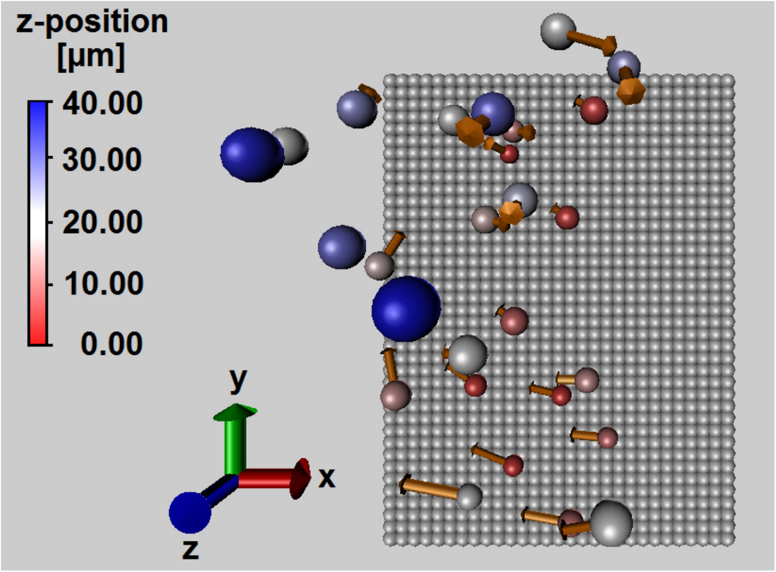

Figure 8.4: 3D reconstruction of the initial particle configuration and their translation during the first shear step. The particles are color coded concerning their height in the sample (z-position). The translation is visualized with orange vectors. The different size of the particles is due to the projection along the z-axis in the 3D reconstruction

After the second shear step (shear displacement of 0.50µm) in the bottom part of the cluster at low z-positions and in the top part at z-positions larger than 20µm a few particles displacements started to increase (Fig.8.5). Although the applied shear displacement was kept constant, the particle displacements became now larger than one diameter and the particle trajectories were no longer traceable. This shows that the cluster deformation and hence the released energy after droplet relaxation was increased.

The droplet deformation and relaxation not only affected the silica particle motion, but also the translation of the droplets itself. Due to undirected particle motions and the cluster reorganization the droplets were dragged in different directions during the whole shear process leading to random-walk-like droplet trajectories (Fig.8.6).

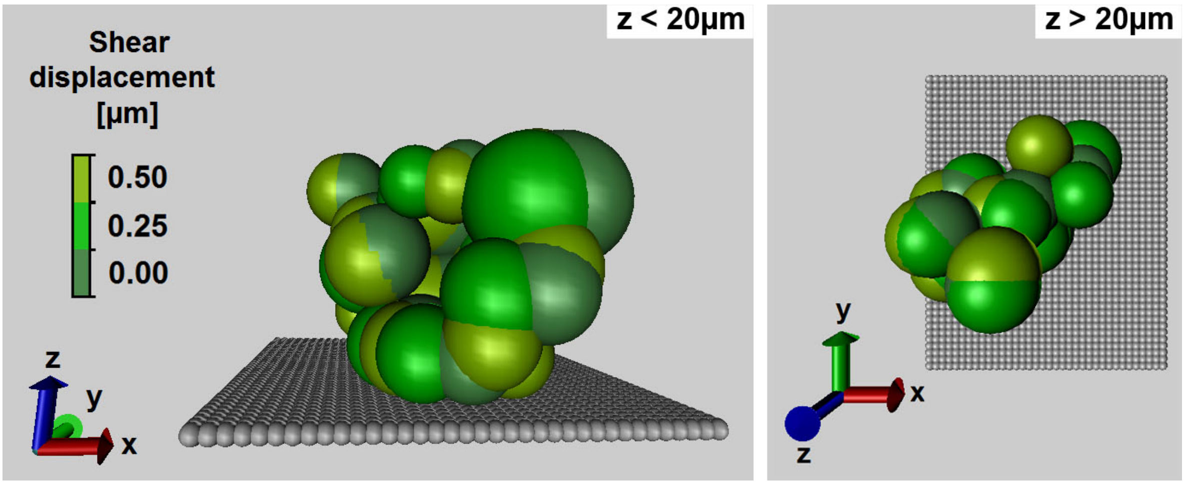

Figure 8.5: 3D reconstruction of the initial particle configuration and after the first and second shear step, side view at low z-positions (A) and top view at high z-positions (B). A few of the particle displacements were too large to follow trajectories

In total this system shows a complex dynamic behavior when sheared. Different interactions between the particles and droplets contributed to the particle-droplet motion. The main influence was originated by the droplet deformation during shear. As the droplet relaxation was not directed with shear, the released deformation energy led to undirected particle displacements. The resulting inhomogeneous cluster reorganization affected then also the droplet trajectories, which were random-walk-like.

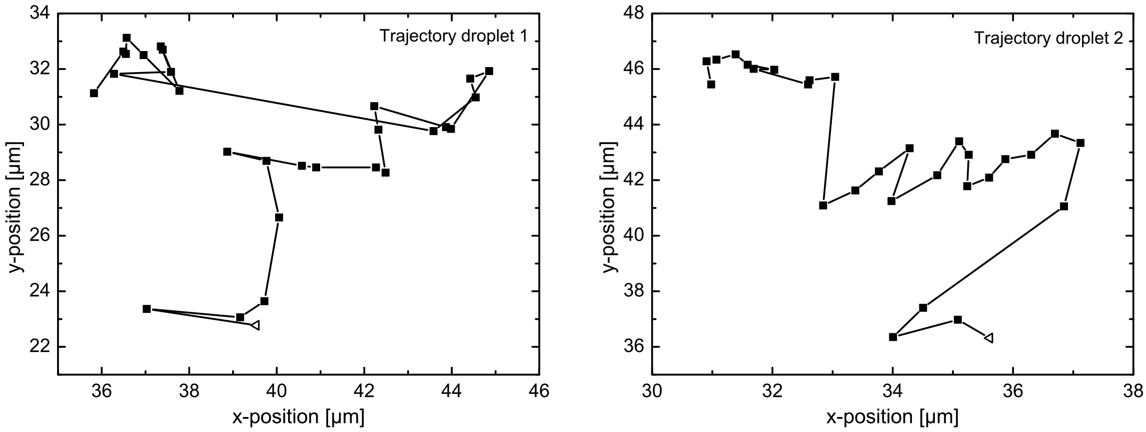

Figure 8.6: Trajectories in the x-y-plane of the two lowest droplets in the cluster. Droplet one was situated at a initial z-position of $z = 10.59\mu\text{m}$, droplet two at $z = 17.22\mu\text{m}$. The droplet trajectories are comparable with a random walk

8.2 Compression of a Wet Bulk Granulate

In the previous section the wet cluster was measured with the 1-color mode LSCM. Hence possible deformations of the droplet shape due to attached silica particles could not be resolved. The droplet appeared here as spheres. In the following measurement the 2-color mode was used. Droplet deformations could now be visualized and described quantitatively. The influence of the droplet deformation on the local structure of a bulk system during compression was now investigated.

8.2.1 Measurement Procedure

A loose wet granulate bulk system was investigated (Fig.8.7). Just as in the case of the cluster sample the bulk sample consisted of 50mg/ml of HMDS-modified particles suspended in a mixture of 85vol% NaSCN-solution (refractive index $n = 1.444$) and 15vol% cis-decaline. As the sample was measured with the 2-color mode LSCM, the cis-decaline was labeled differently with the fluorescent dye Coumarin 6 (see Sec.3.1.2). The bulk granulate was imaged in an observation volume of 100µm×100µm×41.7µm with a resolution of 512px×512px×96px. The sample was compressed stepwise in 2µm steps with a total compression displacement of 12µm. For the compression the indenter tip with a surface tip diameter of 200µm was used. At the beginning of the compression an indenter tip surface was at the upper boundary of the observation volume, i.e. at a height of 41.7µm.

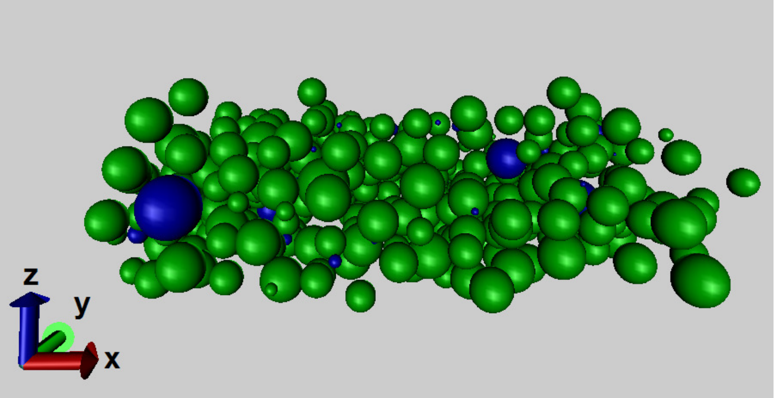

Figure 8.7: 3D reconstruction of the initial particle configuration of the wet loose bulk system. The particles are indicated with green, the cis-decaline droplets in blue

8.2.2 Droplet Shape Analysis

The actual sample was measured with the 2-color mode LSCM. Hence possible deformations of the droplet and deviations from a spherical shape due to silica particles were resolvable. The positioning algorithm (see Sec.5.1.2) used up to now failed for non-spherical objects. The droplets were positioned and analyzed with an modified watershed algorithm instead [118]. This watershed positioning was done by Laurent Gilson (Institut für Mikroverfahrenstechnik und Partikeltechnologie, Umweltcampus Trier-Birkenfeld, Birkenfeld). First the raw LSCM images (Fig.8.8A) were binarized, i.e. pixels above

Figure 8.8: Cis-decaline droplet as raw (A) and binarized image (B) and as 3D visualization with VMD (C) and Surface Evolver (D). In the VMD visualization the droplet shape is reconstructed with small spheres. With Surface Evolver the contact of the silica particles with the droplet surface could be visualized

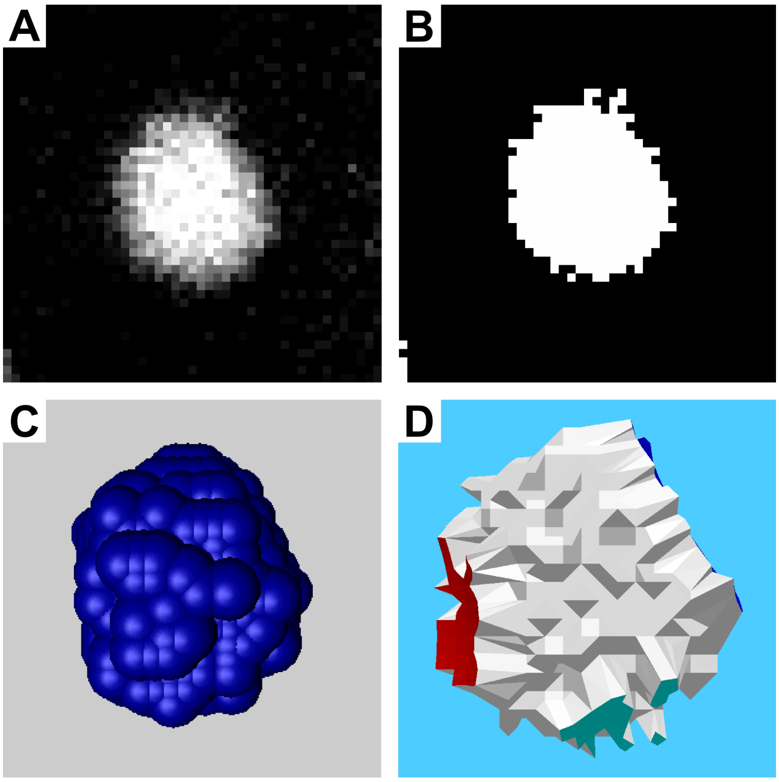

a certain intensity threshold were counted as part of the droplet and imaged in white (Fig.8.8B). From the binarized images the watershed analysis determined all pixels being part of the droplet. With this the droplet shape and surface could be calculated. The watershed analysis provided the center of mass coordinates of the droplets, their volume and the droplet extensions along the x-, y- and z-axis. Once all pixels belonging to the droplet were determined, the droplet shape and surface could be reconstructed in 3D. The droplet shape could be then visualized in 3D with VMD (Fig.8.8C). The droplet shape is reconstructed with small spheres. A further 3D reconstruction of the droplet shape and surface could be done with the program “Surface Evolver”, where the contacts of silica particles with the droplet surface were shown (Fig.8.8D).

To describe the droplet deformation quantitatively, two new parameters were defined: The polar and the azimuth eccentricity (see Sec.10.6). For that, it was assumed that the droplets have an ellipsoidal shape. The eccentricity in general describes the deviation of the droplet shape from being spherical. The polar eccentricity e_{pol} hence describes this deviation along the polar axis and the azimuth eccentricity e_{azi} in the azimuth plane respectively.

8.2.3 Structure Analysis

The initial structure of the wet bulk granulate was quite loose with a starting averaged particle volume fraction of $\phi_{ave} = 0.256 \pm 0.012$ (Fig.8.9). This volume fraction was

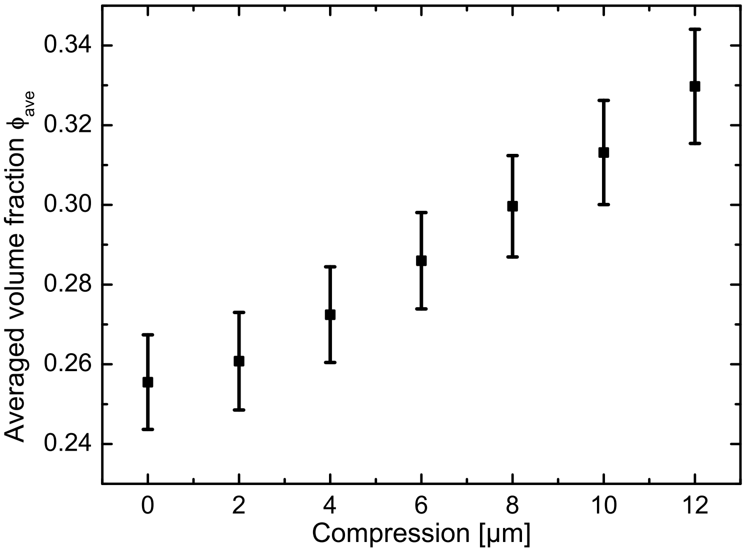

Figure 8.9: Averaged particle volume fraction ϕ_{ave} of the wet loose bulk granulate system. The initial particle volume fraction here was comparable to the one of dry system without an additional binder liquid

comparable to that of a dry suspension, i.e. a suspension of HMDS-modified particles in NaSCN-solution without an additional binder liquid (see Sec.10.2). Therewith the additional capillary interaction had no influence on the the static structure, i.e. the starting particle configuration in the bulk. The initial averaged volume fraction was hence dominated by the interaction of the silica particles.
During the compression a global compaction of the bulk granulate was observed, as the averaged particle volume fraction increased continuously. In Sec.8.1.3 it was shown that the local structure and dynamics were dominated by the deformation and relaxation of the droplets' shape. Accordingly a different behavior of the local volume distribution during compression will be expected compared to the compression of a sediment in a dry cohesive model system (see Sec.6.2.2).

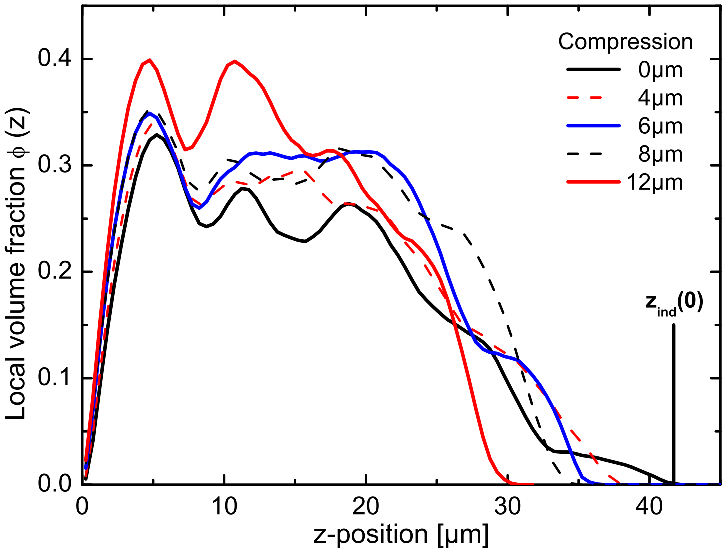

Figure 8.10: Local volume fraction distribution $\phi_{local}(z)$ of the wet granulate systems for different compression steps

Experimentally this different behavior was observed, as seen in the local volume fraction distribution $\phi_{local}(z)$ (Fig.8.10). In the lowest layer ($z < 8\mu$m) ϕ_{local} increased as expected with ongoing compression, in the second layer between 8µm and 15µm in height the local volume fraction was varying strongly. In the upper part ($z > 23\mu$m) near the indenter tip surface a decrease of ϕ_{local} was expected as here the particles are pushed downwards. Nevertheless also here strong variations in the local volume fraction distribution were observed. The structural changes during compression were obviously due to an additional capillary attraction in the system. The energy interplay between the droplet deformation energy and the binding energy of the particles at the droplets surface has to be taken into account to fully describe the reorganizations.

In the following a few examples of local structural changes and reorganizations are shown. The structural changes are related quantitatively with the droplet deformation, i.e. with the eccentricities of the droplet. Further phenomena caused by the droplet deformation and relaxation, such as the release of particles from the liquid-liquid surface are also discussed in respect to the droplet eccentricities.

8.2.4 Dynamics Analysis

Local structural changes due to droplet deformation

Large structural reorganization predominantly occurred in the local environment of cis-decaline droplets. Fig.8.11 shows a part of the bulk granulate above z-positions of 20µm before and after a compression displacement of 8µm (compression step four). The structure before the compression step is shaded in light colors, particles and droplets afterwards in dark colors. There were two characteristic regions, where the environment around the droplet has been locally diluted after the compression step. The droplet and its neighboring particles in region 1 disappeared, i.e. their displacement was significantly larger then the applied compression step and they were probably squeezed out of the observation volume. In region 2 the droplet, its shape and the contacting neighbors

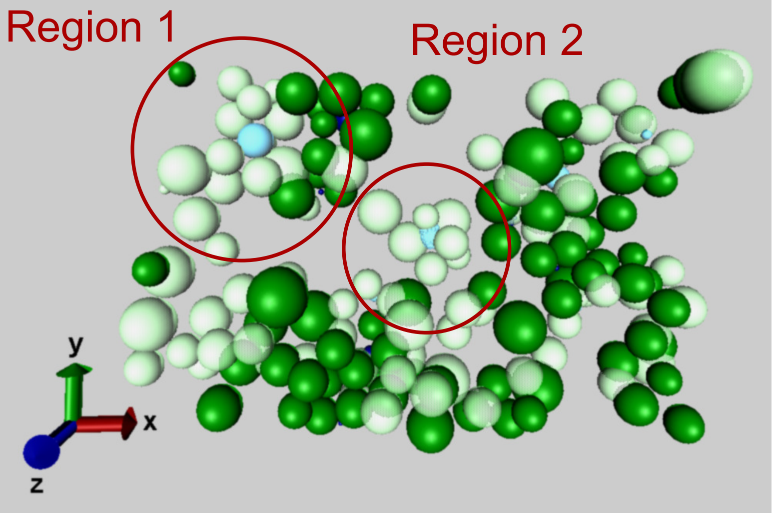

Figure 8.11: Part of the bulk granulate structure before and after the fourth compression step. Particles are colored in green, droplets in blue. Particles and droplets before the compression step are shaded in light colors, particles afterwards in dark colors

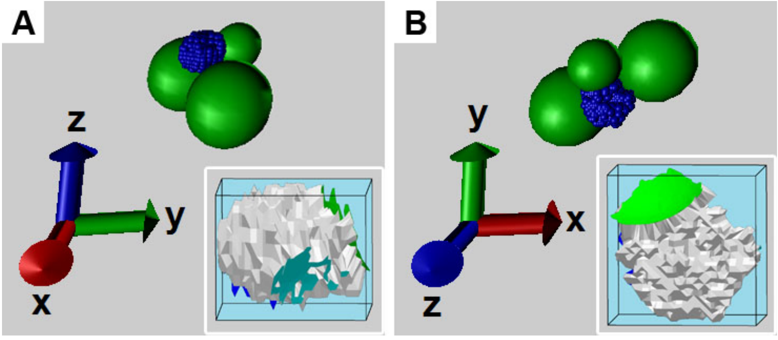

Figure 8.12: 3D reconstruction of droplet and its local environment before compression step four. The inlets show the visualization with Surface Evolver

were visualized (Fig.8.12). At the beginning before compression step four this droplet had three contacting particles. The droplet eccentricities were $e_{pol} = -0.306$ and $e_{azi} = 0.192$, which showed that the droplet was strongly deformed. After the compression step four, which corresponded to a total compression displacement of 8µm this droplet and its local particle environment disappeared. Obviously the relaxation of the droplet shape after deformation led to a laminar flow, which dragged the particle-droplet configuration away. Nevertheless an estimation about the possible trajectories could be made, as there were two droplets in the neighborhood after the compression with comparable volume (Fig.8.13). In both cases of the possible droplet trajectories the number of contacting particles at the droplet surface was unchanged (Fig.8.14). The change in the polar eccentricity is for both possible droplet trajectories large and in the order of $\Delta e_{pol} \approx 0.450$, while the azimuth eccentricity was nearly unchanged. This droplet deformation corresponded to a deformation energy of $E_{deform} \approx 0.20 \cdot 10^7 \mathrm{k_B T}$ for D1. For droplet trajectory D2 a deformation energy of roughly $E_{deform} \approx -4.96 \cdot 10^7 \mathrm{k_B T}$

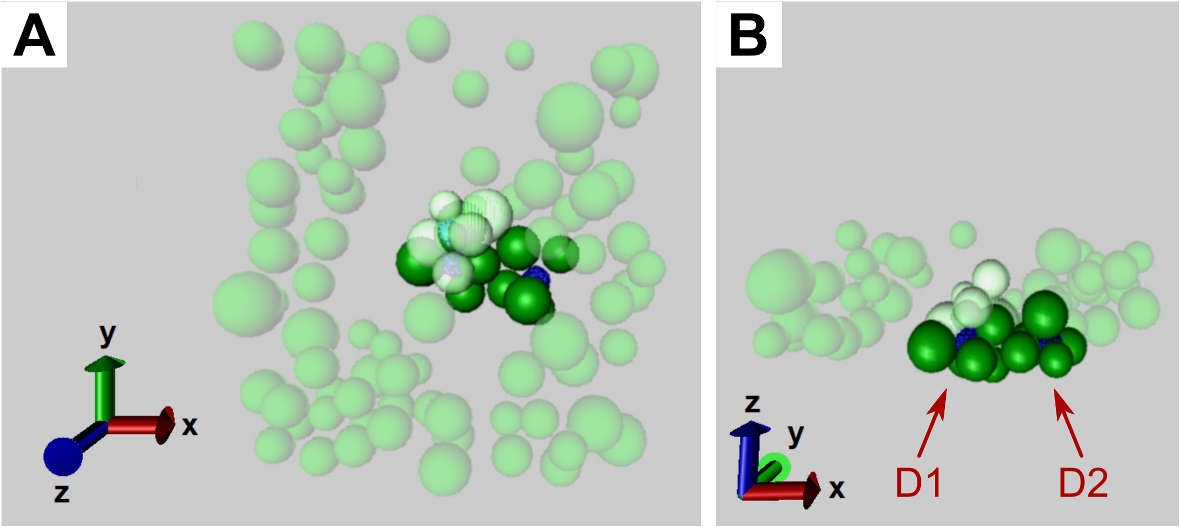

Figure 8.13: Part of the bulk granular structure in region 2 before and after the compression step four, top view (A) and front view (B). Particles and droplets before step four are shaded in light transparent. The droplets and their local particles environment after step four are opaque, particles in the surrounding are shaded dark transparent

was obtained (see Tab.10.5 in Sec.10.6). As the gain in energy after relaxation for droplet trajectory D2 was positive, this trajectory should be favored. Nevertheless this deformation energy was not able to release silica particles from the droplet surface. Instead a structural reorganization of the local droplet environment due to a laminar flow was observed.

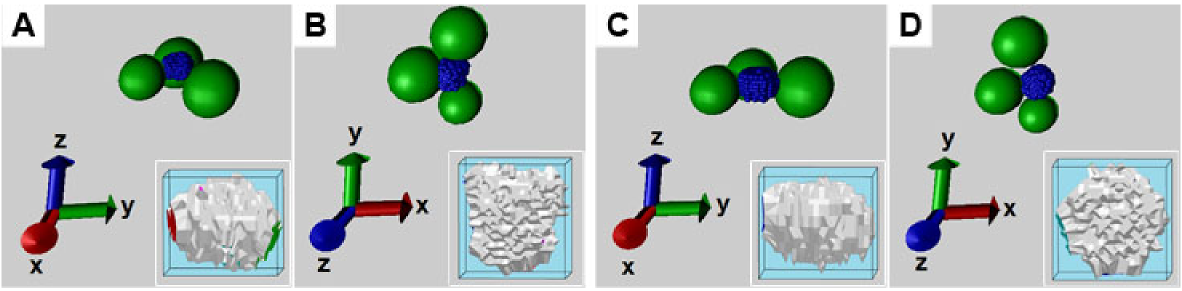

Figure 8.14: 3D reconstruction of droplet D1 and D2 its local environment after compression step four. The droplet orientation is visualized concerning their eccentricities, the polar eccentricity e_{pol} droplet D1 (A) and its azimuth eccentricity e_{azi} (B) and for droplet D2 respectively (C) and (D)

Particle release from the droplet surface

Droplets with a large volume and large extensions provide hence large surface areas. Small deformations lead already to deformation energies which exceed the binding energy of the silica particles at the liquid-liquid interface. Fig.8.15 shows the 3D reconstructions of a droplet, which was situated at the bottom of the sample and had a larger volume compared to the one discussed before. As it was sticked to the cover slide, the trajectory over the entire compression process was traceable. The large size and the high volume of this droplet, led to large changes in the surface and hence to large deformation energies, although the eccentricities were almost unchanged during compression (Fig.8.16 and see Tab.10.6). Particles at the surface gained enough kinetic energy for leaving the droplet surface, e.g. between a compression displacement of 6µm and 8µm (Fig.8.15). Additional due to the compression particles were pushed downwards. Once they came in contact with the droplet surface, they got bound to it (see compression displacement 6µm and 12µm).

For small droplets the deformation energy was not large enough to release silica particles from the droplet surface. Nevertheless large changes in the droplet shape and hence the eccentricities led to laminar flows around the droplet, dragging away the particle-droplet configuration and leading to locally diluted regions in the bulk system. For larger droplet volumes and depending on the deformation, the change in droplet surface could get that large that the deformation energy exceeded the binding energy of the silica particles at the droplet surface. The deformation energy was then converted into kinetic energy and particles were released from the liquid-liquid interface.

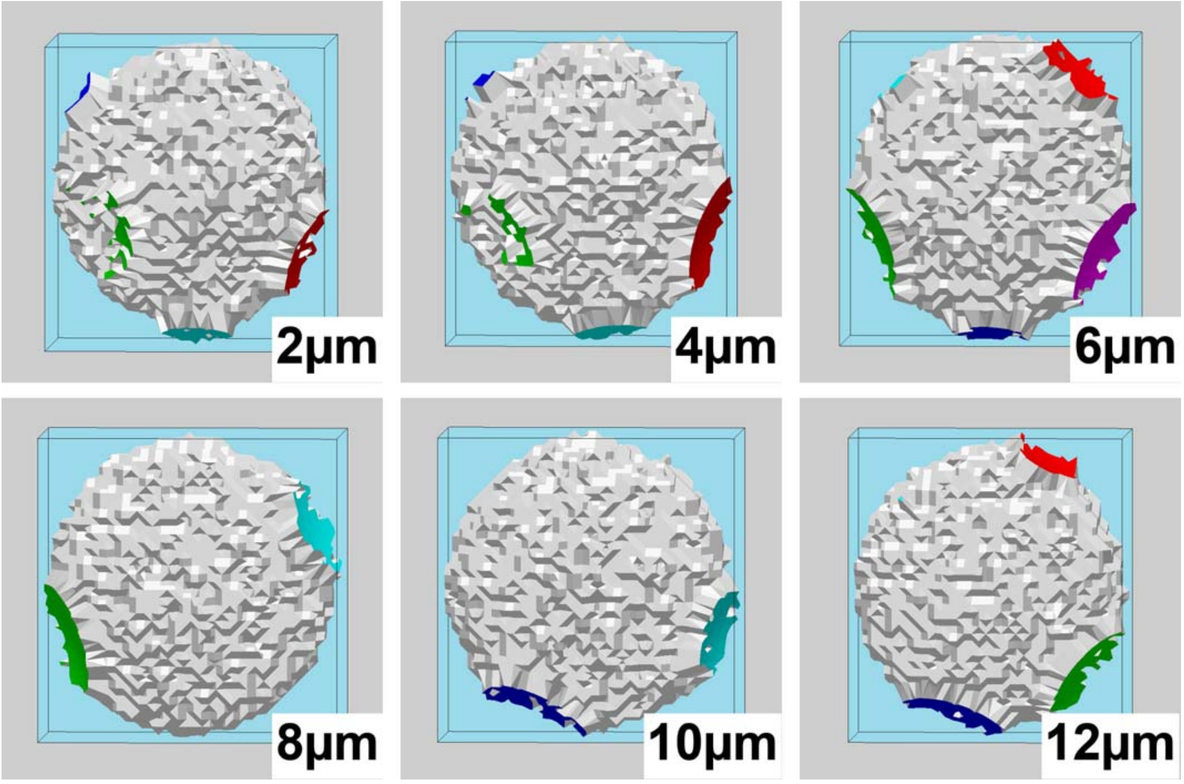

Figure 8.15: 3D reconstruction of a droplet situated at the cover slide. The trajectory was traceable over the entire compression process. Due to the high deformation energy, a release of silica particles from the droplet surface was possible and the number of contacting particles was varying

8.3 Conclusion and Outlook

Conclusion

A wet granulate model system was investigated. It consisted of a silica particle suspension with nearly hard sphere interaction and an additional binding liquid. This binding liquid created an additional attraction over capillary interaction. The binder liquid was inhomogeneously distributed, leading to a Pickering emulsion-like structure.

Two different structures were explored. One was a compact wet cluster under shear, consisting of five binder liquid droplets with roughly thirty silica particles. The second structure was a loose bulk granulate, where a compression load was applied. In both systems large structural reorganizations with typical particle displacements larger than one diameter were observed. The main particle displacement directions were inhomogeneously distributed and generally not directed along the applied load. This was in contrast to the up to now observed structural changes under compression and shear in dry cohesive model systems. In these systems the particles were traceable with averaged particle displacements below one particle diameter and had a preferred displacement direction caused by the applied load.

Figure 8.16: Polar and azimuth eccentricities for the droplet situated at the cover slide. During the compression the droplet shape and hence the eccentricities were varying only slightly

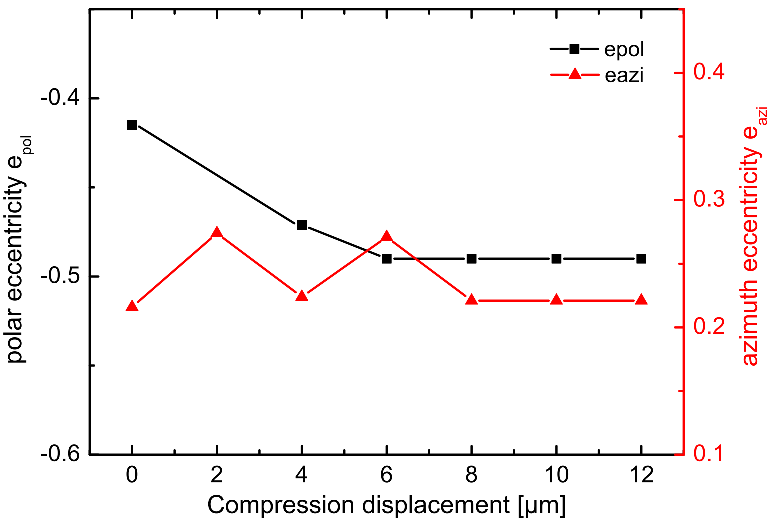

The large structural changes in the wet granulate models system were caused by an energy interplay of the two dominant energies in this system; the binding energy of the silica particles at the liquid-liquid interface and the deformation energy of the binding liquid droplets. A deformation of the droplets when applying a load led to a change in the droplet surface. For increasing the surface the required surface energy was stored in the droplet as deformation energy. When reaching a certain load, the stored energy was released. This energy was either converted into kinetic energy of the silica particles at the droplet surface or a laminar flow was built up leading to large structural changes in the local environment. With the obtained kinetic energy the silica particles were either able to migrate on the droplet surface or, when the binding energy was exceeded, the particles were released from the surface. All these three phenomena were observed in the investigated wet granulate system.

These investigations showed that in systems with an inhomogeneously distributed binder liquid, e.g. Pickering emulsions complex and anisotropic structural changes occur, when mechanical load is applied. The relationship between macroscopic parameters, e.g. averaged volume fraction, and microscopic particle behavior, e.g. single particle motion, is here hardly possible. For predicting the bulk behavior once the single particle dynamics are known and vice versa, further investigations on a single particle level of these systems are required.

Outlook

As the dynamics during droplet deformation and relaxation are to fast for visualizing with the LSCM setup used here, further 3D imaging techniques are needed. A new setup for fast confocal microscopy was developed in this group [119]. In combination with a slow continuous shear or compression the fast dynamics of the droplet deformation might be captured and following the droplet trajectories might be possible. As the deformation energy not only depended on the droplet deformation, i.e. the eccentricities but also on the droplet volume, further parameters describing the deformation process have to be developed. Improvements of the watershed algorithm can lead to more precise determinations of the droplets surface and hence of the deformation energy.

9 Conclusion

A combination of confocal microscopy for 3D imaging with nanoindentation was used to investigate model granular systems in the wet and dry state under a mechanical load. The model systems consisted of polydisperse fluorescent silica particles with various particle interactions. The focus was on the relationship between the global macroscopic behavior and the single particle dynamics. A novel technique was developed for measuring the rotation of micrometer sized spherical particles in 3D with all rotation angles. The particles were marked with an optical anisotropy by photobleaching parts of the fluorescent dye. In compression and shear experiments the structural changes in the bulk and their influence on the rotation and translation of polydisperse silica particles were studied.

Globally a compaction of a sediment of cohesive particles under compression was observed. On a local scale during the initial compression steps the compaction predominantly occurred in the lower part of the sediment. The particle motion strongly depended on the local structure of the sediment. Particles located in locally dense regions showed a less pronounced translational and rotational motion. In regions, where mainly the structural changes happened, the particles showed a significant rotation before the onset of a translational motion.

In shear experiments on a global bulk scale the explored samples showed the shear behavior, which was expected from classical shear experiments as with the Jenike cell. A local diluted region near the upper shear plate enhanced the onset of the shear flow and shear zone formation. During the shear a rearrangement of particles along the sample height was observed. This was a mixing between lower lying particle layers. This exchange of particles occurred also between the flowing (shear zone) and the non-flowing region. This interlayer mixing was hence a global behavior of the examined granulate systems.

Further, a wet granulate model system was investigated. An additional binding liquid created an attraction over capillary interaction. The binder liquid was inhomogeneously distributed, leading to a Pickering emulsion-like structure. Large structural reorganizations with typical particle displacements larger than one particle diameter were observed. The main particle displacement directions were inhomogeneously distributed and generally not directed along the applied load. The binding liquid dominated the particle and the droplet dynamics, when a mechanical load was applied on the system.

Global parameters as the averaged volume fraction are not sufficient to describe fully the behavior of granulates under shear and compression. For dynamical processes also the single particle motions have to be considered for understanding the complex structural changes in dense granular systems under mechanical loads.

10 Appendix

10.1 Particle Properties

Properties of particles as purchased from supplier

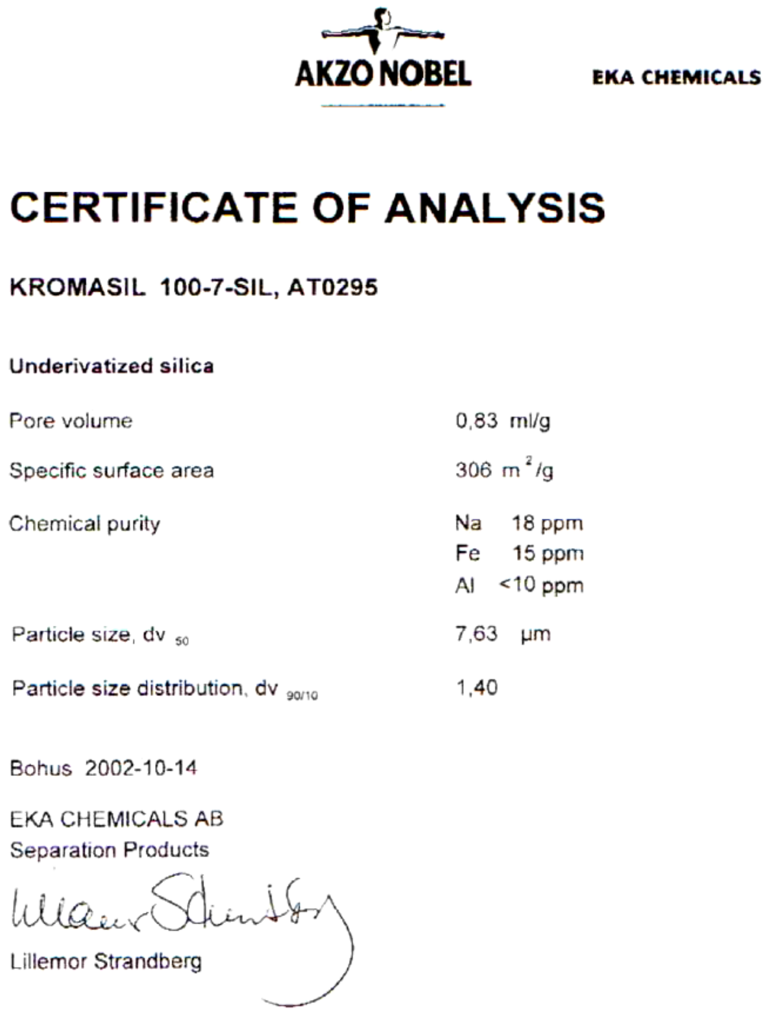

AKZO NOBEL

EKA CHEMICALS

CERTIFICATE OF ANALYSIS

KROMASIL 100-7-SIL, AT0295

Underivatized silica

Pore volume	0,83 ml/g
Specific surface area	306 m^2/g
Chemical purity	Na 18 ppm Fe 15 ppm Al <10 ppm
Particle size, dv_{50}	7,63 µm
Particle size distribution, $dv_{90/10}$	1,40

Bohus 2002-10-14

EKA CHEMICALS AB
Separation Products

Lillemor Strandberg

Figure 10.1: Particle properties of the silica particles as purchased from the supplier

Particle properties - Overview

The particle properties, i.e. diameters and refractive indices of the particles at different stages of synthesis and surface modification were measured optically by SEM images and with refractometry, respectively (see also Sec.4.1.1 and Sec.4.1.2).

particles	diameter [µm]	refractive index
as purchased	7.39 ± 0.69	-
fluorescently labeled	7.54 ± 1.20	1.443 ± 0.003
DMOAP-modified	-	1.470 ± 0.003
HMDS-modified	-	1.443 ± 0.003

Table 10.1: Particle diameters and refractive indices for the different particle fractions

10.2 Sediment Preparation

Volume fraction of the undisturbed sediment

As all used sample systems in this work were dominated by gravitation, the particles were directly sedimenting to the bottom cover slide after sample preparation. The undisturbed sediments, i.e. not exposed to an external load, were imaged in 3D for three different sample heights. The particle local volume fractions (see Sec.5.2.2) were calculated and averaged to obtain an averaged volume fraction. Depending on the particle interactions, different volume fractions of the sediments were observed. The

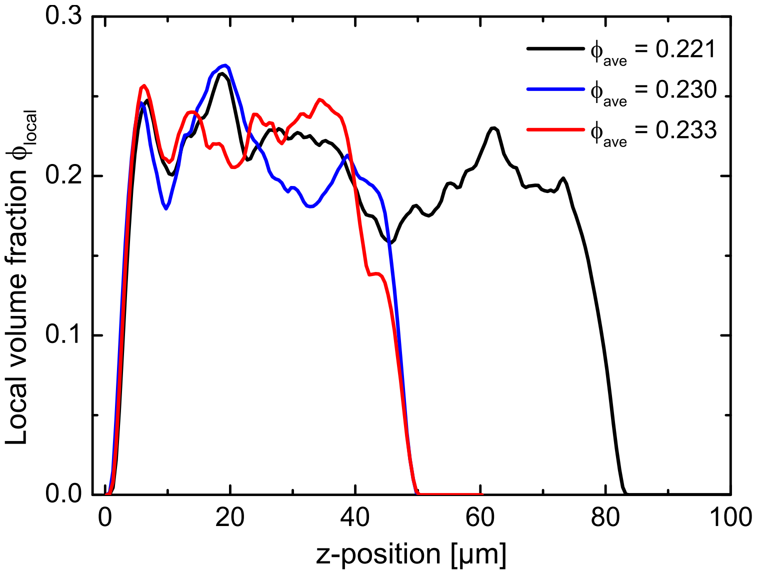

Figure 10.2: Local volume fraction distribution and averaged volume fraction of the reference systems for three different sample heights

averaged volume fraction for the dry hard-sphere like model system (reference system) was 0.228 ± 0.005 (Fig.10.2). In the dry cohesive model system (Fig.10.3, left) with $\phi_{ave} = 0.332 \pm 0.016$ the averaged volume fraction was slightly higher than for the dry hard-sphere like system. To visualize the influence of the particle interaction on the sediments volume fraction in the wet model system, only the HMDS modified particles in a NaSCN-solution without an additional binder liquid were measured (Fig.10.3, right). The obtained averaged volume fraction was $\phi_{ave} = 0.249 \pm 0.006$, which was comparable to the dry hard-sphere like model system.

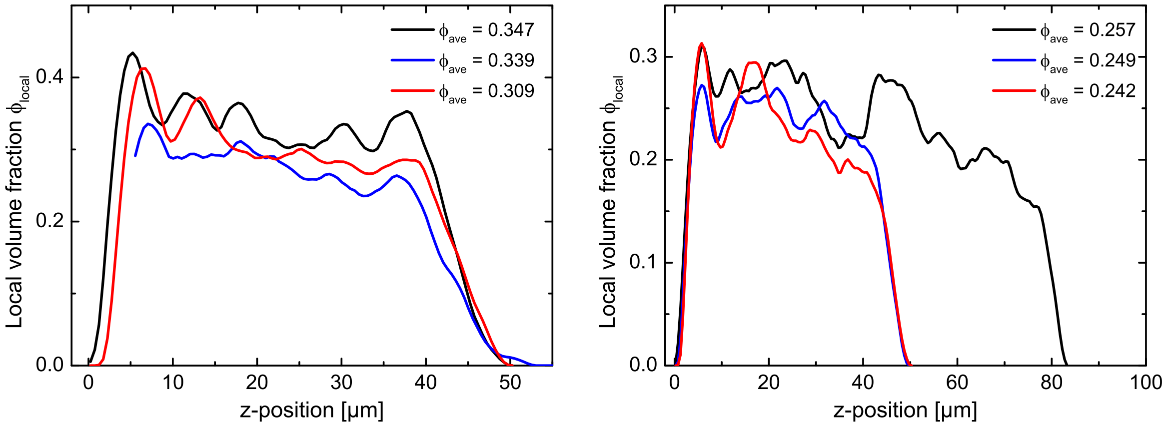

Figure 10.3: Local volume fraction distribution and averaged volume fraction of of the dry cohesive (left) and the wet granulate model system (right) for three different sample heights

10.3 Data Analysis

Determination of the positioning accuracy

For determing the positioning accuracy a static structure was images ten times in consecutive 3D images. The imaged volume had a size of 100µm×100µm×25µm. Particle positions and diameters were determined as described in Sec.5.1.2. Afterwards for all particles over the entire 3D image series the trajectories were calculated (see Sec.5.3.1). Between 307 and 313 particles were localized per 3D image, in total for 299 particles the trajectory was obtained. Each trajectory contained now ten sets of particle coordinates in x-, y- and z-direction and the diameter for one single particle. These coordinates and diameters were now averaged for each particle.

The positioning accuracy of the localization algorithm is the averaged standard deviation for each coordinate. Positions were obtained with an accuracy of 135nm in x- and y-direction and 248nm in z-direction. Diameters had an accuracy of 41nm.

10.4 Calculation of Particle Interactions

Material constants

	refractive index n	dielectric constant ε	ionization frequency ν_i [10^{15}Hz]	density ϱ [g/cm^3]
silica (am)	1.443^a	3.82^b	3.2^b	2.00
NaSCN-H_2O	1.443^a	2.08^c	-	1.25^a
cis-decaline	1.479^a	2.50^d	2.8^e	0.87^a
octadecane	1.434^f	2.08^g	2.9^e	-

Table 10.2: Material constants of the used materials for the calculation of the interaction constants. a) own in-house performed measurements, b) after reference [44], c) with the assumption $\varepsilon = n^2$, d) after reference [120], e) estimated from values for different solvents from reference [44], f) after reference [121], g) extrapolated from dielectric constants of several alkanes

Figure 10.4: Dielectric constants of alkanes (after [120]) versus the number of carbon atoms of the alkanes. For obtaining the dielectric constant of octadecane the values were extrapolated with an exponential growth function

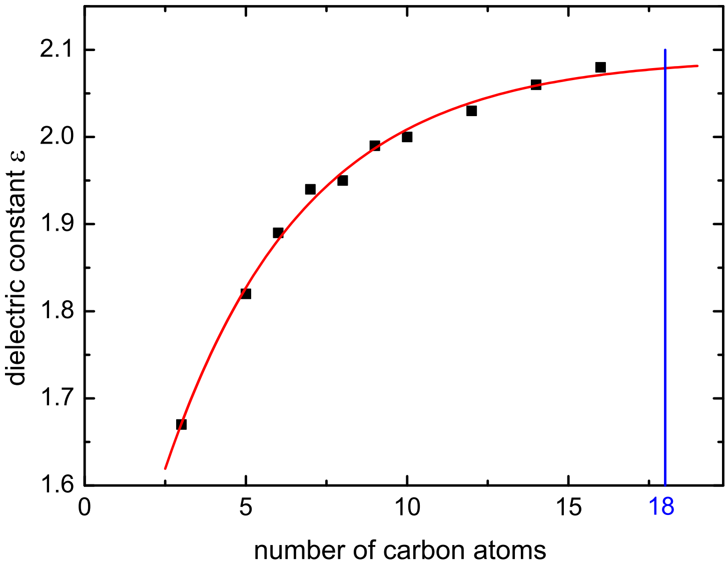

The dielectric constant for octadecane was extrapolated from the dielectric constants of several alkanes [120]. The values were fitted with an exponential function $f(x) = a \cdot \exp(-x/n) + b$ with $a = -0.84344$, $n = 4.31845$ and $b = 2.09196$ (Fig.10.4). The obtained value for the dielectric constant for octadecane was $\varepsilon = 2.08$.

Calculation of the DMOAP-film thickness

The thickness of the DMOAP layer on silica in cis-decaline depended on the diameter of the collapsed alkyl chains. The diameter was calculated with the radius of gyration.

$$R_{gyr}^2 = \frac{1}{6} N l^2 \tag{10.1}$$

with l being the length of a chain segment and N the number of segments. For an alkyl chain l was assumed to be the bond length between two carbon atoms with $l = 154\text{pm}$ [76] and $N = 18$. As a radius of gyration for the alkyl chain ball one obtains $R_{gyr} = 267\text{pm}$. Taking the N-O bond with a length of 121pm [122] and other bonds into account, a layer thickness of roughly 400pm of the DMOAP film was obtained.

Calculation of the size of a cis-decaline molecule

For the maximum and the minimum extension of a cis-decaline molecule it was assumed that the cyclohexane rings are lying in one plane. The maximum extension D_{max} is then the width of the two rings. With the C-C bond length of 154pm and an angle of 120° between two bonds one obtains $D_{max} \approx 580\text{pm}$. Here the size of an carbon atom with roughly 50pm in diameter was additionally taken into account. The minimum extension D_{min} was the radius of a carbon and a hydrogen atom and the bond length of 109pm between them [76]. It was calculated to $D_{min} \approx 160\text{pm}$.

Calculation of Hamaker constants

The Hamaker constants A_H for the different systems were calculated at room temperature with $T = 295\text{K}$ with Eq.2.8 (Tab.10.3). For the ionization frequency in Eq.2.8 the ionization frequencies of the intermediary solvent were used. Further parameters were obtained from Tab.10.2. The interaction energy E_{VdW} with separation distances D between two identical spheres with radius $R_p = 3.77\mu\text{m}$ was calculated using Eq.2.7.

material A	material I	material B	A_H [10^{-22}J]	D [pm]	E_{VdW} [k_BT]
silica	cis-decaline	silica	4.36	800	-42.09
silica	octadecane	silica	2.96	800	-28.53
octadecane	cis-decaline	octadecane	6.32	160	-304.93
octadecane	cis-decaline	octadecane	6.32	580	-84.12
silica	NaSCN-solution	silica	2.66	560	-36.60

Table 10.3: Hamaker constants and interaction energies for different systems

Calculation of the Debye length for an aqueous NaSCN-solution

For the calculation of the inverse Debye length κ for the aqueous NaSCN-solution Eq.2.15 was used. It was assumed that due to the high salt concentration in the NaSCN-solution no dissociation of charges at the silica surface occurred. For obtaining an refractive index of $n = 1.445$ of the NaSCN-solution roughly 1g of NaSCN had to be dissolved in 1.15ml water. This corresponded to a particle number density of $6.014 \cdot 10^{27}\mathrm{m}^{-3}$. The valency of the NaSCN ions was one. With the parameter from Tab.10.2 an inverse Debye length of $\kappa = 4.51 \cdot 10^{10}\mathrm{m}^{-1}$ was obtained, corresponding to a Debye length of 22pm. This was much smaller than the diameter of a hydrogen atom [76].

Calculation of Peclet numbers

The Peclet numbers for the reference system (see Sec.4.2) and the dry cohesive model system (see Sec.4.2.1) were calculated using Eq.2.42. The silica particles in the wet granulate model system were dispersed in the NaSCN-solution. For freely sedimenting particles the Peclet number of this system were then comparable to the one of the reference system. The used material densities can be found in Tab.10.2. In both systems a particle with a radius of $R_p = 3.77\mu\mathrm{m}$ was assumed. For the reference system a Peclet number of $Pe = 1.56 \cdot 10^3$ and for the dry cohesive model system $Pe = 2.34 \cdot 10^3$ was obtained. In both cases the Peclet number was much larger than one, which showed that the used model systems were dominated by gravity and Brownian motion could be neglected.

Calculation of laminar flow parameters

When applying a mechanical load, the motion of the indenter plate created a flow near the plate surface. The largest displacement per load step in the performed measurements was 2µm. With a reaction time of 40ms of the driving piezo-actuator (see Sec.3.2) a resulting velocity of 0.05mm/s was obtained. The characteristic length scale in this case is the maximum displacement of the indenter per load step, $L = 2\mu\mathrm{m}$. The Reynolds numbers for the different sample systems were calculated using Eq.2.30. The viscosity of this solution was measured in house with a capillary viscometer and was $\eta_{NaSCN} = 2.925 \cdot 10^{-3}\mathrm{Pa\,s}$. The viscosity of cis-decaline at 23C° was $\eta_{deca} = 3.129 \cdot 10^{-3}\mathrm{Pa\,s}$ [123]. The timescale for the decay of a laminar flow in the reference system and in the dry cohesive model system was calculated with Eq.2.31. For the timescale of a particle with radius $R_p = 3.77\mu\mathrm{m}$ being dragged with the laminar flow Eq.2.36 was used. For both systems the characteristic length of the laminar flow was assumed to be roughly the thickness of a particle layer in a sediment with $L = 10\mu\mathrm{m}$. The mass densities of silica, cis-decaline and the NaSCN-solution were obtained from Tab10.2. In the reference system the applied force on a particle with an indenter plate velocity of 0.05mm/s, was 10pN (see Eq.2.35). This force was explicitly smaller than the interaction force between two particles, which was 0.3nN (after Eq.2.7).

Calculation of the droplet deformation

For calculating the deformation energy it was assumed that a spherical droplet was elongated along one axis by ten percent with the boundary condition of volume conservation. The obtained shape of the droplet is then a prolate ellipsoid. The volume of a spherical

model system	Reynolds number Re $[10^{-5}]$	laminar flow τ_{lam} $[10^{-5}\text{s}]$	particle dragging τ_{drag} $[10^{-6}\text{s}]$
reference	4	4.3	6.5
dry cohesive	4	2.8	6.1

Table 10.4: Reynolds numbers and timescales for laminar flow for the reference and for the dry cohesive model system

droplet with radius $R_d = 4.0\mu\text{m}$ is $V_s = 268.08\mu\text{m}^3$. The volume of an ellipsoid with semi-principal axes a, b and c is

$$V_{elli} = \frac{4}{3}\pi abc \tag{10.2}$$

Using Eq.10.2 the elongated droplet has the extensions $a = 4.4\mu\text{m}$ and $c = 3.81\mu\text{m}$. The deformation energy is characterized by the change in surface energy. The surface of a prolate ellipsoid with $a > b = c$ is:

$$S_{elli} = 2\pi c \left(c + \frac{a^2}{\sqrt{a^2 - c^2}} \cdot \arcsin\left(\frac{\sqrt{a^2 - c^2}}{a} \right) \right) \tag{10.3}$$

The surface area of the prolate ellipsoid is $S_{elli} = 201.78\mu\text{m}^2$. The change in the surface between the sphere and the prolate ellipsoid is then $\Delta S = 0.72\mu\text{m}^2$. With a surface tension of the liquid-liquid interface of $\gamma_{ll} = 17 \cdot 10^{-3}$ N/m this surface change corresponds to a change in surface energy of $\Delta E = 3.06 \cdot 10^6 \text{k}_\text{B}\text{T}$.

10.5 Determination of the Rotation Angles

Conversion between spherical and Cartesian coordinates

In the starting configuration the focus vector $\vec{f}$ was directed along the x-axis. $\vec{n}$ was denoting the normal vector of the plane, pointing initially into the positive y-direction. The vectors $\vec{a}$, $\vec{f}$ and $\vec{n}$ were the base vectors of the particle coordinate system. In the following conversion equation x, y and z denote the Cartesian coordinates of the base vectors in the lab system. In the initial configuration the rotation angles had the values ($\varphi_n = 90°$, $\vartheta_n = 90°$) and ($\varphi_f = 0°$, $\vartheta_f = 90°$).

$$\varphi = \begin{cases} \arctan\left(\frac{y}{x}\right) & \text{, if } x > 0 \\ \text{sgn}(y)\frac{\pi}{2} & \text{, if } x = 0 \\ \arctan\left(\frac{y}{x}\right) + \pi & \text{, if } x < 0 \text{ and } y \geq 0 \\ \arctan\left(\frac{y}{x}\right) - \pi & \text{, if } x < 0 \text{ and } y < 0 \end{cases} \tag{10.4}$$

$$\vartheta = \arccos\left(\frac{z}{\sqrt{x^2 + y^2 + z^2}} \right) \tag{10.5}$$

Calculation of error bars of the rotation angles

The uncertainty of the rotation angles had two contributions. One uncertainty is the precision with which the position of the start and end points of the base vectors could be determined. As these positions could vary over one till two pixels a constant uncertainty of 5° was assumed here. The second contribution to the rotation angle was the degree of orthogonality between the base vectors $\vec{f}$ and $\vec{n}$. The deviation of the angle between the two base vectors from 90° plus the additional constant uncertainty of 5° was chosen as the total uncertainty of the rotation angle.

$$\Delta\varphi = 5^\circ \pm \left(\left| \arccos\left(\frac{\vec{n} \cdot \vec{f}}{|\vec{n}| \cdot \left|\vec{f}\right|} \right) - 90^\circ \right| \right) \tag{10.6}$$

The error on the rotation angels ϑ were deduced in the analog way.

10.6 Calculation of Parameters for the Wet Granulate System

Calculation of deformation parameters: Eccentricities

The eccentricity in general describes the deviation of an ellipsoid to a sphere. For an ellipsoid it can range from zero to one. The larger the eccentricity is, the less spherical is the object. In the case of the cis-decaline droplets in the wet granulate system, it was assumed that the droplets have an ellipsoidal shape. The polar eccentricity e_{pol} describes hence the deviation of the droplet from being spherical along the polar axis, which is here the z-axis. The polar eccentricity is defined as follow:

$$e_{pol} = \begin{cases} \sqrt{1 - \frac{y^e_{ext}}{z^e_{ext}}} & \text{, if } y^e_{ext} < z^e_{ext} \\ -\sqrt{1 - \frac{z^e_{ext}}{y^e_{ext}}} & \text{, if } y^e_{ext} > z^e_{ext} \end{cases} \tag{10.7}$$

y^e_{ext} and y^e_{ext} are the droplet extensions along the y- and the z-axis, which are obtained from the watershed analysis (see Sec.8.2.2). The negative sign indicates that the ellipsoid has then an oblate shape (Fig.10.5). The azimuthal eccentricity e_{azi} describes the deviation from a spherical shape in the azimuth plane, which is here the x-y-plane.

$$e_{azi} = \begin{cases} \sqrt{1 - \frac{x^e_{ext}}{y^e_{ext}}} & \text{, if } x^e_{ext} < y^e_{ext} \\ -\sqrt{1 - \frac{y^e_{ext}}{x^e_{ext}}} & \text{, if } x^e_{ext} > y^e_{ext} \end{cases} \tag{10.8}$$

Droplet parameters in wet bulk granulates under compression

In the wet bulk granulate region 2 was locally diluted after compression step four (see Sec.8.2.4). This structural change was caused by the release of deformation energy of

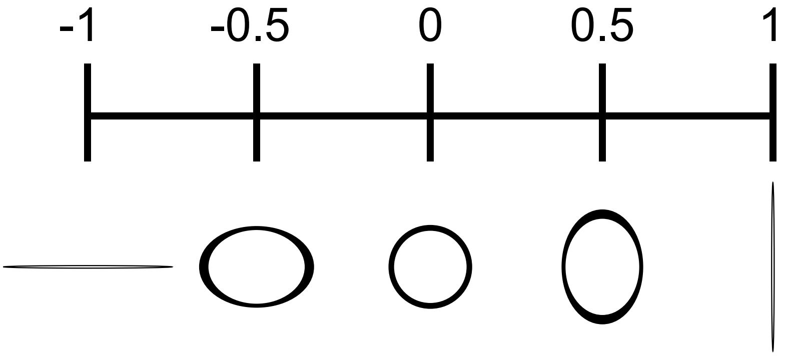

Figure 10.5: Shape and orientation of the ellipsoids for various values of the eccentricities e_{pol} and e_{azi} respectively. For very large absolute values the ellipsoids become infinitely elongated

a cis-decaline droplet (droplet before) situated there. This droplet had two possible trajectories. Tab.10.5(top row) lists the measured volumes, extensions and number of contacting particles as obtained from the watershed analysis (see Sec.8.2.2). For calculating the eccentricities (Eq.10.7 and Eq.10.8) it was assumed that the droplet had an ellipsoidal shape. Additionally the droplet volume under this assumption was calculated with Eq.10.2, indicated with "volume*". From the change in the droplet surface the deformation energy after the fourth compression step could be obtained (Tab.10.5, bottom row).

	volume [μm^3]	extension x [μm]	extension y [μm]	extension z [μm]	number of contacts
droplet before	25.2	5.078	5.273	4.778	3
droplet after D1	34.2	4.883	5.078	5.212	3
droplet after D2	22.0	4.492	4.688	4.778	3

	volume* [μm^3]	e_{pol}	e_{azi}	surface [μm^2]	deformation energy $[10^7 k_B T]$
droplet before	66.988	-0.306	0.192	79.871	-
droplet after D1	67.668	0.161	0.196	80.351	0.200
droplet after D2	52.683	0.138	0.204	67.998	-4.958

Table 10.5: Parameters of droplets in region two before and after the fourth compression step, as obtained by the watershed analysis (top row) and calculated with the assumption of an ellipsoidal shape (bottom row)

The trajectory of a droplet and its local environment situated at the cover slide could be followed over the entire compression. Tab.10.6 lists the parameters of this droplet as obtained by the watershed analysis (top row) and the calculated parameters under the assumption of an ellipsoidal shape (bottom row). As the droplet extension in z-direction for compression displacement 2μm was not accurate, the values for e_{pol}, the droplet surface and the deformation energy could not be calculated.

compression displacement	volume [μm^3]	extension x [μm]	extension y [μm]	extension z [μm]	number of contacts
0	166.1	8.008	8.398	6.950	4
2	127.3	7.227	7.813	7.384	4
4	103.5	7.422	7.813	6.081	4
6	115.0	7.422	8.008	6.081	5
8	123.5	7.617	8.008	6.081	2
10	117.1	7.617	8.008	6.081	2
12	123.7	7.617	8.008	6.081	3

	volume* [μm^3]	e_{pol}	e_{azi}	surface [μm^2]	deformation energy [$10^7 k_B T$]
0	244.728	-0.415	0.216	190.209	-
2	-	-	0.274	-	-
4	184.634	-0.471	0.224	158.321	-
6	189.242	-0.490	0.271	161.175	1.192
8	194.214	-0.490	0.221	164.118	1.229
10	194.214	-0.490	0.221	164.118	0
12	194.214	-0.490	0.221	164.118	0

Table 10.6: Parameters of a droplet situated at the cover slide over the entire compression process. The values of the compression displacement two could not be calculated, as the extension of the droplet in z was not accurate

Bibliography

[1] P.G. de Gennes: *Granular matter: A tentative view.* Rev. Mod. Phys. **71**(2), 374-382 (1999)

[2] P. Coussot: Rheometry of Pastes, Suspensions and Granular Materials: Applications in Industry and Environment. Wiley, New York (2005)

[3] J. Schwedes: *Review on testers for measuring flow properties of bulk solids (based on an IFPRI-Report 1999).* Granul. Matter **5**(1), 1-43 (2003)

[4] J. Tomas: *Energy absorption at particle contact, compression, and shear flow of dry ultrafine powder.* Part. Sci. Technol. **27**(4), 337-351 (2009)

[5] R. Tykhoniuk, J. Tomas, S. Luding, M. Kappl, L. Heim, H.J. Butt: *Ultrafine cohesive powders: From interparticle contacts to continuum behaviour.* Chem. Eng. Sci. **62**(11), 2843-2864 (2007)

[6] C. Thornton, Z. Ning, C.Y. Wu, M. Nasrullah, L.Y. Li: *Contact mechanics and coefficients of restitution.* In: T. Pöschel, S.Luding (eds.) Granular Gases, Lecture Notes in Physics **564** 184-194 (2001)

[7] G. Binnig, C.F. Quate, C. Gerber: *Atomic Force Microscope.* Phys. Rev. Lett. **56**(9), 930-933 (1986)

[8] D. Tabor, F.R.S. Winterton, R.H.S. Winterton: *Direct measurement of normal and retarded Van der Waals forces.* Proc. R. Soc. Lond. A **312**(1511) 435-451 (1969)

[9] D. Kadau, G. Bartels, L. Brendel, D.E. Wolf: *Contact dynamics simulations of compacting cohesive granular systems.* Comput. Phys. Commun. **147**(1-2), 190-193 (2002)

[10] M.A. Aguirre, J.G. Grande, A. Calvo, L.A. Pugnaloni, J.C. Geminard: *Pressure independence of granular flow through an aperture.* Phys. Rev. Lett. **104**(23), 238002-1-4 (2010)

[11] J. Zhang, T.S. Majmudar, M. Sperl, R.P. Behringer: *Jamming for a 2D granular material.* Soft Matter **6**(13), 2982-2991 (2010)

[12] H.M. Jaeger, S.R. Nagel, R.P. Behringer: *Granular solids, liquids, and gases.* Rev. Mod. Phys. **68**(4), 1259-1273 (1996)

[13] GDR MiDi: *On dense granular flows.* Eur. Phys. J. E **14**(4), 341-365 (2004)

[14] Herman, G.T.: Fundamentals of Computerized Tomography: Image Reconstruction from Projections. Springer Verlag, Berlin Heidelberg (2009)

[15] G.W. Delaney, T. Di Matteo, T. Aste: *Combining tomographic imaging and DEM simulations to investigate the structure of experimental sphere packings*. Soft Matter **6**(13), 2992-3006 (2010)

[16] R. Liu, X. Yin, H. Li, Q. Shao, P. York, Y. He, T. Xiao, J. Zhang: *Visualization and quantitative profiling of mixing and segregation of granules using synchrotron radiation X-ray microtomography and three dimensional reconstruction*. Int. J. Pharmaceut. **445**(1-2), 125-133 (2013)

[17] V.I. Uricanu, M.H.G. Duits: *Micromechanical behavior of adhesive granular silica layers: Structure deformation*. Langmuir **22**(18), 7783-7792 (2006)

[18] Z. Fournier, D. Geromichalos, S. Herminghaus, M.M. Kohonen, F. Mugele, M. Scheel, M. Schulz, B. Schulz, C. Schier, R. Seemann and A. Skudelny: *Mechanical properties of wet granular materials*. J. Phys. Cond. Matt. **17**(9), 477-502 (2005)

[19] S. Herminghaus: *Dynamics of wet granular matter*. Adv. Phys. **54**(3), 221-261 (2005)

[20] D. Filip, V.I. Uricanu, M.H.G. Duits, D. van den Ende, J. Mellema, W.G.M. Agterof, F. Mugele: *Microrheology of aggregated emulsion droplet networks, studied with AFM-CSLM*. Langmuir **22**(2), 560-574 (2006)

[21] R.L. Brown, J.C. Richards: Principles of Powder Mechanics. Pergamon Press, Oxford (1970)

[22] D. Schulze: Powders and Bulk Solids - Behavior, Characterization, Storage and Flow. Springer Verlag, Berlin Heidelberg (2008)

[23] W.H. Keesom: *On Waal's cohesion forces*. Physik. Zeitschr. **22**, 129-141 & 643-644 (1921)

[24] P. Debye: *The van der Waals cohesion forces*. Physik. Zeitschr. **21**, 178-187 (1920)

[25] F. London: *Zur Theorie und Systematik der Molekularkräfte*. Z. Physik *63*(3-4), 245-279 (1930)

[26] H.C. Hamaker: *The London-Van der Waals attraction between spherical particles*. Physica **4**(10), 1058-1072 (1937)

[27] E.M. Lifshitz: *The theory of molecular attractive forces between solids*. Soviet Phys. JETP **2**(1), 73-83 (1956)

[28] M.L. Bortz, R.H. French: *Optical reflectivity measurements using a laser plasma light-source*. Appl. Phys. Lett. **55**(19), 1955-1957 (1989)

[29] R.F. Egerton: *Electron energy-loss spectroscopy in the TEM.* Rep. Prog. Phys. **72**(1), 1-25 (2009)

[30] B.W. Ninham, V.A. Parsegian: *Van der Waals forces -Special characteristics in lipid-water systems and a general method of calculation based on Lifshitz theory.* Biophys. J. **10**(7), 646-663 (1970)

[31] J.N. Israelachvili, D. Tabor: *The measurement of Van der Waals dispersion forces in the range 1.5 to 130 nm.* Proc. Roy. Soc. London A **331**(1584), 19-39 (1972)

[32] R.H. French, R.M. Cannon, L.K. Denoyer, Y.M. Chiang: *Full spectral calculation of nonretarded Hamaker constants for ceramic systems from interband transition strengths.* Solid State Ionics **75** 13-33 (1995)

[33] M. Kappl, H.J. Butt: *The colloidal probe technique and its application to adhesion force measurements.* Part. Part. Sys. Char. **19**(3), 129-143 (2002)

[34] P. Debye, E. Hückel: *Zur Theorie der Elektrolyte. I. Gefrierpunktserniedrigung und verwandte Erscheinungen.* Physik. Zeitschr. **24**, 185-206 (1923)

[35] B. Derjaguin, L. Landau: *Theory of the stability of strongly charged lyophobic sols and of the adhesion of strongly charged particles in solutions of electrolytes.* Acta Phys. Chem. URSS **14**, 633 (1941)

[36] E.J.W. Verwey, J.T.G. Overbeek: Theory of the stability of lyophobic colloids. Elsevier, Amsterdam (1948)

[37] T. Young: *An Essay on the Cohesion of Fluids.* Phil. Trans. Roy. Soc. Lond. **95**, 65-87 (1805)

[38] Sir William Thomson: *On the equilibrium of vapour at a curved surface of liquid.* Phil. Mag. series 4, **42**(282), 448-452 (1871)

[39] S.U. Pickering: *Emulsions.* J. Chem. Soc., Trans.**91**, 2001-2021 (1907)

[40] J.C. Melrose, G.C. Wallick: *Exact geometrical parameters for pendular ring fluid.* J. Phys. Chem. **71**(11), 3676-3678 (1967)

[41] F.M. Orr, L.E. Scriven, A.P. Rivas: *Pendular rings between solids - Meniscus properties and capillary force.* J. Fluid Mech. **67**(4), 723-742 (1975)

[42] B.V. Derjaguin: *Untersuchungen über die Reibung und Adhäsion IV - Theorie des Anhaftens kleiner Teilchen.* Kolloid-Zeitschrift **69**(2), 155-164 (1934)

[43] O. Pitois, P. Moucheront, X. Chateau: *Liquid bridge between two moving spheres: An experimental study of viscosity effects.* J. Colloid Interface Sci. **231**(1), 26-31 (2000)

[44] H.J. Butt, M. Kappl: Surface and interfacial forces, Wiley-VCH, Weinheim (2010)

[45] A. Einstein: *Über die von der molekularkinetischen Theorie der Wärme geforderte Bewegung von in ruhenden Flüssigkeiten suspendierten Teilchen.* Annalen der Physik **322**(8), 549-560 (1905)

[46] M. Smoluchowski: *Mean path of a gaseous molecule.* Bull. Int. De l'Acad. Des Sci. De Cracovie **3**, 202-213 (1906)

[47] A.C. Fischer-Cripps: Introduction to Contact Mechanics. In: Mechanical Engineering Series, Springer Verlag, Berlin Heidelberg (2007)

[48] S.D. Poisson: *Note sur l'Extension des Fils et des Plaques élastiques.* Annls Chim. Phys. **36**, 384-387 (1827)

[49] N. Gaspar: *A granular material with a negative Poisson's ratio.* Mech. Mater. **42**(7), 673-677 (2010)

[50] W. Oliver, G.M. Pharr. *An improved technique for determining hardness and elastic modulus using load and displacement sensing indentation experiments.* J. Mater. Res. **7**(6), 1564-1583 (1992).

[51] W. Oliver, G.M. Pharr. *Measurement of hardness and elastic modulus by instrumented indentation: Advances in understanding and refinements to methodology.* J. Mater. Res. **19**(1), 3-20 (2004).

[52] R.S. Bradley: *The Cohesive Force between Solid Surfaces and the Surface Energy of Solids.* Philos. Mag. **32**, 853-862 (1932)

[53] H. Hertz: *Über die Berührung fester elastischer Körper.* J. Reine Angew. Math. **92**, 156-171 (1882)

[54] T.C.T. Ting: *Contact stresses between a rigid indenter and a viscoelastic half-space.* J. Appl. Mech. **33**(4), 845-854 (1966)

[55] I.N. Sneddon: *The relation between load and penetration in the axisymmetric boussinesq problem for a punch of arbitrary profile.* Int. J. Eng. Sci. **3**(1), 47-57 (1965)

[56] K.L. Johnson, K. Kendall, A.D. Roberts: *Surface energy and the contact of elastic solids.* Proc. R. Soc. London A **324**, 301-313 (1971)

[57] B.V. Derjaguin, V.M. Muller, Y.P. Toporov: *Effect of contact deformations on the adhesion of particles.* J. Colloid Interface Sci. **53**, 314-325 (1975)

[58] D. Maugis: *Adhesion of spheres: The JKR-DMT transition using a Dugdale model.* J. Colloid Interface Sci. **150**, 243-269 (1992)

[59] H. Krupp: *Particle adhesion theory and experiment.* Adv. Coll. Int. Sci. **1**(2), 111-239 (1967)

[60] S. Wanka, M. Kappl, M. Wolkenhauer, H.J. Butt: *Measuring adhesion forces in powder collectives by inertial detachment.* Langmuir (2013) DOI:10.1021/la404014d

[61] D.S. Rimai, L.P. Demejo, W. Vreeland, R. Bowen, S.R. Gaboury, M.W. Urban: *The effect of Young's modulus on the surface-force-induced contact radius of spherical glass particles on polyurethane substrates.* J. Appl. Phys. **71**(5), 2253-2258 (1992)

[62] F.P. Bowden, D. Tabor: The friction and lubrication of solids. Oxford University Press, Oxford (1950)

[63] J.A. Greenwood, J.B.P. Williamson: *Contact of nominally flat surfaces.* Proc. R. Soc. Lond. A **295**, 300-319 (1966)

[64] D. Tabor: *The Mechanism of rolling friction II. The elastic range.* Proc. R. Soc. Lond. A **229**, 198-220 (1955)

[65] C. Dominik, A.G.G.M. Tielens: *Resistance to rolling in the adhesive contact of two elastic spheres.* Philos. Mag. A **72**(3), 783-803 (1995)

[66] O. Reynolds: *On rolling friction.* Philos. Trans. R. Soc. Lond. **166**, 155-174 (1876)

[67] D.R. Lide (ed.): CRC Handbook of Chemistry and Physics, Internet Version 2005. CRC Press, Boca Raton, FL (2005)

[68] Institution of Chemical Engineers: Standard Shear Testing Technique for Particulate Solids Using the Jenike Shear Cell. IChemE, Rugby (1989)

[69] J. B. Pawley: Handbook of biological confocal microscopy. Springer Verlag, Berlin Heidelberg (2006).

[70] S.W. Paddock, K.W. Eliceiri: *Laser Scanning Confocal Microscopy: History, Applications, and Related Optical Sectioning Techniques.* In: S.W. Paddock (ed.) Confocal Microscopy - Methods in Molecular Biology **1075**, 9-47 (2014)

[71] M. Roth: *Rheology of arrested colloids: a parameter study using novel experimental methods.* Dissertation, Johannes Gutenberg-Universität Mainz (2011)

[72] J. Wenzl, R. Seto, M. Roth, H.J. Butt, G.K. Auernhammer: *Measurement of rotation of individual spherical particles in cohesive granulates.* Granul. Mat. **15**(4), 391-400 (2013)

[73] A. Van Blaaderen, A. Vrij: *Synthesis and characterization of colloidal dispersions of fluorescent, monodisperse silica spheres.* Langmuir **8**(12), 2921-2931 (1992)

[74] N.A.M. Verhaegh, A. Van Blaaderen: *Dispersions of Rhodamine-labeled silica spheres: synthesis, characterization, and fluorescence confocal scanning laser microscopy.* Langmuir **10**(5), 1427-1438 (1994)

[75] T. Karstens, K. Kobs: *Rhodamine B and rhodamine 101 as reference substances for fluorescence quantum yield measurements.* J. Phys. Chem. **84**(14), 1871-1872 (1980)

[76] H.P. Latscha, H.A. Klein: Anorganische Chemie - Chemie Basiswissen I, Springer Verlag, Berlin Heidelberg (2007)

[77] F.J. Kahn, G.N. Taylor, H. Schonhorn: *Surface-produced alignment of liquid crystals.* Proceedings of the IEEE **61**(7), 823-828 (1973)

[78] J.W. Jansen, C.G. Dekruif, A. Vrij: *Attractions in sterically stabilized silica dispersions. II. Experiments on phase separation induced by temperature variation.* J. Colloid Interface Sci. **114**(2), 481-491 (1986)

[79] C.J. Rueb, C.F. Zukoski: *Viscoelastic properties of colloidal gels.* J. Rheol. 41(2), 197-218 (1997)

[80] C.G. Dekruif, P.W. Rouw, W.J. Briels, M.H.G. Duits, A. Vrij, R.P. May: *Adhesive hard-sphere colloidal dispersions - A small-angle neutron-scattering study of stickiness and the structure factor.* Langmuir **5**(2), 422-428 (1989).

[81] C.R. Crick, I.P. Parkin: *Superhydrophobic silica films on glass formed by hydrolysis of an acidic aerosol of tetraethylorthosilicate.* J. Mater. Chem. **21**, 9362-9366 (2011)

[82] E. Nürnberg, P. Surmann: Hagers Handbuch der Pharmazeutischen Praxis, Band 2, Springer Verlag, Berlin Heidelberg (1991)

[83] J.C. Bird, S Mandre, H.A. Stone: *Short-time dynamics of partial wetting.* Phys. Rev. Lett. **100**(23), 234501-1-4 (2008)

[84] Crocker, J.C., Grier, D.G.: Methods of Digital Video Microscopy for Colloidal Studies. J. Colloid Interface Sci. **179**(1), 298-310 (1996)

[85] http://www.physics.emory.edu/˜weeks/idl/

[86] P. Varadan, M.J. Solomon: *Direct visualization of flow-induced microstructure in dense colloidal gels by confocal laser scanning microscopy.* J. Rheol. **47**(4), 943-968 (2003)

[87] N.N. Medvedev: *The extension of the Voronoi-Delaunay method to describe a void space inside polydisperse ball packings.* Dokl. Akad. Nauk. **337**(6), 767-771 (1994)

[88] K. Iwashita, M. Oda: *Rolling resistance at contacts in simulation of shear band development by DEM.* J. Eng. Mech.-ASCE **124**(3), 285-292 (1998)

[89] K. Wada, H. Tanaka, T. Suyama, H. Kimura, T. Yamamoto: *Numerical simulation of dust aggregate collisions. I. Compression and disruption of two-dimensional aggregates.* Astrophys. J. **661**(1), 320-333 (2007)

[90] F.A. Gilabert, J.-N. Roux, A. Castellanos: *Computer simulation of model cohesive powders: Influence of assembling procedure and contact laws on low consolidation states.* Phys. Rev. E **75**(1), 011303-1-26 (2007)

[91] S. Luding: *Cohesive, frictional powders: contact models for tension.* Granul. Mat. **10**(4), 235-246 (2008)

[92] R. Seto, R. Botet, G.K. Auernhammer, H. Briesen: *Restructuring of colloidal aggregates in shear flow: Coupling interparticle contact models with Stokesian dynamics.* Eur. Phys. J. E **35**(128), 1-12 (2012)

[93] L.O. Heim, J. Blum, M. Preuss, H.J. Butt: *Adhesion and friction forces between spherical micrometer-sized particles.* Phys. Rev. Lett. **83**(16), 3328-3331 (1999)

[94] L.O. Heim, H.J. Butt, R. Schräpler, J. Blum: *Analyzing the compaction of high-porosity microscopic agglomerates.* Aust. J. Chem. **58**(9), 671-673 (2005)

[95] J.P. Pantina, E.M. Furst: *Elasticity and critical bending moment of model colloidal aggregates.* Phys. Rev. Lett. **94**(13), 138301-1-4 (2005)

[96] A. Hasan, K. Alshibli: *Three dimensional fabric evolution of sheared sand.* Granul. Matter **14**(4), 469-482 (2012)

[97] S.M. Anthony, L. Hong, M. Kim, S. Granick: *Single-particle colloid tracking in four dimensions.* Langmuir **22**(24), 9812-9815 (2006)

[98] M.P. Lettinga, G.H. Koenderink, B.W.M. Kuipers, E. Bessels, A.P. Philipse: *Rotational dynamics of colloidal spheres probed with fluorescence recovery after photobleaching.* J. Chem. Phys. **120**(9), 4517-4529 (2004)

[99] M. Roth, M. Franzmann, M. D'Acunzi, M. Kreiter, G.K. Auernhammer: *Experimental analysis of single deformations and rotations in colloidal and granular systems.* arXiv:1106.3623v2 [cond-mat.soft] (2011)

[100] J.B. Kuipers: Quaternions and rotation sequences. Princeton University Press, Princeton, New Jersey (2002)

[101] F. Da Cruz, F. Chevoir, D. Bonn, P. Coussot: *Viscosity bifurcation in granular materials, foams, and emulsions.* Phys. Rev. E **66**(5), 051305-1-7 (2002)

[102] P. Welker, S. McNamara: *Failure in small granular assemblies.* In: M.L.S. Nakagawa (ed.) Powders and Grains 2009, AIP Conference Proceedings **1145**, 289-292 (2009)

[103] E. Hamm, F. Tapia, F. Melo: *Dynamics of shear bands in a dense granular material forced by a slowly moving rigid body.* Physical Review E **84**(4), 041304-1-7 (2011)

[104] J.F. Métayer, D.J. Suntrup III, C. Radin, H.L. Swinney, M. Schröter: *Shearing of frictional sphere packings.* EPL **93**(6) 64003-1-5 (2011)

[105] P. Schall, M. van Hecke: *Shear bands in matter with granularity.* In: S. Gubins (ed.) Annual Review of Fluid Mechanics **42**, 67-88 (2010)

[106] C. Thornton, L. Zhang: *Numerical simulations of the direct shear test.* Chem. Eng. Technol. **26**(2), 153-156 (2003)

[107] S. Abedi, A. Rechenmacher, A. Orlando: *Vortex formation and dissolution in sheared sands.* Granul. Matter **14**(6), 695-705 (2012)

[108] M. Lätzel, S. Luding, H.J. Herrmann, D.W. Howell, R.P. Behringer: *Comparing simulation and experiment of a 2D granular Couette shear device.* Eur. Phys. J. E **11**(4), 325-333 (2003)

[109] W. Losert, K. Ronaszegi, J. Weijs, J.A. Dijksman, S. Slotterback: *Three dimensional particle rearrangements during slow granular shear flow in a split bottom geometry.* In: M.L.S. Nakagawa (ed.) Powders and Grains 2009, AIP Conference Proceedings **1145**, 347-350 (2009)

[110] J.A. Dijksman, F. Rietz, K.A. Lörincz, M. van Hecke, W. Losert: *Refractive index matched scanning of dense granular materials.* Rev. Sci. Instrum. **83**(1), 0113011-12 (2012)

[111] J. Wenzl, R. Seto, R. Mayer, T.M.L. Palmer, G.K. Auernhammer: *Sheared granulates in strain-controlled geometry - A confocal microscopy study on a single particle level.* Gran. Matt. **submitted**

[112] E. Koos and N. Willenbacher: *Capillary forces in suspension rheology.* Science **331**(6019), 897-900 (2011)

[113] R. Schwarze, A. Gladkyy, F. Uhlig, S. Luding: *Rheology of weakly wetted granular materials: a comparison of experimental and numerical data.* Granul. Matt. **15**(4), 455-465 (2013)

[114] C. Gögelein, M. Brinkmann, M. Schröter and S. Herminghaus: *Controlling the formation of capillary bridges in binary liquid mixtures.* Langmuir **26**(22), 17184-17189 (2010)

[115] M. Scheel, R. Seemann, M. Brinkmann, M. Di Michiel, A. Sheppard, B. Breidenbach, S. Herminghaus: *Morphological clues to wet granular pile stability.* Nat. Mater. **7**(3), 189-193 (2008)

[116] R. Mani, D. Kadau, H. Herrmann: *Liquid migration in sheared unsaturated granular media.* Granul. Matter, **15**(4), 447-454 (2012)

[117] A.T. Krummel, S.S. Datta, S. Münster, D. A. Weitz: *Visualizing multiphase flow and trapped fluid configurations in a model three-dimensional porous medium.* AIChE Journal **59**(3), 1022-1029 (2013)

[118] J. Ohser, K. Schladitz: 3D Images of Materials Structures: Processing and Analysis. Wiley-VCH Verlag, Weinheim (2009)

[119] G.K. Auernhammer, M. Roth, H.J. Butt: *Optisches Rastermikroskop mit zwei Scaneinheiten.* Patent DE-10 2012 101 344.6 (2012)

[120] Landolt-Börnstein, Group IV Physical Chemistry, Volume 17: Static Dielectric Constants of Pure Liquids and Binary Liquid Mixtures (Supplement to IV/6), Springer-Verlag Berlin Heidelberg (2008)

[121] Landolt-Börnstein, Group III Condensed Matter, Volume 47: Refractive Indices of Pure Liquids and Binary Liquid Mixtures (Supplement to III/38), Springer-Verlag Berlin Heidelberg (2008)

[122] H.B. Gray: Elektronen und chemische Bindung, de Gruyter, Berlin (1973)

[123] Landolt-Börnstein, Group IV Physical Chemistry, Volume 18: Viscosity of Pure Organic Liquids and Binary Liquid Mixtures, Springer-Verlag Berlin Heidelberg (2008)

List of Symbols and Abbreviations

Abbreviations

AFM	Atomic force microscope
APS	(3-aminopropyl)triethoxysilane
DMOAP	Dimethyloctadecyl[3-(trimethoxysilyl)propyl] ammonium chloride
HDMS	Hexamethyl-Disilazane
LSCM	Laser Scanning Confocal Microscope
NaSCN	Sodium thiocyanate
SEM	Scanning Electron Microscope
SFA	Surface force apparatus
TES	Tetraethoxysilane
TMS	Trimethylsilyl

Greek Symbols

α	Polarizability
α_i	Polarizability of molecule i
β	Tilting angle of arbitrary plane in granulate bulk (see Mohr circle)
ΔP	Laplace pressure
δ	Indentation depth
ϵ_i	Linear elongation in direction i (x,y,z)
ε	Dielectric constant (relative permittivity)
$\varepsilon''(\omega)$	Dielectric response function
ε_i	Dielectric constant (relative permittivity) of molecule i
η	Viscosity

$\dot{\gamma}$	Shear rate
γ	Shear strain
γ_i	Surface tension of material i (s: solid, l:liquid)
γ_{ij}	Interfacial tension of material i and j (s: solid, l:liquid)
κ	Inverse Debye length
κ_c	Capillary constant
λ	Wavelength
μ	Friction coefficient
μ_r	Rolling friction coefficient
μ_s	Sliding friction coefficient
μ_{kin}	Kinetic friction coefficient
μ_{stat}	Static friction coefficient
$\overline{\mu}_r$	Averaged rolling friction coefficient
ν	Frequency
ν_e	Mean ionization frequency of the materials for calculation of Hamaker constant
ν_i	Ionization frequency of molecule i
ν_p	Poisson ratio
ω	Angular frequency
ϕ_{ave}	Averaged volume fraction
$\phi_{local,i}$	Local volume fraction of particle i (Voronoi cell volume fraction)
ϕ_{local}	Local volume fraction
$\phi_{plateau}$	Averaged volume fraction of the plateau
φ_f	Rotation angle (azimuth) concerning focal vector
φ_n	Rotation angle (azimuth) concerning normal vector
ψ	Electric potential
ψ_0	Surface potential

$\Delta\varrho$	Mass density difference between a solid object and the surrounding liquid
ϱ_e	Local charge distribution
ϱ_i	Molecular density of object i
ϱ_l	Liquid mass density
ϱ_s	Solid mass density
ϱ_{e,c_0}	Local charge distribution with counterion concentration
σ_c	Critical normal stress
σ_e	Surface charge density
σ_h	Normal stress in horizontal direction
σ_i	Normal stress in direction i (x,y,z)
σ_v	Normal stress in vertical direction
σ_β	Normal stress on plane under angle β
τ_b	Typical timescale for Brownian motion
τ_c	Critical yield stress
τ_i	Tangential stress in direction i (x,y,z)
τ_s	Typical timescale for sedimentation
τ_β	Tangential stress on plane under angle β
τ_{drag}	Timescale for a particle being dragged with the laminar flow
τ_{lam}	Timescale for the build up of a laminar flow
Θ	Contact angle
Θ_i	Contact angle at point i
ϑ_f	Rotation angle (polar) concerning focal vector
ϑ_n	Rotation angle (polar) concerning normal vector
Latin Symbols	
$\vec{a}$	base vector for particle own coordinate system
A	Area

a_c	Contact radius
A_H	Hamaker constant
A_{AIB}	Hamaker constant for material A, B and I
A_{app}	Apparent contact area
A_{real}	Real contact area
a,b,c	Semi-principal axes of an ellipsoid
$C_{ijk}^{(\alpha)}$	Convolved image data concerning mask α
c_0	Counterion concentration
c_b	background salt concentration
$c_{0,i}$	Counterion concentration of molecule i
C_{AB}	Total interaction constant for materials A and B
C_{Debye}	Debye interaction constant for Van der Waals interactions
C_{ijk}	Convolved image data
C_{Keesom}	Keesom interaction constant for Van der Waals interactions
C_{London}	London interaction constant for Van der Waals interactions
C_{total}	Total interaction constant, sum of Keesom, Debye and London interaction constant
D	Separation distance
D_{max}	Maximum extension of a cis-decaline molecule
D_{min}	Minimum extension of a cis-decaline molecule
ΔE	Change in surface energy
$\mathcal{E}$	Elastic modulus (also Young's modulus)
$\vec{E}$	Electric field
e_{azi}	Azimuth eccentricity
E_{bind}	Binding energy
E_{deform}	Deformation energy
E_{el}	Electrical energy needed for charge separation

e_{pol}	Polar eccentricity
E_{VdW}	Van der Waals energy
$\vec{f}$	Focal vector, base vector for particle own coordinate system
F,$\vec{F}$	Force
F_L	Lateral force
F_N	Normal force
F_{ext}, $\vec{F}_{ext}$	External force
$F_{N,Hertz}$	Normal force in Hertz model
$F_{N,JKR}$	Normal force in JKR model
h	Height coordinate
I_{ijk}	3D image data (intensity)
K	Lateral stress ratio
L	Typical length scale
M	Torque
$M_{ijk}^{(\alpha)}$	Mask for convolution process for mask α
M_{ijk}	Mask for convolution process
$\vec{n}$	Normal vector, base vector for particle own coordinate system
NA	Numerical Aperture
P	Pressure
p	Dipole moment
p_i	Dipole moment of molecule i
P_v	Vapor pressure of curved surface
P_{gas}	Pressure in gas phase
p_{ind}	Induced dipole moment
P_{liquid}	Pressure in liquid phase
$P_{v,0}$	Vapor pressure of a planar surface

$\overline{R}_p$	Averaged particle radius
R	Leaving group during chemical reaction
r	Radial distance in the spherical coordinate system
R^*	Effective radius
R_d	Droplet radius
R_i	Radius of particle i
r_i	Radius of curvature at point i
R_p	Particle radius
R_r	Radius of rolling object for friction coefficient measurements
Re	Reynolds number
ΔS_{elli}	Change in surface of a prolate ellipsoid
S_{elli}	Surface of a prolate ellipsoid
T	Temperature
$\overline{v}$	Typical velocity
$\overrightarrow{v}_p$	Particle velocity
$\widetilde{V}_i$	Voronoi cell Volume of particle i
V	Volume
v, $\overrightarrow{v}$	Velocity
V_m	Molar volume
V_s	Droplet volume with spherical shape
V_{Debye}	Debye part of the Van der Waals potential
V_{elli}	Droplet volume with ellipsoidal shape
V_{Keesom}	Keesom part of the Van der Waals potential
V_{London}	London part of the Van der Waals potential
V_{VdW}	Van der Waals potential
$\overrightarrow{x}$	Spatial point in Cartesian coordinates

$\vec{x}_i$	Central position of the particle i in Cartesian coordinates
x	Cartesian distance variable in the Cartesian coordinate system
x_a,y_a,z_a	Cartesian coordinates of point a
x_o,y_o,z_o	Cartesian coordinates of point 0, particle center position in image analysis
x,y,z	Cartesian coordinates
Z	Valency
Z_i	Valency of molecule i
Z_p	Total particle surface charge

Nature Constants

$\hbar$	Reduced Planck constant
ε_0	Electric constant (vacuum permittivity)
c	Speed of light
e	Electric charge
g	Acceleration of gravity
k_B	Boltzmann constant
N_A	Avogadro constant

List of Figures

List of Tables